



Investigation of the Deuteron Breakup on Protons in the Forward Angular Region

A doctoral dissertation submitted to the Faculty of
Physics, Astronomy and Applied Computer Science
of the Jagiellonian University

by

Izabela Ciepał

Thesis Advisor

dr hab. Stanisław Kistryn, prof. UJ

Kraków, September 2010

Contents

| | | |
|----------|-------------------------------------------------------------------------|-----------|
| 1 | Introduction | 5 |
| 2 | Experimental observables | 9 |
| 2.1 | Kinematical relations of the ${}^1H(d, pp)n$ breakup reaction | 9 |
| 2.2 | Elastic scattering process | 11 |
| 2.3 | Cross section and analyzing powers | 11 |
| 3 | Theoretical approaches to the 2N and 3N systems | 15 |
| 3.1 | Realistic potentials | 16 |
| 3.2 | Coupled-channel formalism (CCP) | 17 |
| 3.3 | Chiral Perturbation Theory | 18 |
| 3.4 | Coulomb interaction | 19 |
| 3.5 | Acting of 3N forces | 20 |
| 4 | Experimental setup | 23 |
| 4.1 | COSY accelerator | 23 |
| 4.2 | Production of a polarized deuteron beam | 24 |
| 4.3 | GEM facility | 26 |
| 4.3.1 | Big Karl spectrometer and a Dipole Exit counter | 26 |
| 4.3.2 | Target section | 26 |
| 4.3.3 | Veto and luminosity counters | 27 |
| 4.3.4 | Germanium Wall | 27 |
| 4.3.5 | Electronics | 31 |
| 5 | Data analysis | 33 |
| 5.1 | Basics of software analysis | 33 |
| 5.2 | Reconstruction of the particles trajectories | 33 |
| 5.3 | Angular information | 35 |
| 5.4 | Identification of the reaction channels | 36 |
| 5.5 | Testing the detection system geometry | 38 |
| 5.6 | Energy calibration | 41 |
| 5.7 | Energy resolution of GeWall detectors | 42 |
| 5.8 | Determination of the beam polarization | 45 |
| 5.8.1 | Selection of the elastic scattering events | 45 |
| 5.8.2 | Beam polarization | 47 |
| 5.8.3 | Vector analyzing power of the elastic scattering | 48 |
| 5.9 | Efficiency of the detection system | 49 |

| | | |
|----------|--------------------------------------------------------------------------------|------------|
| 5.9.1 | Efficiency of the Quirl detector | 50 |
| 5.9.2 | Efficiency of Pizza 1 detector | 52 |
| 5.9.3 | Efficiency of the Pizza 2 detector | 52 |
| 5.10 | Evaluation of the breakup observables | 56 |
| 5.10.1 | Selection of events | 56 |
| 5.10.2 | Determination of the breakup cross section | 57 |
| 5.10.3 | Vector analyzing powers of the breakup process | 60 |
| 5.11 | Discussion of possible sources of uncertainties | 62 |
| 5.11.1 | Statistical uncertainties | 62 |
| 5.11.2 | Systematic uncertainties | 63 |
| 6 | Results | 67 |
| 6.1 | Experimental results | 67 |
| 6.2 | Averaging of the theoretical predictions over the integration limits | 67 |
| 6.3 | Comparisons of the results with theory | 69 |
| 6.3.1 | The vector analyzing powers - individual configurations | 72 |
| 6.3.2 | The cross section values - individual configurations | 76 |
| 7 | Summary and conclusions | 81 |
| | Appendix A | 83 |
| | Appendix B | 93 |
| | Acknowledgements | 99 |
| | Bibliography | 101 |

Chapter 1

Introduction

One of the most important goals of modern nuclear physics is precise study of the forces acting between nucleons. This fundamental knowledge is necessary for understanding of properties and interactions of nuclei.

Properties of few-nucleon systems at medium energies are determined by pairwise nucleon-nucleon (NN) interaction, which is a dominant component. On a basis of the meson exchange theory, which stems from the Yukawa's idea [1], models of NN forces were created. These new generation realistic NN potentials reproduce the NN scattering data with an impressive precision, expressed by a χ^2 per degree of freedom very close to one. Nowadays, since QCD cannot yet be solved in the nonperturbative regime, the realistic two-nucleon (2N) potentials, together with the more sophisticated approaches like coupled-channels (CC) method [2, 3] and the fundamental one based on Chiral Perturbation Theory (ChPT) [4, 5], constitute a rich theoretical basis for description of the NN interaction.

Now, an obvious question needs to be stated, whether these 2N potentials describe the experimental properties of systems with more than two nucleons. In order to investigate this problem, the simplest testing ground, the three-nucleon (3N) system was chosen. As it turned out, even the most fundamental properties, the binding energies of 3H and 3He [6], have not been reproduced in a proper way. This experimental fact was the first clue for existence and significance of additional dynamics appearing in the presence of the third nucleon, which is referred to as three-nucleon force (3NF). Further and richer indications of 3NF existence come from the nucleon-deuteron (Nd) high precision scattering data for the cross sections and spin observables [7–15]. In this case the first evidence of 3NF effect in scattering was observed when studying minima of the Nd elastic scattering cross sections for incoming nucleon energies larger than 60 MeV [7]. Quantitative conclusions are nowadays possible due to the fact that rigorous technique of solving the Faddeev equations with any short range interaction for the 3N system (e.g. [16]) was formulated. There exist various models of 3NF [17–20] derived from the meson exchange theory, which combined with the pure NN forces can be used in such calculations. The 3NF potentials are naturally obtained within the coupled-channel framework, as well as in the Chiral Perturbation Theory (effective field theory for the NN interaction). Comparisons of the above calculational approaches with the rich set of the elastic Nd scattering observables demonstrate the importance of 3NF (see Fig. 1.1), nevertheless reveal discrepancies, especially in various polarization data [9, 10, 12, 14], but also in certain cross-section angular distributions [12, 13, 15]. These indigences remain, even if the full available 3N dynamics

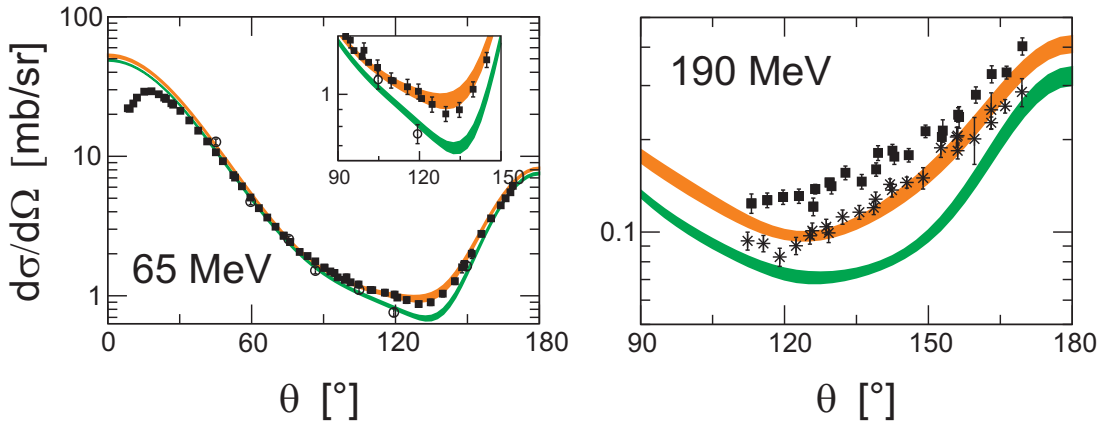


Figure 1.1: Comparison of theoretical predictions and experimental data for the Nd elastic scattering differential cross section at 65 MeV and 190 MeV beam energy. The two bands represent the theoretical calculations of the NN potentials with (orange) and without the 3NF model (green) included. Open circles are the nd data [21], full squares and stars are pd data [22], [23] and [9]. Figure adopted from [24].

is taken into account, what indicates that the 3NF models are still missing some relevant ingredients.

A natural extension of the experimental program is exploration of the nucleon-deuteron breakup process, whose final state provides the richest field for verifying and developing the interaction models. Up to now the experimental activities in this field were limited to very small fraction of the phase space [25], what did not allow to draw any global conclusions. The first new generation measurement of the ${}^1H(\vec{d}, pp)n$ breakup reaction in a wide phase-space region, performed at the beam energy of 130 MeV by the polish-dutch group provided very interesting data. The results, when compared with the theoretical predictions showed not only the significance of the 3NF in the experimental cross sections data [26, 27], but also revealed new unexpected effects. For the configurations characterized by small polar angles of the emitted protons and at large relative azimuthal angles φ_{12} the theoretical predictions strongly underestimate data, while at the small φ_{12} angles, the data are overestimated - see Fig. 1.2. This kind of disagreements led to a conclusion that their can be understood qualitatively as the action of the electromagnetic long-range force, neglected in the mentioned above theories. The first calculations with the Coulomb interaction included were performed within the coupled-channels approach [29] for the elastic proton-deuteron scattering. Then their were developed for the pd breakup process [30] and clearly confirmed the above conclusion. Moreover, the Coulomb force was recently implemented in calculations [31] with the realistic AV18 NN potential [32] combined with the Urbana IX 3NF model [19]. Within this approach the observables for the pd elastic scattering and breakup reactions were predicted and will be shown later in this Thesis.

In spite of the fact that in the recent years developments of the theoretical models describing the 3N systems were quite intensive, the experimental data still suggest some additional aspects of the 3N dynamics, which are not considered in the predictions. In order to investigate this, a further measurement of the vector and tensor analyzing powers of the deuteron-proton breakup reaction was performed as the extension of the previous one. The obtained results [33] stay in good agreement with the theoretical calculations

in terms of the 3NF effect. In particular, it is true for vector analyzing powers in the whole studied phase-space. In case of the tensor analyzing powers certain discrepancies are observed in the region where the Coulomb effects in the cross section case were important, here, however, their influence is very small. One can therefore conclude that the procedure of implementation of the electromagnetic interaction in the theoretical models has not been finally developed yet.

The theoretical approaches, within which the inclusion of the Coulomb interaction was recently performed need quantitative verification. The best testing region is the part of the phase-space where the influence of the electromagnetic force is seizable, i.e. the region of very small polar angles. The new calculations predict quite spectacular effects connected with the presence of the Coulomb force for the cross sections and rather small for the analyzing powers - see Fig. 1.3. Furthermore, in case of the polarization observables various theoretical approaches lead to different behavior of the 3NF (see Fig. 1.4), what also requires verification.

To meet the above expectations, an experiment was carried out with the use of the Germanium Wall detector at the Research Center in Jülich. This experimental studies of the ${}^1H(\vec{d}, pp)n$ breakup reaction with the 130 MeV polarized deuteron beam allowed to extend the available data base at medium energies to the very forward angular domain ($5^\circ \div 14^\circ$). The investigated region of the phase-space is extremely important to check the predictions of the Coulomb force influence.

The aim of this dissertation was to determine precise values of the differential cross sections and the vector analyzing powers for the $d - p$ breakup reaction in the forward angular region and to compare the results with the theoretical predictions originating from various approaches which model the 3N system dynamics. The data were obtained at 135 kinematical configurations in case of the cross section, whereas for vector analyzing powers A_x and A_y at 42 configurations.

Chapter 2 contains a description of the kinematical relations of the $d - p$ breakup reaction, as well as theoretical characteristic of the experimental breakup observables. Chapter 3 contains a brief discussion of the 2N and 3N theoretical approaches which are

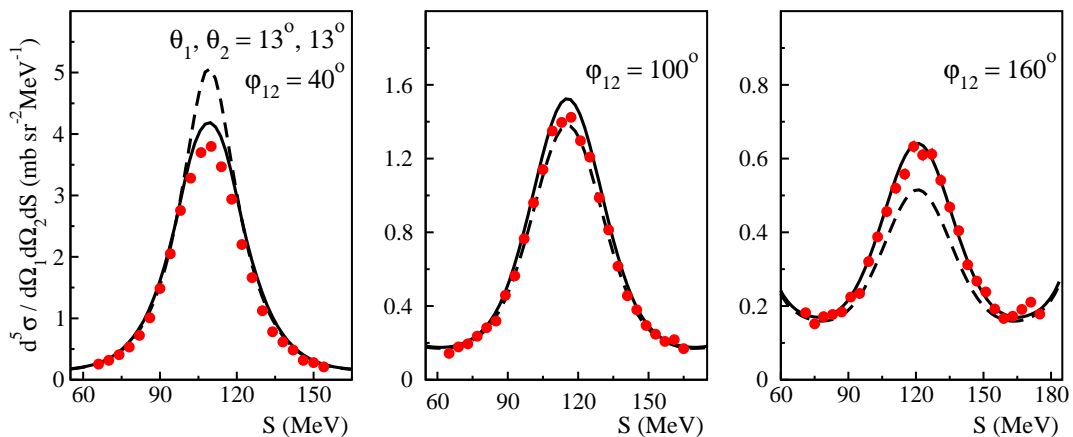


Figure 1.2: Cross sections for three different kinematical configurations of the ${}^1H(\vec{d}, pp)n$ reaction. Lines represent calculations with (solid) and without (dashed) Coulomb interaction included. Figure adopted from [28].

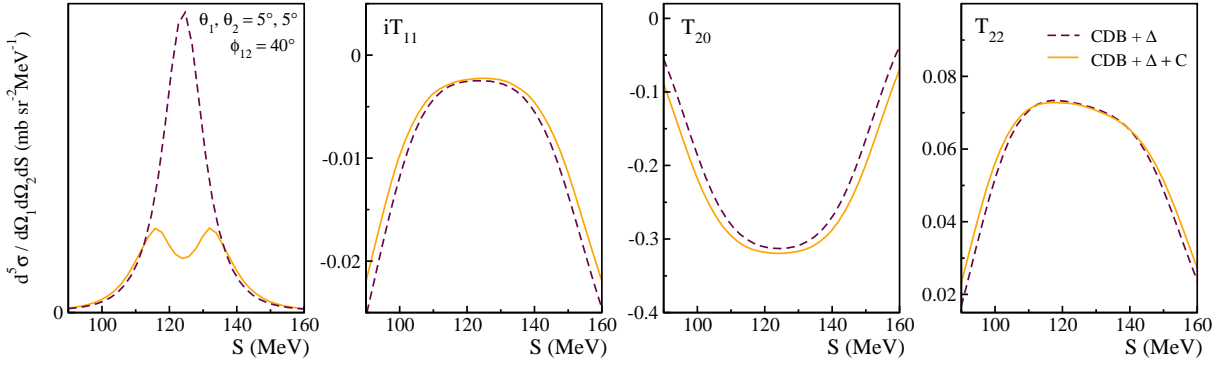


Figure 1.3: Examples of the predicted in the coupled-channel approach differential cross sections and analyzing powers of the breakup reaction at 65 MeV/nucleon in the kinematical configuration $\theta_1 = 5^\circ$, $\theta_2 = 5^\circ$ and $\varphi_{12} = 40^\circ$. The dashed lines show the results of the theoretical calculations with the CD Bonn+ Δ potential, the solid line represent the predictions obtained with the Coulomb force included in the formalism.

used for comparisons with the experimental results. Chapter 4 is committed to description of the experimental setup and technique. Chapter 5 contains presentation of all procedures used in evaluation of the interesting observables. This chapter gives discussion of the method of obtaining the beam polarization values, as well as of the evaluated vector analyzing powers for the $d - p$ elastic scattering process. Moreover, it presents a detailed description of the detection system efficiencies, methods leading to construction of the kinematical spectra, as well as gives the information about the evaluation of the breakup observables - the vector analyzing powers A_x and A_y , and the differential cross sections. Chapter 6 is committed to the global discussion of the results, as well as to the detailed comparisons of the data with theoretical calculations. Summary and final conclusions can be found in Chapter 7. Appendix A and Appendix B contain all the results of the breakup cross sections and vector analyzing powers, respectively, obtained in this Thesis.

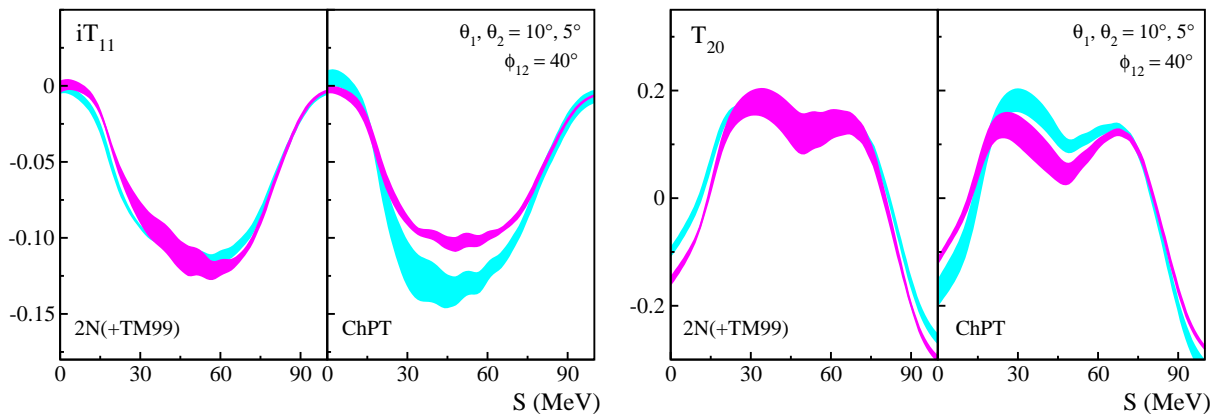


Figure 1.4: Examples of the analyzing powers of the breakup reaction at 65 MeV/nucleon calculated with the realistic potentials (left panels) and within the ChPT (right panels) for the kinematical configuration $\theta_1 = 10^\circ$, $\theta_2 = 5^\circ$ and $\varphi_{12} = 40^\circ$. The magenta bands represent the calculations with the 3NF included in the dynamics, the cyan bands show the predictions of the pure NN interaction.

Chapter 2

Experimental observables

2.1 Kinematical relations of the ${}^1H(\vec{d}, pp)n$ breakup reaction

The investigated breakup reaction ${}^1H(\vec{d}, pp)n$ with three free nucleons in the final state (see Fig. 2.1) is kinematically described by the momenta of the two protons: \vec{p}_1, \vec{p}_2 and one neutron: \vec{p}_3 , what amounts to 9 variables. Energy and momentum conservations in this case are expressed as follows:

$$\begin{aligned} E_d &= E_1 + E_2 + E_3 - E_b, \\ \vec{p}_d &= \vec{p}_1 + \vec{p}_2 + \vec{p}_3, \end{aligned} \quad (2.1)$$

where E_d, E_1, E_2, E_3 denote the kinetic energies of the deuteron, two protons and neutron, respectively, and $E_b = -2.224$ MeV is the binding energy of the deuteron.

If one takes into account the above conservation laws and the relation $\varphi_{12} = \varphi_1 - \varphi_2$, the number of independent variables can be reduced to the following five: $E_1, E_2, \theta_1, \theta_2, \varphi_{12}$. Due to the fact that in the discussed here experiment the proton energies (E_1, E_2) and their directions (polar θ_1, θ_2 and azimuthal φ_1, φ_2 angles) were determined, the final state of the reaction is over-completely reconstructed. After eliminating E_3 in Eq. 2.1 one obtains in the non-relativistic case the following formula:

$$\begin{aligned} (m_1 + m_3)E_1 + (m_2 + m_3)E_2 - 2\sqrt{m_d m_1 E_d E_1} \cos \theta_1 - 2\sqrt{m_d m_2 E_d E_2} \cos \theta_2 \\ + 2\sqrt{m_1 m_2 E_1 E_2} \cos \theta_{12} = m_3 E_b + (m_3 - m_d)E_d, \end{aligned} \quad (2.2)$$

where:

$$\cos \theta_{12} = \cos \theta_1 \cos \theta_2 + \sin \theta_1 \sin \theta_2 \cos(\varphi_1 - \varphi_2),$$

m_d - deuteron mass,

m_1, m_2 - proton masses,

m_3 - neutron mass.

If one assumes $m_1 = m_2 = m_3 \equiv m$ and $m_d \equiv 2m$, Eq. 2.2 simplifies to:

$$E_1 + E_2 - \sqrt{2E_d E_1} \cos \theta_1 - \sqrt{2E_d E_2} \cos \theta_2 + \sqrt{E_1 E_2} \cos \theta_{12} = \frac{E_b - E_d}{2}, \quad (2.3)$$

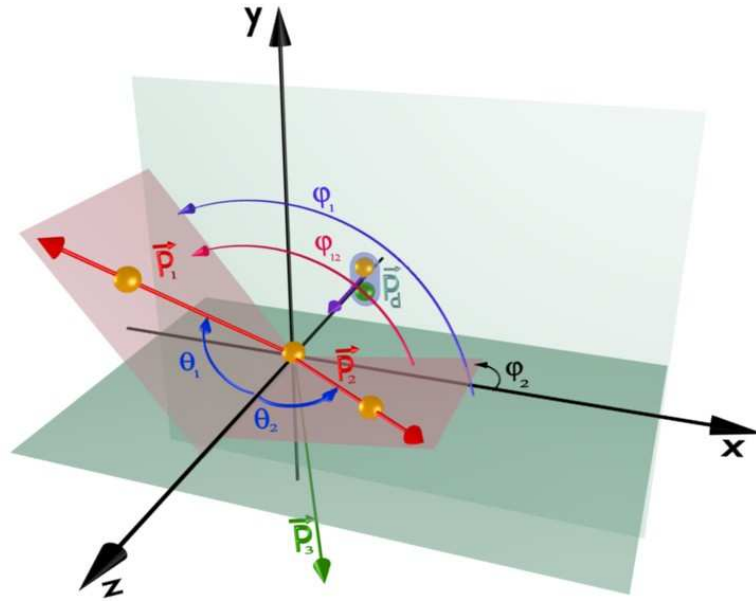


Figure 2.1: A schematic view of the breakup reaction with indicated momenta of the incoming deuteron (\vec{p}_d) and the outgoing protons (\vec{p}_1 , \vec{p}_2) and neutron (\vec{p}_3). The polar (θ_1 and θ_2) and azimuthal (φ_1 and φ_2) angles of the two protons are defined in the chosen reference frame, as well as their relative angle $\varphi_{12} = \varphi_1 - \varphi_2$.

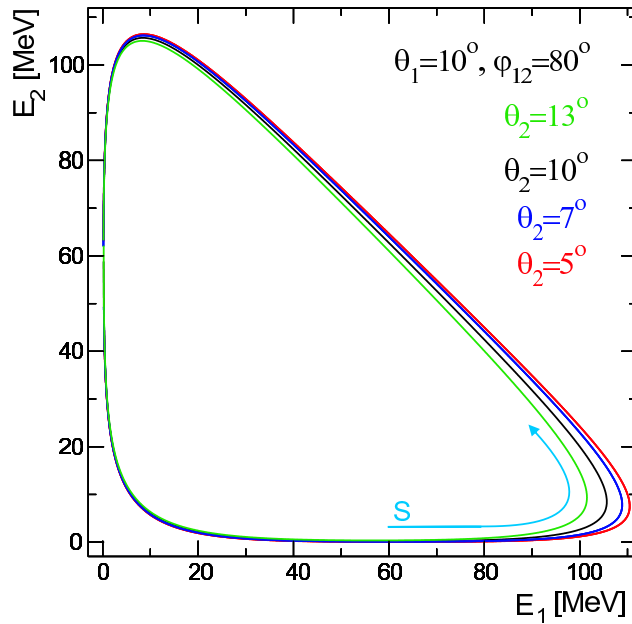


Figure 2.2: Sample set of kinematical relations between the energies of the two protons for different configurations. The blue arrow represents the arc-length variable S for one of these kinematics, with its zero value chosen at the minimum of E_2 .

what, for one set of angles, is the equation relating the energies of the two measured protons. This relation corresponds to the so-called *kinematical curve* i.e. dependency between the energies E_1 and E_2 of the outgoing protons for a chosen kinematical configuration $\theta_1, \theta_2, \varphi_{12}$. A few examples of the kinematical curves are shown in Fig. 2.2. The S – *variable* defines the arc-length along the individual kinematical curve and is represented in Fig. 2.2 by the arrow starting at the minimal energy E_2 , what defines $S=0$.

2.2 Elastic scattering process

Elastic $d-p$ scattering reaction is described by two-body kinematics i.e. two particles are present in the final state of the reaction. In this experiment the initial conditions were given as $(m_{deut}, m_{prot}, \vec{p}_{deut}, \vec{p}_{prot} = 0)$, where the m_{deut}, m_{prot} are masses of the proton and deuteron and $\vec{p}_{deut}, \vec{p}_{prot}$ are the momenta of these particles. The projectile is heavier than the target $m_{deut} > m_{prot}$, thus the obtained from the conservation of energy and momentum laws kinematical relations describe the so-called inverse kinematic. In Fig. 2.3 such kinematical curves are presented with two distinguished branches. Moreover, the detector acceptance is marked with the colour dashed lines. The “first” branch refers to the situation when the high-energy deuteron is detected, whereas the proton is emitted outside the detector acceptance. The “second” branch is related to the high-energy proton accompanied by the low-energy deuteron. In a certain range of the polar angles both particles reach the detector. In general, if the final state particle is chosen to be detected at an angle θ_1 , two-body kinematics determine the unique angle θ_2 at which the other particle emerges as well as both kinetic energies.

2.3 Cross section and analyzing powers

If one considers a reaction with a polarized spin $J=1$ projectile and an unpolarized target with three particles in the final state, the general formula for the cross section $\sigma(\xi, \varphi_1, \beta)$ in Cartesian coordinate system depends on the cross section for an unpolarized beam $\sigma_0(\xi)$, vector analyzing powers $A_x(\xi), A_y(\xi), A_z(\xi)$ and tensor analyzing powers $A_{xy}(\xi), A_{yz}(\xi), A_{xz}(\xi), A_{xx}(\xi), A_{yy}(\xi), A_{zz}(\xi)$. ξ represents a set of kinematical variables, which in the case of the breakup reaction is $\xi = (\theta_1, \theta_2, \varphi_{12}, S)$. β angle describes the orientation of the projectile spin with respect to its momentum. Then, the general cross section formula can be expressed as follows [34]:

$$\begin{aligned} \sigma(\xi, \varphi_1, \beta) = & \sigma_0(\xi) \cdot \left[1 - \frac{3}{2} \sin \beta \sin \varphi_1 P_z A_x(\xi) + \frac{3}{2} \sin \beta \cos \varphi_1 P_z A_y(\xi) + \frac{3}{2} \cos \beta P_z A_z(\xi) \right. \\ & - \sin^2 \beta \cos \varphi_1 \sin \varphi_1 P_{zz} A_{xy}(\xi) + \sin \beta \cos \beta \cos \varphi_1 P_{zz} A_{yz}(\xi) - \sin \beta \cos \beta \sin \varphi_1 P_{zz} A_{xz}(\xi) \\ & \left. + \frac{1}{2} (\sin^2 \beta \sin^2 \varphi_1 - \cos^2 \beta) P_{zz} A_{xx}(\xi) + \frac{1}{2} (\sin^2 \beta \cos^2 \varphi_1 - \cos^2 \beta) P_{zz} A_{yy}(\xi) \right]. \end{aligned} \quad (2.4)$$

The angles and frame definitions are consistent with the Madison Convention [35]. For the beam polarization normal to its momentum ($\beta = 90^\circ$), as it was used in the experiment, Eq. 2.4 can be rewritten as:

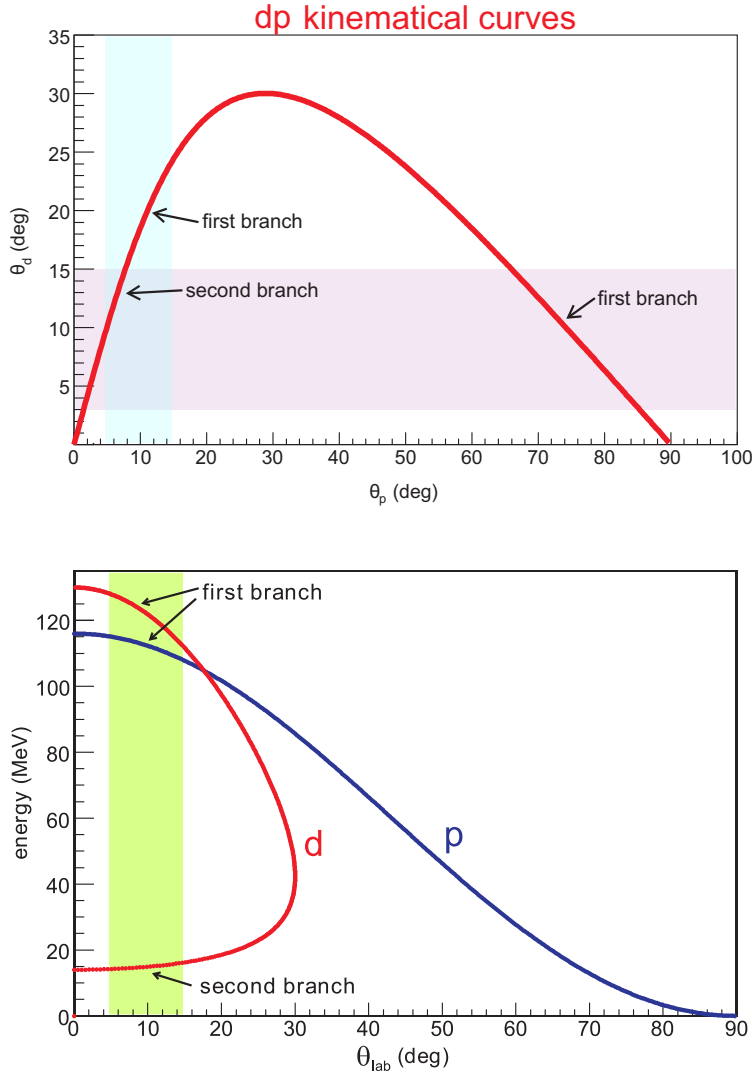


Figure 2.3: The elastic $d-p$ scattering kinematical relations presented as the dependencies of θ_d vs. θ_p and kinetic energy vs. θ_{lab} . The arrows indicate the part of the kinematical curves referred to as “first” and “second” branches within the detector acceptance of the present experiment (marked by dotted lines).

$$\begin{aligned} \sigma(\xi, \varphi_1) = \sigma_0(\xi) \cdot & \left[1 - \frac{3}{2} \sin \varphi_1 P_z A_x(\xi) + \frac{3}{2} \cos \varphi_1 P_z A_y(\xi) - \cos \varphi_1 \sin \varphi_1 P_{zz} A_{xy}(\xi) \right. \\ & \left. + \frac{1}{2} \sin^2 \varphi_1 P_{zz} A_{xx}(\xi) + \frac{1}{2} \sin^2 \varphi_1 P_{zz} A_{yy}(\xi) + \frac{1}{2} \cos^2 \varphi_1 P_{zz} A_{yy}(\xi) \right]. \end{aligned} \quad (2.5)$$

P_z and P_{zz} are the vector and tensor polarizations of the deuteron beam, and can be defined in the source coordinate system by the formulae:

$$P_z = \frac{N_+ - N_-}{N_+ + N_0 + N_-}, \quad (2.6)$$

$$P_{zz} = \frac{N_+ + N_- - 2N_0}{N_+ + N_0 + N_-}, \quad (2.7)$$

where N_+ , N_0 , N_- are the numbers of particles with the spin projection m_I : $+1$, 0 , -1 , respectively.

The analyzing powers which appear in Eqs. 2.4 and 2.5 possess the following properties:

- the tensor A_{xx} , A_{yy} , A_{zz} components satisfy the identity:

$$A_{xx}(\xi) + A_{yy}(\xi) + A_{zz}(\xi) = 0, \quad (2.8)$$

- from parity conservation result the following symmetry rules:

$$\begin{aligned} A_x(\theta_1, \theta_2, S, \varphi_{12}) &= -A_x(\theta_1, \theta_2, S, -\varphi_{12}), \\ A_y(\theta_1, \theta_2, S, \varphi_{12}) &= A_y(\theta_1, \theta_2, S, -\varphi_{12}), \\ A_{xx}(\theta_1, \theta_2, S, \varphi_{12}) &= A_{xx}(\theta_1, \theta_2, S, -\varphi_{12}), \\ A_{xy}(\theta_1, \theta_2, S, \varphi_{12}) &= -A_{xy}(\theta_1, \theta_2, S, -\varphi_{12}), \\ A_{yy}(\theta_1, \theta_2, S, \varphi_{12}) &= A_{yy}(\theta_1, \theta_2, S, -\varphi_{12}), \end{aligned} \quad (2.9)$$

- as a consequence of the above conditions it follows that the A_x and A_{xy} analyzing powers vanish for the coplanar configurations ($\varphi_{12} = 180^\circ$), as well as for the symmetric ones ($\theta_1 = \theta_2$).

For the elastic scattering process, which is the coplanar case (i.e. the relative azimuthal angle $\varphi_{12} = 180^\circ$) with the final state described by only two independent variables, usually the polar and azimuthal angles θ , φ of one of the reaction products, Eq. 2.5 takes a simplified form:

$$\sigma(\theta, \varphi) = \sigma_0(\theta) \cdot \left[1 + \frac{3}{2} \cos \varphi P_z A_y(\theta) + \frac{1}{2} \sin^2 \varphi P_{zz} A_{xx}(\theta) + \frac{1}{2} \cos^2 \varphi P_{zz} A_{yy}(\theta) \right], \quad (2.10)$$

where now all observables (σ , σ_0 , A_y , A_{xx} , A_{yy}) refer to the elastic scattering.

The above formula can be expressed in spherical coordinates, also very commonly used. The relation between the analyzing powers in the spherical and Cartesian coordinates can be found in [34], [36]. Rewritten in that representation Eq. 2.10 takes the form:

$$\sigma(\theta, \varphi) = \sigma_0(\theta) \cdot \left[1 + iT_{11}(\theta) \sqrt{3} P_z \cos \varphi - T_{22}(\theta) \frac{\sqrt{3}}{2} P_{zz} \cos 2\varphi - T_{20}(\theta) \frac{\sqrt{2}}{4} P_{zz} \right]. \quad (2.11)$$

Chapter 3

Theoretical approaches to the 2N and 3N systems

Properties of few-nucleon systems at medium energy regime are determined mainly by pairwise NN interactions. The long range part of the NN potential is described with the meson-exchange theory, whereas the short range is constructed using phenomenological approaches, with the aim to reproduce a rich set of the NN scattering data. This aim was achieved with an impressive accuracy of χ^2 per data point very close to one. This kind of a new generation forces, developed within the meson-exchange theory (one-boson exchange, OBE, or multi-particle exchanges between nucleons), which was first proposed by Yukawa (see Fig. 3.2, left), are referred to as realistic NN models. They operate on purely nucleonic degrees of freedom considering the nucleons as stable objects. Nowadays, there exist many so-called realistic NN potential models, like AV18 [32], CD Bonn [37], Nijmegen I and II [38].

There exists also a method of extension of the above picture, in which one Δ isobar is treated as a stable particle. This approach, called coupled-channels, is based on the realistic CD Bonn potential [2, 3].

An alternative and more fundamental approach comes from Chiral Perturbation Theory (ChPT), which considers the strong forces between the nucleons as interaction between their constituent quarks. This effective field theory for NN interaction links the quantum chromodynamics (QCD) and NN interaction phenomenology in the non-perturbative energy regime.

An obvious step in testing those 2N force models is turning into systems with more than two nucleons interacting and checking whether the above models correctly reproduce experimental data in such environment. The simplest and nontrivial one is the three-nucleon (3N) system.

The realistic NN forces fail to provide experimental binding energies of few-nucleon systems and lead to underbinding of 0.5-1 MeV in the cases of 3H and 3He , 2-4 MeV for 4He , [39] and for systems up to $A=8$, the underbinding is ≈ 10 MeV. Moreover, the realistic NN potentials also do not reproduce the data from nucleon-deuteron (Nd) elastic scattering for nucleon energies larger than 60 MeV [8, 12, 13, 22, 40–42], especially at the minima of the cross sections, see Fig. 3.1. The most natural candidate to explain those disagreements is *three nucleon force* (3NF), which only affects observables in processes involving three or more nucleons. There are different models of 3NF, usually refined versions of the Fujita-Miyazawa force [43], in which one of the nucleons is excited into an

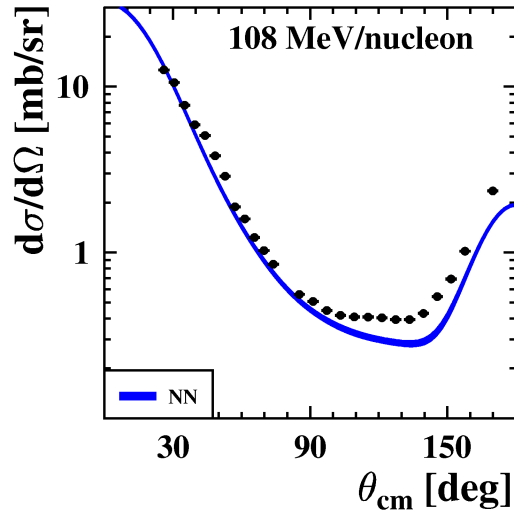


Figure 3.1: Comparison of the differential cross section data with the theoretical predictions for the Nd elastic scattering at 108 MeV/nucleon. The dark blue band presents theoretical calculation based on the realistic NN potentials. The experimental results (black circles) are Nd elastic scattering data [13]. Figure adopted from [13].

intermediate Δ via 2π -exchange with both nucleons, see Fig. 3.2 (middle). In a more general case the scheme of interaction is as follow: a pion emitted by one nucleon interacts in a complicated way with a second nucleon and then is absorbed by a third nucleon, see Fig. 3.2 (right). The realistic potentials are supplemented by this additional 3NF dynamic, what leads to appearance of a new term in the potential energy, which depends in an irreducible way on the degrees of freedom of all three participating nucleons. In the case of the alternative coupled-channel approach, the 3N system is described with the explicit treatment of the degrees of freedom of a single Δ isobar excitation. In ChPT framework the non-zero 3NF appears naturally at the next-to-next-to-leading order (NNLO).

In order to obtain in a theoretical way observables which could then be used for interpretation of the measured 3N system data in terms of nuclear force properties, a new formalism was introduced by Faddeev [44]. This method of exact treatment of the 3N scattering problem with any short range interaction is a tool which allows to obtain the theoretical predictions with high accuracy, not biased by (numerical) simplifications. Quantitative conclusions are nowadays possible due to the rigorous technique of solving the Faddeev equations for the 3N system [16].

A brief descriptions of the above mentioned approaches is presented below.

3.1 Realistic potentials

The realistic NN potentials used nowadays, like charge dependent (CD) Bonn [37], AV18 [32], Nijm I and Nijm II [38], describe the long range part of the interaction with the use of meson-exchange formalism, whereas the implemented short range part is phenomenological. These 2N forces can be combined with the recent version of the 2π -exchange Tucson-Melbourne (TM) 3NF model [17, 18, 20], called TM99 3NF. The general expres-

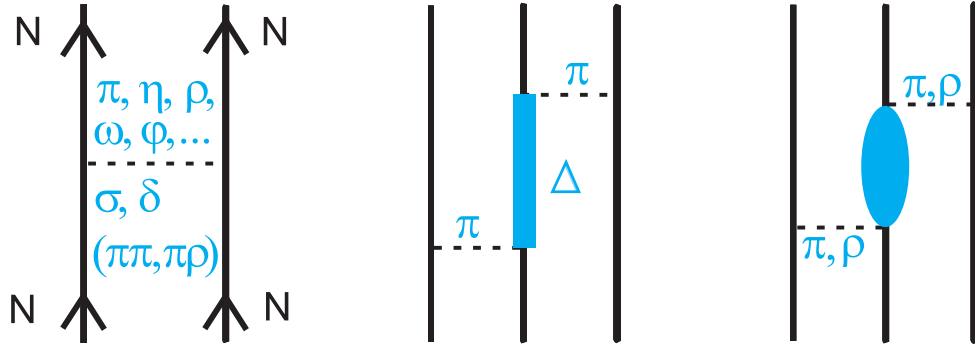


Figure 3.2: Schematic diagrams of the structure of the nucleon-nucleon interaction (left) and of the three-nucleon force: the Fujita-Miyazawa 3NF (middle) and a general 3NF model via two-meson exchange (right).

sion for the 2π -exchange 3NF in the TM framework contains four coefficients a , b , c and d , which are obtained by fitting the π -N scattering data and refer to three terms [45]:

1. a-term - describes the π -N S-wave scattering,
2. b, d-terms - are related to π -N P-wave scattering with the main process $\pi N \rightarrow \Delta \rightarrow \pi N$,
3. c-term - the term which vanishes due to chiral symmetry.

Besides these parameters the TM99 3NF model contains one additional cut-off parameter Λ_{TM} , expressed in units of the pion mass m_π . Value of Λ_{TM} is adjusted to reproduce the 3H binding energy separately for different NN forces.

When the 3N system dynamics is described with the AV18 NN potential, it is also combined with the Urbana IX 3NF [19]. This force is based on the Fujita-Miyazawa model of an intermediate Δ -excitation in the 2π exchange and includes also a phenomenological short-range part. More detailed description of the formalism of the 3N system with the realistic potentials combined with 3NF could be found in [46], [16].

3.2 Coupled-channel formalism (CCP)

The approach, presented in [2, 3], is based on the realistic CD Bonn potential. In this case the Δ resonance is treated as a stable particle, in contrary to the realistic CD Bonn potential mentioned before. The two nucleon channels are coupled to those in which one nucleon is excited and forms the Δ isobar - see Fig. 3.3. In the coupled-channel potential contributions of the transitions between the NN and $N\Delta$ states, as well as the exchange N- Δ potential from direct interaction of the N- Δ states are included.

For the 3N system, creation of a Δ -containing state yields an effective 3NF (see Fig. 3.4, right), but also so-called two-baryon dispersion (Fig. 3.4, left). These two contributions usually compete, therefore the net effects of including Δ isobar in the potential are smaller

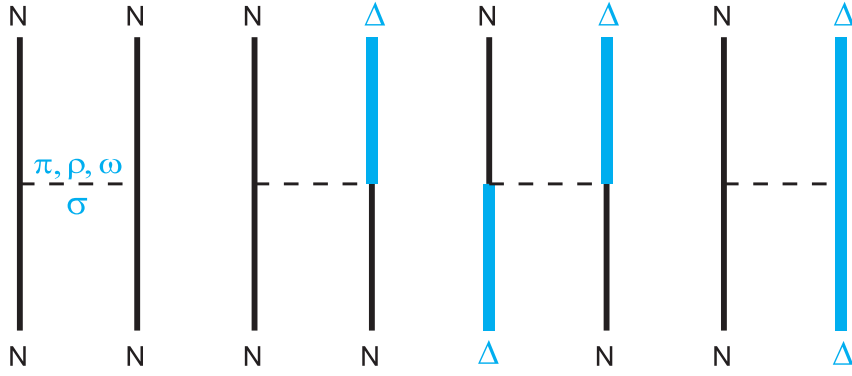


Figure 3.3: Channels considered in construction of the potential, in which single Δ -isobar degrees of freedom are explicitly taken into account.

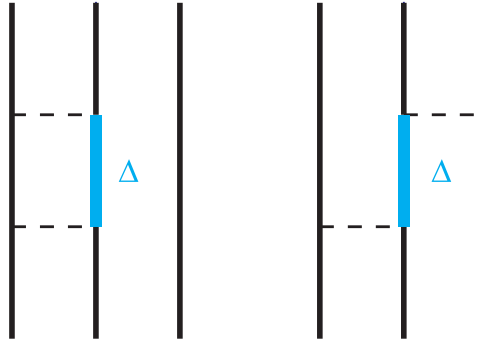


Figure 3.4: Three-baryon dispersion effect arising within the coupled channel potential: two-baryon dispersion (left) and the effective three-body force (right).

than for approaches with the phenomenological 3NF's.

In this framework the rigorous calculations including the Coulomb interaction have been performed, see Sec. 3.4.

3.3 Chiral Perturbation Theory

The framework is based on the Lagrangian for Goldstone bosons (pions) and matter field (nucleons), which is consistent with the broken chiral symmetry of the QCD [47, 48]. Two types of interaction are assumed: long range pion(s) exchanges, with the crucial role of the chiral symmetry, and contact interactions, with the associated low energy constants (LEC). Here, the nuclear potential is obtained in a way of a systematic expansion in terms of momentum variable: $(Q/\Lambda)^\nu$, with Q describing a characteristic momentum of the interacting system, Λ is connected to the chiral symmetry breaking scale of about 1 GeV and ν is a given expansion order. A non-vanishing 3NF appears at the NNLO ($\nu=3$) and the full potential at this order can be then written as follow (see Fig. 3.5):

$$V = V^0 + V^2 + V^3 + V^{3NF}, \quad (3.1)$$

where

V^0 - LO ($\nu=0$) is obtained by 1π -exchange part and two contact interactions; it contains

| | Two - nucleon force | Three - nucleon force | Four - nucleon force |
|---------------|---------------------|-----------------------|----------------------|
| Q^0 LO | | — | — |
| Q^2 NLO | | — | — |
| Q^3 N2LO | | | — |
| Q^4 N3LO | | | |

Figure 3.5: The graphs which appear at different orders and contribute to the ChPT NN potential. The 3NF arises at the NNLO. Figure adopted from [47].

two LEC's,

V^2 - NLO ($\nu=2$) is given by 2π -exchanges; it contains seven new LEC's and corrections to 1π -exchange are introduced,

V^3 - NNLO ($\nu=2$) is expressed by subleading 2π -exchange potential with three new LEC's and corrections to 1π -exchange,

V^{3NF} - is appearing in three topologies and with two LEC's.

The LEC's appearing at LO and NLO are obtained by fitting the theoretical ChPT NN potential to the NN data, whereas the three LEC's characterizing NNLO potential are determined from πN scattering data [26, 27].

This method is unique because it provides a possibility to estimate uncertainties of the obtained predictions. To this purpose the calculations are performed with a few combinations of the two cut-off parameters $[\Lambda, \tilde{\Lambda}]$, which are used for regularization of the obtained potentials. An estimation of uncertainties of the theoretical observables is obtained due to reasonable choice of the variation intervals of both cut-offs. Up to now within the ChPT framework a complete description of the NN and 3N systems has been established at the NNLO. Recently calculations for the NN system have been performed at the next higher order, N3LO, however, the graphs corresponding to 3NF have not been included yet. For more details on ChPT see also [49, 50], [28], [51].

3.4 Coulomb interaction

The Coulomb force due to its infinite range and slow decrease with the distance of the two charges is very difficult to include in the theoretical description in the 3N continuum. The theoretical efforts to overcome these problems have long history (see [29]) and now some important progress is being achieved. The Coulomb interaction has been included in

the coupled-channel approach, as well as in the calculations with the AV18 NN potential combined with the Urbana IX 3NF.

In these calculations a screened Coulomb potential, with the screening radius much larger than the range of the nuclear potential is used. Then the standard methods for the short-range forces are applied and the obtained results are corrected to match the un-screened limit. Recently this idea has been used in the coupled-channel potential and AV18 NN potential combined with the Urbana IX force calculations, and worked out to a form providing relevant results for the 3N bound states, elastic proton-deuteron scattering [29, 31, 52] and for the pd breakup reaction [31, 53]. At 130 MeV the predicted effects for the breakup process are sizable for cross sections in some regions of the phase space [29, 30], [54] and much less prominent for the analyzing powers [55].

3.5 Acting of 3N forces

For 3N and 4N systems the correct binding energies were obtained by introducing the TM99 or Urbana IX 3NFs. The combined models of NN and 3N potentials (adjusted to reproduce the 3H binding energy) correctly described the 3He , 4He [6] bound states, as well as the low energy levels of light ($A \leq 8$) nuclei. Similar conclusions are also obtained within the ChPT and coupled-channel approaches. In the case of ChPT framework inclusion of 3NF graphs leads to an improvement in description of few-nucleon bound states [56], whereas for the coupled-channel framework the binding energies of 3H , 3He are much closer to the experimental values when Δ -isobar contributions are included [2]. A brief summary is presented in Tab. 3.1. Binding energies have shown the importance of 3NF for the nucleus. Further consequences originating from introducing additional dynamics into 3N system are visible in the Nd elastic scattering data. A large part of discrepancies appearing in the Nd elastic scattering cross sections can be removed when the 3NF is included in the 3N Hamiltonian within different frameworks. In several cases where the NN forces fail to reproduce the observables, the implemented 3NF leads to significant improvements [7, 8, 10, 12–14], see sample in Fig. 3.6, left. Unfortunately, for

| potentials | E_B [MeV] 3H | E_B [MeV] 3He | E_B [MeV] 4He |
|--------------|------------------------|-------------------------|-------------------------|
| CDBonn | -8.01 | -7.29 | -26.3 |
| AV18 | -7.62 | -6.92 | -24.3 |
| Nijm II | -7.66 | -7.01 | -24.6 |
| CDBonn+TM99 | -8.48 | -7.73 | -29.2 |
| AV18+TM99 | -8.48 | -7.76 | -28.8 |
| AV18+UIX | -8.48 | -7.76 | -28.5 |
| Nijm II+TM99 | -8.39 | -7.72 | -28.5 |
| CC CDBonn | -8.36 | -7.64 | -28.4 |
| Experiment | -8.48 | -7.72 | -28.3 |

Table 3.1: Binding energies E_B of 3H , 3He and 4He for various realistic potentials with and without Tucson-Melbourne and Urbana IX three nucleon forces. The experimental values are listed in the last row.

various elastic Nd scattering polarization observables discrepancies between the theoretical predictions and experimental data are still present. In some cases inclusion of 3NF do not improve the theoretical descriptions enough [7, 9, 10, 13, 14] to reproduce the experimental points or the data are remarkably well described by calculations based on NN interaction only and including 3NF is unnecessary (see Fig. 3.6, right). For the ChPT framework, the existing discrepancies indicate the necessity for including the higher order (at least $N^3\text{LO}$) terms for the 3N continuum. In general one can suspect that the spin structure of the current 3NF models is not yet properly understood.

Relying on the above facts one can conclude that the existing theoretical models still need more high precision data and it is natural to turn into more complicated Nd breakup reaction, where the final state offers a ground to detailed investigation of 3NF properties, especially of the spin structure of the 3NF. Also for this process precise theoretical predictions for observables are available via exact solutions of the 3N Faddeev equations for any NN interaction, even with the inclusion of 3NF model [16], as well as with the Coulomb force, e.g. [53].

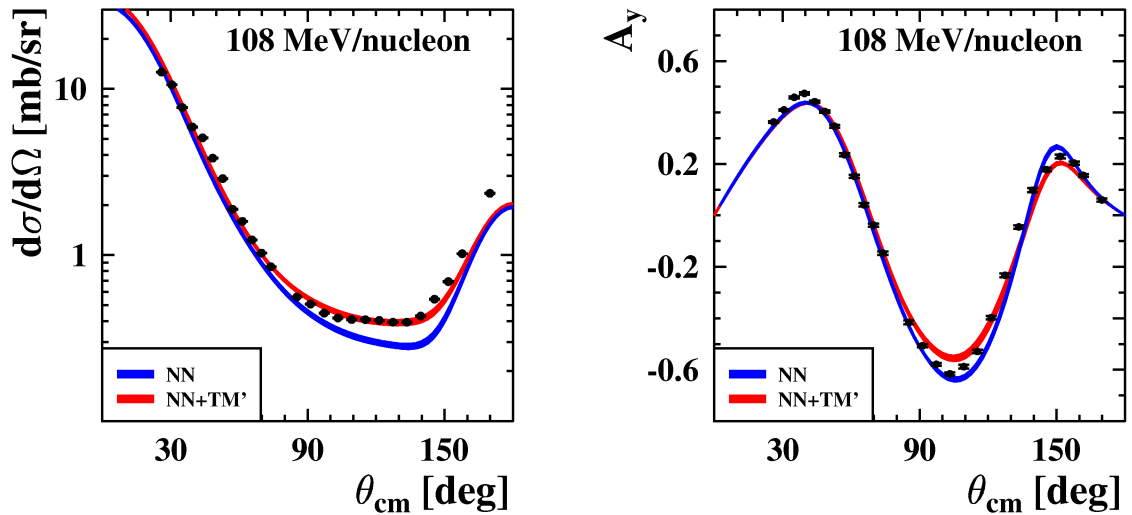


Figure 3.6: Comparison of the differential cross section data (left) and polarization observable A_y (right) with the theoretical predictions for the Nd elastic scattering at 108 MeV/nucleon. The dark blue band presents theoretical calculation based on the realistic NN potentials, whereas the red one shows the predictions of the NN potentials combined with the TM99 3NF. The experimental results (black circles) are the Nd elastic scattering data [13]. Figures adopted from [13].

Chapter 4

Experimental setup

The data presented in this dissertation come from the experimental runs committed to investigation of the breakup process ${}^1H(\vec{d}, pp)n$, carried out at the Forschungszentrum Jülich GmbH, Germany in 2006 and 2007. The experiments were performed with the use of COSY (COoler SYnchrotron) accelerator and Germanium Wall detection system. The experiment was placed outside the storage ring of the accelerator in the Big Karl spectrometer area.

4.1 COSY accelerator

The cooler synchrotron COSY [57] is a storage ring device used to accelerate polarized and unpolarized beams of protons and deuterons. Floor plan of the facility is presented in Fig. 4.1. The ion source provides polarized and unpolarized ions of H^- and D^- , which are preaccelerated with the use of the cyclotron JULIC up to the energies of about 45 MeV/A. Then the particles are guided through a 100 m long injection beam line, injected into the COSY ring and accelerated up to the required energy of 130 MeV. After the acceleration stage the beam was guided through extraction beam lines to the experimental area of the Big Karl and focused on the target. A full machine cycle (spill) starts from injection of the beam into COSY and is terminated after the full extraction process. A typical spill lasts between 5 seconds and one hour.

The synchrotron consists of 24 dipole and 56 quadrupole magnets, which keep the particles trajectories during acceleration process, as well as sextupole magnets, which enable the beam deflection and as a result improve the beam optics. Moreover, COSY is equipped with the electron and stochastic cooling systems in order to improve beam parameters, what is important for high-precision experiments. For protons or deuterons with momentum up to 600 MeV/c the electron cooling may be applied (energy of electrons is up to 100 keV). For more energetic particles (1500 - 3400 MeV/c) the stochastic cooling can be used, what minimizes the beam dimensions longitudinally and transversally.

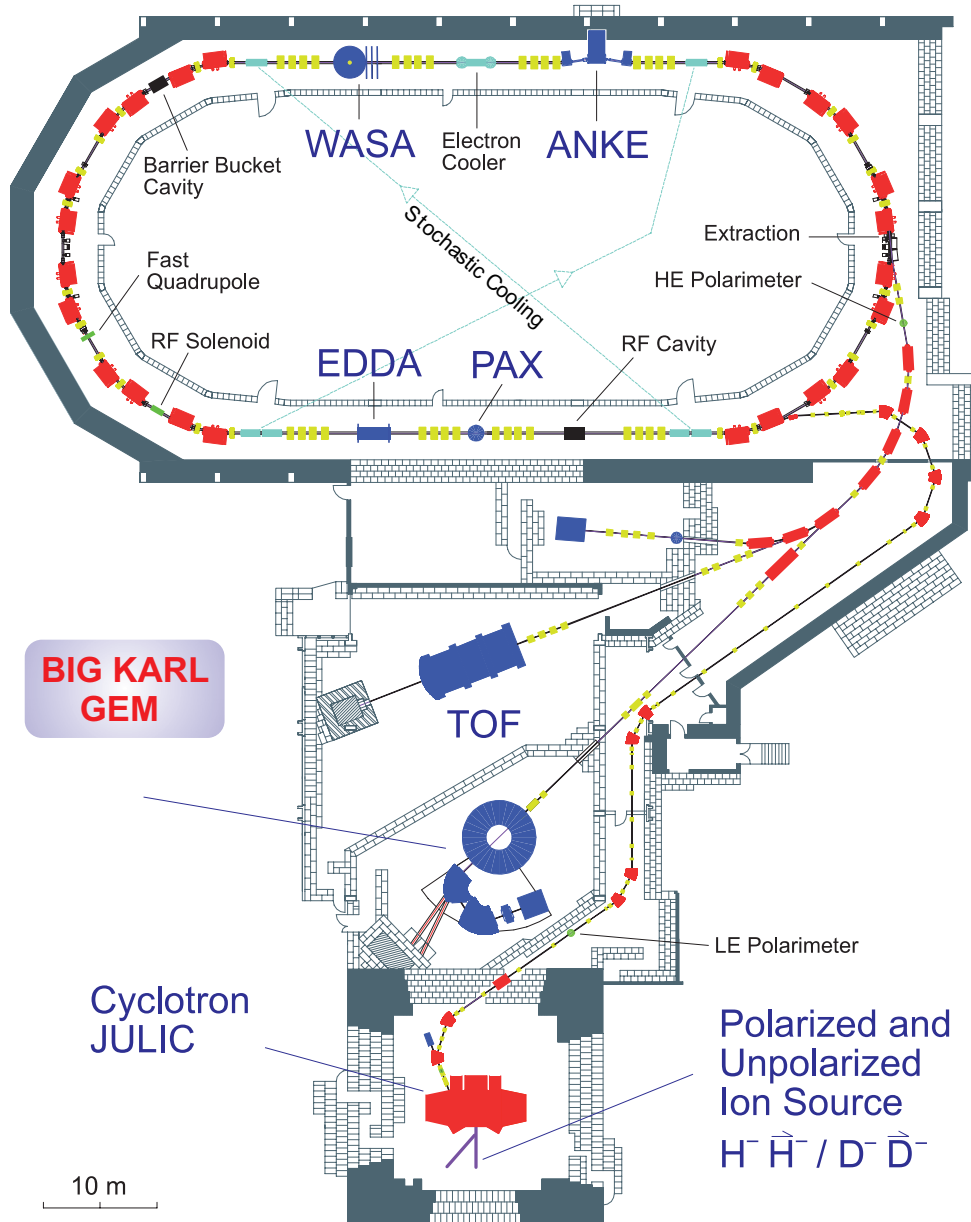


Figure 4.1: A floorplan of the COoler SYnchrotron COSY with the experimental facilities.

4.2 Production of a polarized deuteron beam

The polarized ion source of COSY is a Colliding Beam source (CBS) type, which is able to produce polarized proton and deuteron beams with all possible combinations of vector and tensor polarizations.

The polarized ion source, presented schematically in Fig. 4.2, consists of three major groups of components: the pulsed atomic beam source, the cesium beam source and the charge-exchange and extraction region. In a first step of production of the polarized beam, the $H_2(D_2)$ gas molecules are dissociated into atoms in an inductively coupled

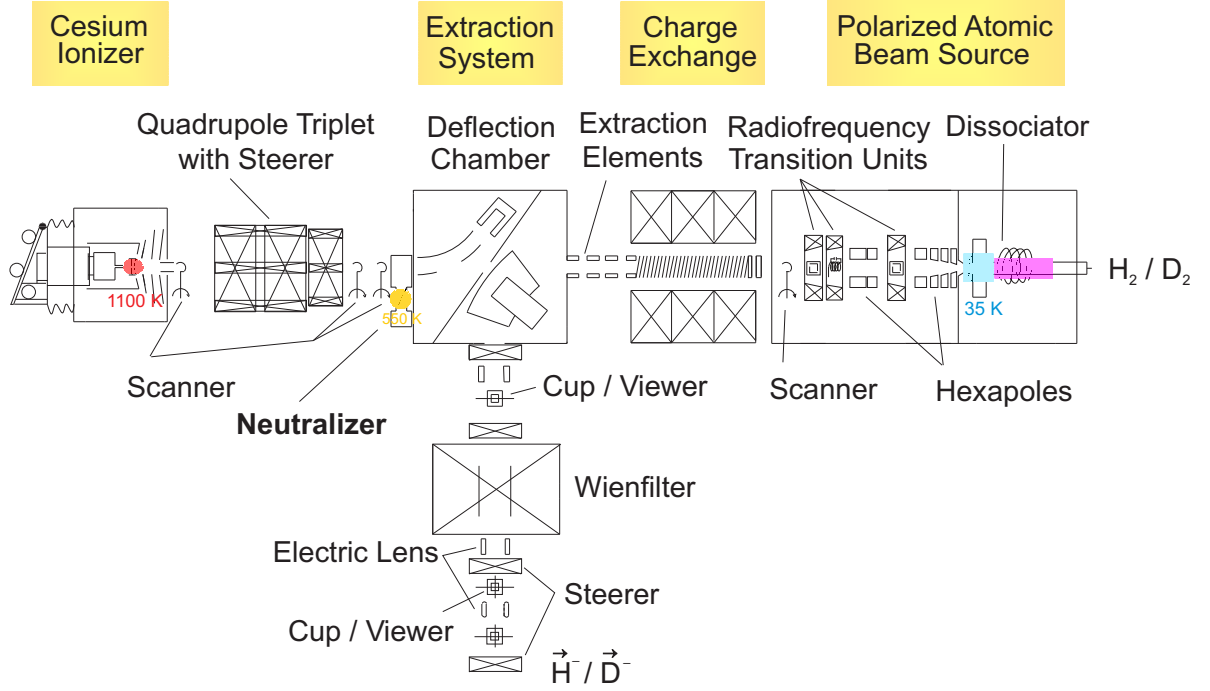
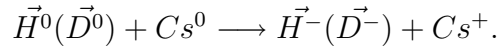


Figure 4.2: The polarized ion source of COSY.

rf discharge and cooled to about 35 K by passing through an aluminum nozzle. Next step is production of the electron state polarization of the atoms with the use of a first sextupole. Due to the atoms magnetic dipole moments some of them are focused (only atoms with the electron spin state $m_J = +1/2$) by a second sextupole into the radio frequency transition area, where the nuclear polarization is produced. Afterwards, in the charge-exchange region, the nuclear polarized hydrogen atoms collide with the neutral Cs:



The fast cesium beam needed for the above charge exchange reaction in the solenoid, is produced inside a vacuum chamber in two steps. First, Cs vapor is thermally ionized on a hot (1100° C) porous tungsten surface at a potential of about 45 kV and the Cs^+ fast beam obtained in this way is focused to the charge exchange region with the use of quadrupole triplet system. Then, inside a neutralizer, placed between the quadrupoles and the cesium deflector, the conversion to neutral Cs^0 occurs. These high speed atoms reach the charge exchange region passing through the deflection chamber and collide with the atomic $\vec{H}^0(\vec{D}^0)$ beam with high nuclear polarization.

The obtained $H^-(D^-)$ ions are extracted with the use of electric field into the deflection chamber, where they are subsequently deflected by 90° in the magnetic deflector and on the way to the extraction system pass a Wien filter. This filter may be rotated around the beam axis and the proper spin alignment for injection into the cyclotron Julic can be selected.

The $H^-(D^-)$ beam is finally injected into the Julic cyclotron at the energy of 4.5 keV and preaccelerated up to energy of 45 MeV/A. Next, the $H^-(D^-)$ beam is guided through the beam lines and reaches the stripping injector, where the $H^-(D^-)$ anions are stripped off two electrons and injected into the COSY accelerator. More detailed description of

CBS can be found in [58], [59], [60].

4.3 GEM facility

The GEM (Germanium Wall and Electromagnetic Spectrometer) detection system operated in 2006 and 2007 consisted of three high-purity, semiconductor position sensitive germanium detectors (GeWall) and the Big Karl spectrometer. The technical details can be found in [61], [62] as well as in [63], [64], [65].

The Big Karl was one of the external facilities, which was using the extracted beam. For such experiments one of the serious problems in obtaining beam with very good properties is beam-halo existence, which induces substantial background. To suppress this effect, the electron cooling was used during the acceleration process. Study of the beam-halo effect on GeWall detectors was performed during the first test run in 2006. In spite of the fact that the deuteron beam was finally focused on the target to a spot described by $\sigma \approx 1.0$ mm, the tails of the direct beam were still present on the detector. Therefore, the experiment was utilizing a veto counter, which limited the acceptance of the beam to its intense core.

In the presented here experiments the spill duration was about one minute and the deuteron beam with the intensity of $2 \cdot 10^7/s$ was focused to a spot with dimensions (rms): 1.1 mm on x- and 1.0 mm on y-axis.

4.3.1 Big Karl spectrometer and a Dipole Exit counter

The Big Karl spectrometer consisted of two dipole and three quadrupole magnets and focused particles scattered at polar angles less than 3^0 . In the presented here experiments it was used to transport the primary deuteron beam to the remote beam dump. The outer yoke of the first dipole was equipped with an exit window, which enabled the primary beam to leave the detection system without producing additional background. In order to monitor the beam intensity (luminosity counters, see 4.3.3) a measurement of the direct deuteron beam was necessary. With the use of an additional scintillator detector, which was called Dipole Exit (*DE*) counter and was placed at the exit window, the measurements of the direct beam intensity was possible.

4.3.2 Target section

The target construction and operation was worked out at the Institute of Nuclear Physics (IKP) of the Forschungszentrum Jülich [66], [67]. As a target a cylindrical copper cell with dimensions: 6 mm diameter and 2 mm thickness, filled with liquid hydrogen was used. The flat taps were closed by the windows made out of $0.9 \mu\text{m}$ thin mylar foil (possibly thin in order to reduce background reactions). To achieve proper pressure conditions inside the cell, a mechanical stabilization system was applied, which allowed to choose the working pressure of 0.2 mbar. Under this pressure hydrogen stays liquid in the temperature range 14 K - 16 K. A schematic picture of the target area with the GeWall detectors is presented in Fig. 4.3.

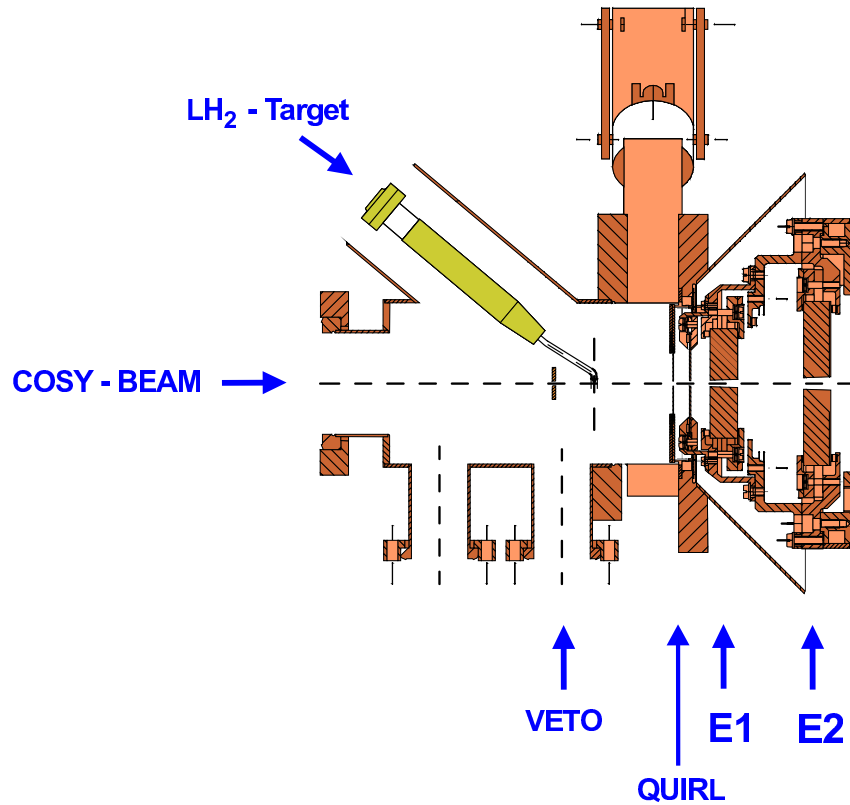


Figure 4.3: A schematic view of the target and the GeWall detectors inside the cryostat.

4.3.3 Veto and luminosity counters

Except the elements forming the main part of the detection system, additional detectors were applied to control the reaction yield.

In order to decrease the trigger rate and select the deuterons which were bombarding center of the target, a 2 mm thick scintillating veto counter with the central hole of 4 mm diameter was mounted in front of the LH_2 cell, see Fig. 4.4. The signal from the veto counter was used in trigger conditions for the data acquisition system, see section 4.3.5. Additional detectors (telescopes called Lumi Right- L_R and Lumi Left- L_L , see also Fig. 4.4) placed outside the scattering chamber were used for beam intensity monitoring. Each telescope consisted of two paddles of scintillators acting in coincidence. Simultaneous measurement of the primary beam with the use of the DE counter (see Sub. 4.3.1) and the deuterons elastically scattered from the target allowed to obtain dependence of the beam intensity as a function of the number of counts registered in L_R or L_L . The measurements were performed with different beam intensities, reduced to the level at which DE scintillators work without saturating the photomultipliers (about 10^5 d/s). The dependence obtained in this way is linear over 5 orders of beam intensity and this gives a possibility to calculate the number of deuterons hitting the target by extrapolation to higher beam intensities.

4.3.4 Germanium Wall

For registering the charged reaction products Germanium Wall detectors were used. The set of HP germanium detectors had a radial symmetry with respect to the beam axis. A

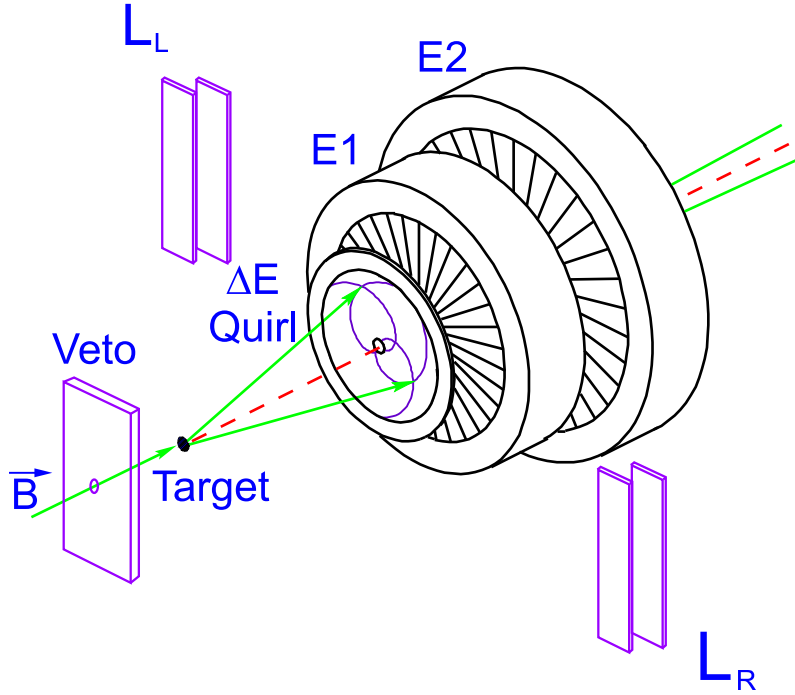


Figure 4.4: A schematic view of the Germanium Wall detectors and the axillary detectors: L_R , L_L , $Veto$. Sizes of different elements are not scale.

schematic view of the experimental arrangement is presented in Figs. 4.3 and 4.4. Each detector possessed a central hole, to allow the beam particles which did not interact with the target to be dumped via an exit in the side yoke of the first dipole of the magnetic spectrometer. Dimensions of the holes, the total diameters of the detectors and the distances from the target define the angular acceptance of the detection system, which was $3^\circ - 14^\circ$ for the polar and 2π for the azimuthal angles.

The GeWall components were diodes of $p-i-n$ type with the dimensions of the detectors and distances to the target shown in Table 4.1. Two different types of detectors were used: a thin transmission detector “Quirl” with an excellent spatial resolution, and two thick energy detectors “Pizza 1” (E1) and “Pizza 2” (E2) with excellent energy resolutions. The detectors were operated in vacuum, at the liquid nitrogen temperature. The Quirl detector was used to determine the position and the energy loss (ΔE -detector) of the passing particles. It was segmented on the front and the rear sides to 2×200 grooves, shaped as Archimedes spirals, each covering an angular range of 2π (including the central hole region). The bending direction of the spirals on the front and rear sides are opposite to each other. Thus, the overlaps of the spirals form an array of about 20000 pixels (central hole removes approximately half of the potential crossing regions) of the size from 0.011

| detector | diameter of the hole frontside | diameter of the hole rearside | total diameter | distance to the target | thickness |
|----------|--------------------------------|-------------------------------|----------------|------------------------|-----------|
| Quirl | 5.0 mm | 5.0 mm | 36.0 mm | 76 mm | 1.8 mm |
| E1 | 5.4 mm | 6.4 mm | 53 mm | 88.0 mm | 15.0 mm |
| E2 | 7.5 mm | 8.4 mm | 77 mm | 117.0 mm | 14.4 mm |

Table 4.1: Characteristics of the GeWall detectors.

mm^2 (the most inner) to about $0.1 mm^2$. Features of the Quirl detector are presented in Figs. 4.5 and 4.6. The energy detectors E1 and E2 were divided into 32 segments each and mainly used for measuring energies of the charged reaction products. Furthermore, they provided additional azimuthal information. A scheme of the Pizza detector is shown in Fig. 4.7.

Information on energy losses in different GeWall components can be used for particle identification, whereas the sum of these energies gives the total kinetic energy of the particle. Position information from the Quirl detector enables the determination of all three components of the momentum vector of the particle (assuming a point-like interaction region at the target) - distance from the target and the position on Quirl transform directly to the azimuthal angle ϕ and the polar angle θ , see Sec. 5.3.

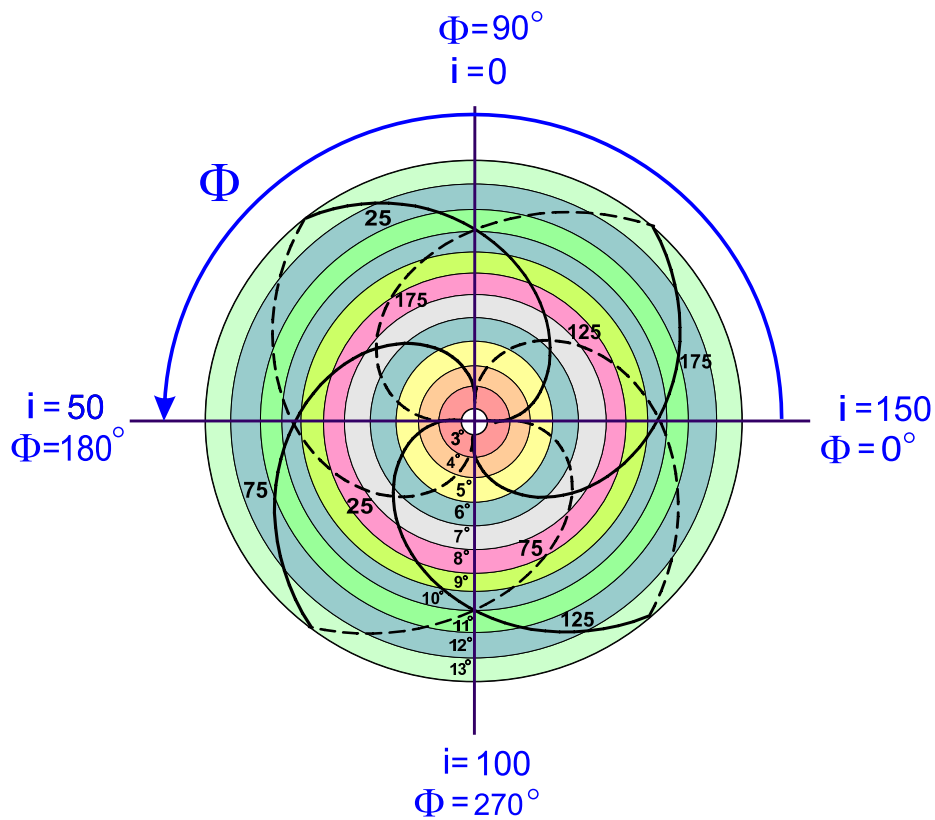


Figure 4.5: A schematic drawing of the Quirl detector with a few spirals of the front and rear sides marked with their numbers. Areas marked with different colours refer to different polar angle ranges.

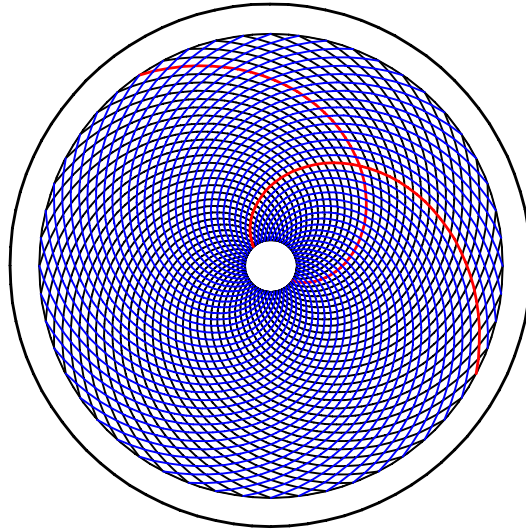


Figure 4.6: A schematic view of the Quirl detector. For clearness only 50 spirals of the front and rear sides are drawn.

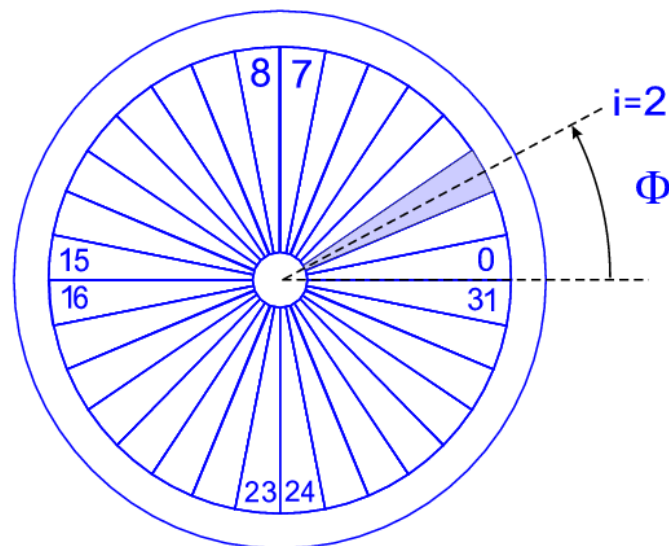


Figure 4.7: A schematic picture of the pizza energy detector with its division into 32 wedges.

4.3.5 Electronics

A schematic view of the electronic devices serving the GeWall detectors is presented in Fig. 4.8. The signals generated by the detector elements i.e. spirals of Quirl or segments of Pizzas were processed in a few steps. First a charge sensitive preamplifiers (CSPA) were used to transform the current pulses, produced in the detector by particles, into voltage signals. These output signals were split into energy and timing branches. The first one contained the shaper amplifier modules coupled to ADCs (Silena 3314 for the Pizza detectors and Le Croy 4300B for the Quirl detector, always preceded by a module Le Croy 3309 PTQ-Peak to Charge Converter), which finally gave the digital information on the energy deposited in the detector elements. The second branch of the circuit was used to generate logical signals for multiplicity analysis and triggering system. In the case of Pizza detectors this branch was equipped with fast filter amplifiers FTA, discriminators and TDC (Time to Digital Converter) modules. Discriminator modules output signals were led to the trigger logic. For the Quirl detector branch, discriminators and MALU units were applied. The MALU (Multiplicity Arithmetic Logic Unit) modules were used in order to combine the neighbouring hits on the Quirl detector to a cluster and to count the number of clusters produced in each event. Output signals obtained from the units are proportional to the cluster multiplicity. MALU output signals were led to the trigger logic.

The trigger conditions were chosen to be:

$$T1 \equiv Quirl\ Front(1)\ AND\ Quirl\ Rear(1)\ AND\ E1(1)\ AND\ \overline{VETO},$$

$$T2 \equiv (Quirl\ Front(2)\ OR\ Quirl\ Rear(2))\ AND\ E1(1)\ AND\ \overline{VETO},$$

$$Quirl\ Front(1) \equiv Quirl\ Front \geq 1\ (\text{a minimum bias trigger}),$$

$$Quirl\ Rear(1) \equiv Quirl\ Rear \geq 1,$$

$$Quirl\ Front(2) \equiv Quirl\ Front \geq 2,$$

$$Quirl\ Rear(2) \equiv Quirl\ Rear \geq 2,$$

$$E1(1) \equiv Pizza\ 1 \geq 1.$$

where the inequalities are understood as concerning the detected in a given element cluster multiplicity. In the experiment the triggers T1 and T2 were individually downscaled by factor 2^x ($x=0$ for T1 and $x=2$ for T2) to enhance the coincidence rate with respect to singles. The digitized data obtained from ADC and TDC units were stored in memories and then readout by the Data Acquisition system (DAQ). All crates were controlled by a PC via CAMAC/FERA Crate Controller and had one dedicated Trigger Module, which informed given Crate Controller when to start the read-out procedure. The numbers of accepted and rejected events were recorded by the Scaler Module (once per spill) to obtain information of the system dead time. Finally the data were proceeded to Subevent and Event Builder Modules, sent to a master PC called Event Manager and written to computer discs in so-called cluster form (this form could be converted to the event format by the *CLUSTER2EVENT* program during the analysis process). Moreover a sample of the data was sent to the online analysis performed on a dedicated computer.

All the controlling computers together with the Crate Controllers, Subevent and Event Builders were connected via fast Experimental Network allowing their communication via TCP/IP protocol and were synchronized by means of PCI synchronization modules.

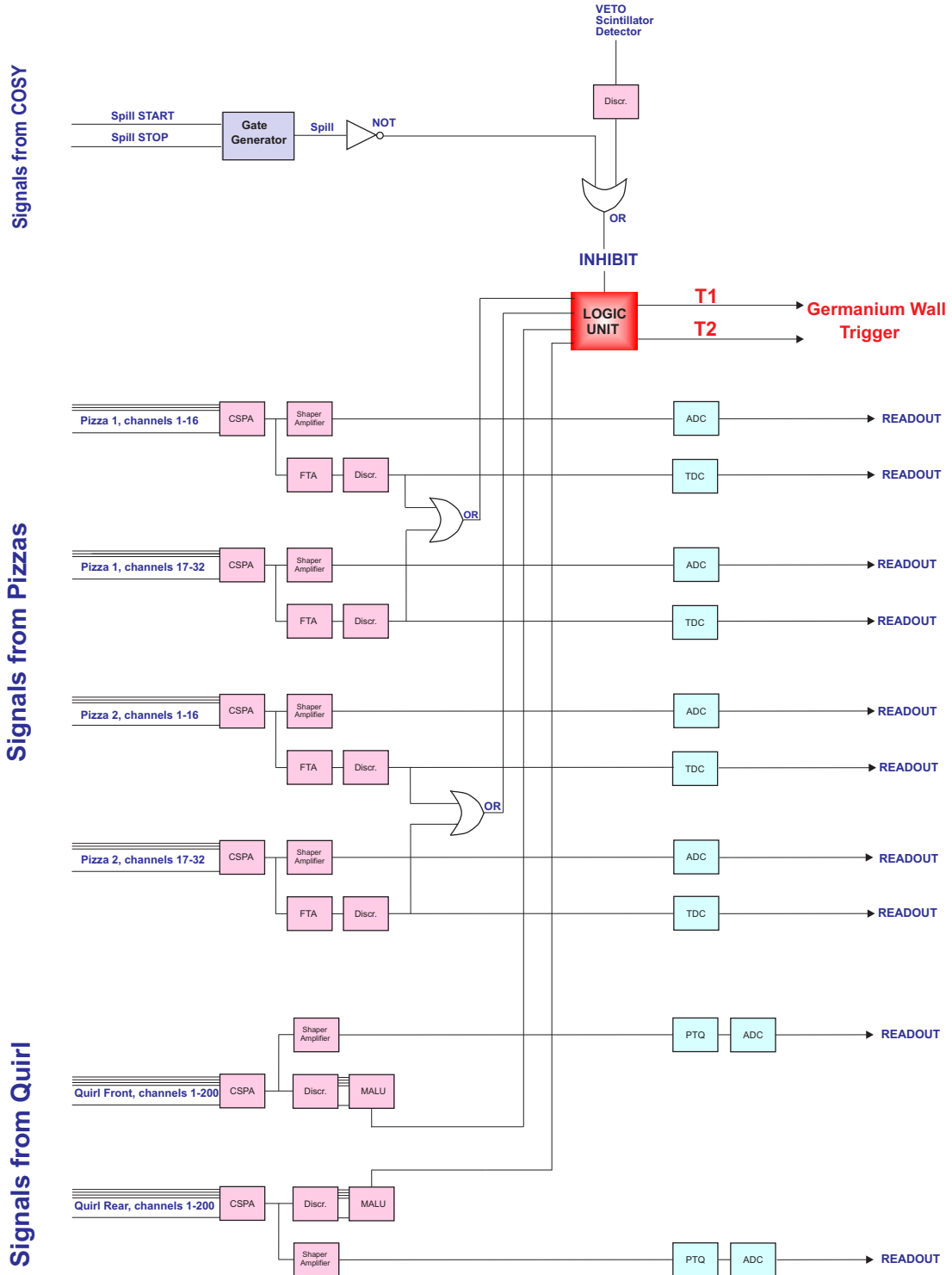


Figure 4.8: A schematic diagram of the GeWall electronics.

Chapter 5

Data analysis

This Chapter contains description of all procedures which were used in evaluation of observables interesting for the breakup process: cross sections and analyzing powers, at chosen kinematical configurations of the two outgoing protons. Moreover, experimental uncertainties and their sources are discussed along with the methods of their estimations.

5.1 Basics of software analysis

During the experiments data were accumulated in a *cluster* format written by DAQ and then converted to an *event* format using a CLUSTER2EVENT program (see also Chapter 4.3, Section 4.3.5). The next step was application of a C++ program called SORTER which transforms the data streams to *ASCII* format, which were finally stored in ROOT files with the use of Tree structure.

The sorting program is based on three main libraries: XD-package [68], the Gemlib library, providing matching to the GEM Data Acquisition System [69] and the GWall library, containing the track reconstruction routines for the Germanium Wall detector [69]. In general, SORTER is divided into two separate programs: a raw sorter (*gSort - raw - work*) and a physical sorter (*gSort*). The raw sorter is able to create output data without any calibration and provides ADC or TDC information only in channel units. This sorter version is used for preparation of the actual calibration and controlling the detector performance. The physical sorter provides energy information after applying calibration procedure and also reconstructs particle trajectories with the use of track reconstruction package.

The output of physical sorter contains the full set of kinematical variables for a given particle, like the energy deposition in each detector, polar and azimuthal angles, *etc.*. This information is used in the next steps of analysis and allows to identify particles (breakup protons, elastic deuterons and protons) by $\Delta E - E$ technique and to create different cuts for removing background events.

5.2 Reconstruction of the particles trajectories

Detailed description of particles trajectories reconstruction routine is presented in [70], here only a brief summary is included for clarification of the software steps which are necessary to understand further material of this Chapter.

Each event is characterized by a number of clusters on every detector i.e. on Quirl Front

(QF), Quirl Rear (QR), Pizza 1 (E1) and Pizza 2 (E2). The cluster consists of a group of spirals (or sectors) or of a single spiral (a sector) which registered charge signal in a given event. Thus the neighbouring channels are considered to belong to a cluster if their energy (ADC channel) is above a certain threshold, value of which is defined for each individual channel. Therefore, the energy deposited in each detector is a sum of all energies deposited in elements constituting the cluster. Besides energy, clusters are also characterized by a mean azimuthal scattering angle $\bar{\Phi}$, calculated as the weighted average of the angles of the cluster elements, e.g. :

$$E = E_1 + E_2 + \dots + E_n, \quad (5.1)$$

$$\bar{\Phi} = \frac{\phi_1 \cdot E_1 + \phi_2 \cdot E_2 + \dots + \phi_n \cdot E_n}{E_1 + E_2 + \dots + E_n}, \quad (5.2)$$

where $i=1, 2, \dots, n$ enumerates the elements of the cluster, E_i is the energy deposited in each element and ϕ_i is the geometrical azimuthal position of the i -th element (see also next Section).

Having these parameters calculated for both sides of the Quirl detector, one can identify the possible crossing points between the front and rear clusters. This information is used in track generation procedure. All found Quirl crossing points are combined with the E1 and/or E2 clusters. Also unusual combinations like QF/QR and E2 are possible. A schematic of the track reconstruction is presented in Fig. 5.1. For selecting the tracks which are likely to represent real particles, additional conditions are also necessary, like a proper correspondence between values of ΔE and E1 or ΔE and E1 and E2, which are

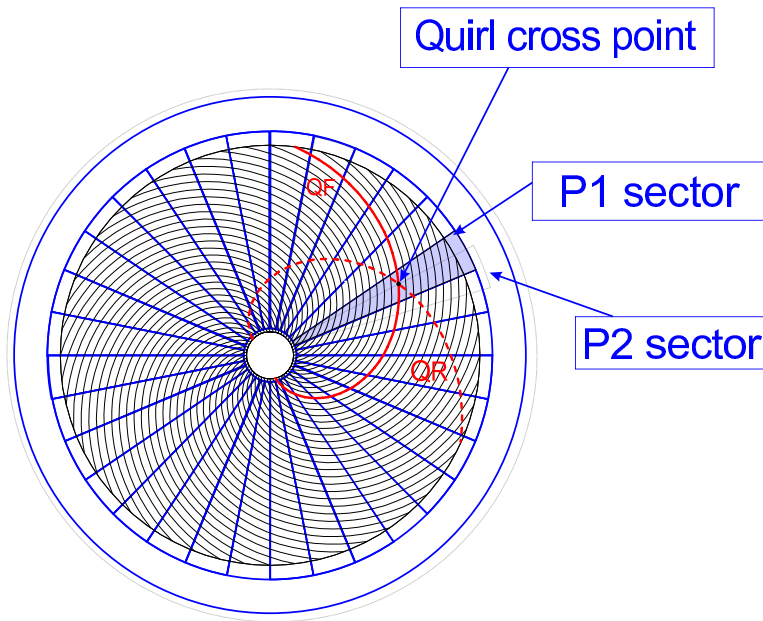


Figure 5.1: A sample event, in which a crossing point in the Quirl detector was found and the adequate sectors of E1 and E2 detectors were matched.

reflecting the particle ranges. There is also an upper limit imposed on the difference between the azimuthal angles of the crossing point in Quirl and the E1 cluster and analogously for E1 and E2 clusters.

Before a track was fully reconstructed, additional conditions, which defined class of events accepted in the further analysis were imposed. In the case of single-track events (elastic protons or deuterons) only events with one cluster created on each detector were accepted, whereas for coincident events (two-track breakup events) two clusters on at least two detectors (Quirl and Pizza 1) were chosen for the next step of analysis. This selection assured an efficient reduction of accidental events.

Depending on the kinetic energy of a particle, three kinds of tracks can be specified: short one (only Quirl detector responds), medium one (Quirl and Pizza 1 respond) and long one (Quirl, Pizza 1 and Pizza 2 respond). For coincident events, combinations of the above kinds are considered.

5.3 Angular information

Precise knowledge of particle emission angles is crucial for reconstruction of the breakup and elastic kinematics. For calculation of polar θ and azimuthal ϕ angles the Quirl detector, which provides excellent spatial resolution, was used. Active area of Quirl is divided on both sides into 200 Archimedes spirals, as it was presented in Sec. 4.3.4. Every spiral covers an angular range of 180° and the position of the i^{th} spiral is described with $\varphi_i = \frac{2\pi i}{200}$, what defines its angular displacement from the 0^{th} spiral center. For any crossing point (x, y) between a left- (rear) and a right-bent (front) spiral, the angle φ and the radius r in polar coordinates on the Quirl surface are given as follows:

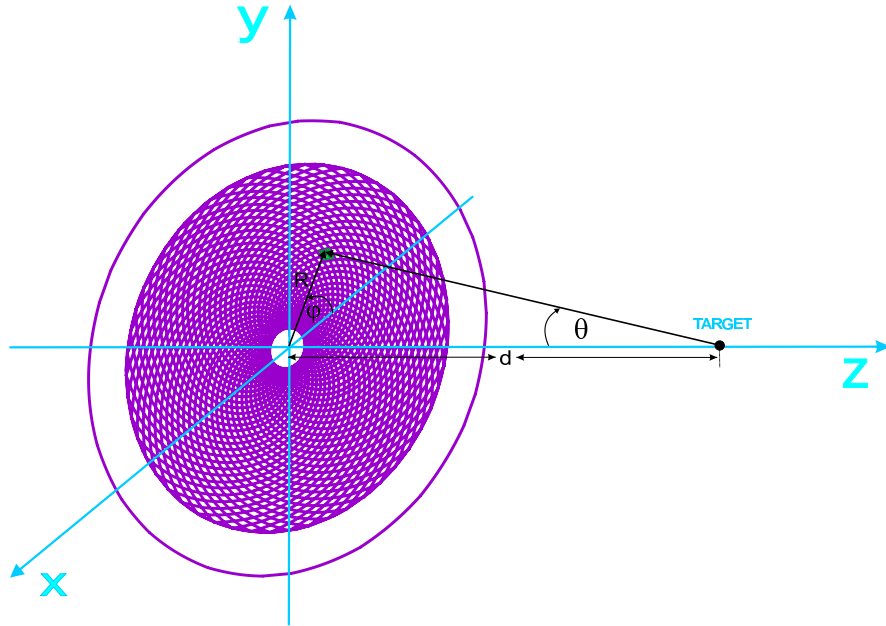


Figure 5.2: Variables, which are used in reconstruction of the emission angles of particles from the target point.

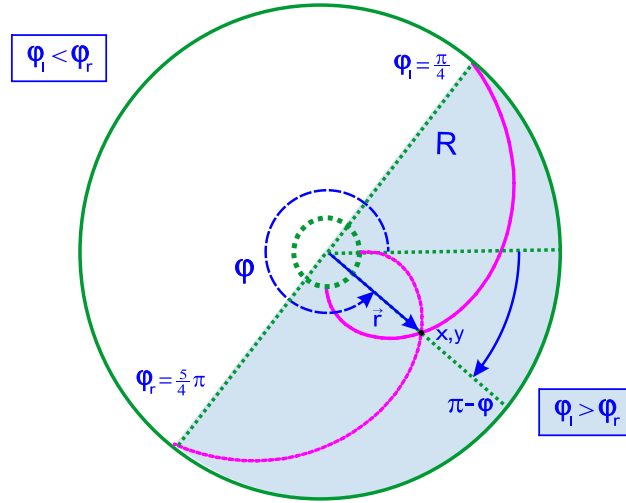


Figure 5.3: Parameters of a crossing point of the front and rear spirals.

for $\varphi_l < \varphi_r$:

$$\varphi = \frac{1}{2}(\varphi_l + \varphi_r) + \pi \quad (5.3)$$

$$r = R \frac{1}{2\pi}(\varphi_l - \varphi_r) \quad (5.4)$$

for $\varphi_l \geq \varphi_r$:

$$\varphi = \frac{1}{2}(\varphi_l + \varphi_r) \quad (5.5)$$

$$r = R \left(1 - \frac{1}{2\pi}(\varphi_l - \varphi_r)\right) \quad (5.6)$$

where φ_l and φ_r are defined in Fig. 5.3. To obtain reliable values of the reconstructed angles, the geometry of the detection system and the reconstruction procedure must be well known and checked. Thus, to calculate the θ angle, the distance d between the target point and the Quirl detector (see Fig. 5.2) was measured. To verify the measured (by optical instruments in vacuum) value, the elastic scattering events were used. First, based on the theoretical elastic scattering kinematics, the deuteron and proton energy losses in the GeWall detectors were calculated with the use of SRIM program. As the result, a theoretical $\Delta E - E$ dependencies for different θ angles were produced (examples are presented in Fig. 5.4). Secondly, different Quirl-target distances were used for the experimental energy losses reconstruction and confronted with the theoretical calculations. As a consequence the distance between the Quirl detector and the target was found as $d = 76$ mm, in good agreement with the result of the optical measurement.

5.4 Identification of the reaction channels

Particle identification was based on the $\Delta E - E$ technique. For that purpose energy-energy spectra were constructed, using different combinations of the detectors to provide the energy information. The events of interest are the coincidences of the two protons from the breakup reaction, and the elastic channel, which, depending on the range of polar

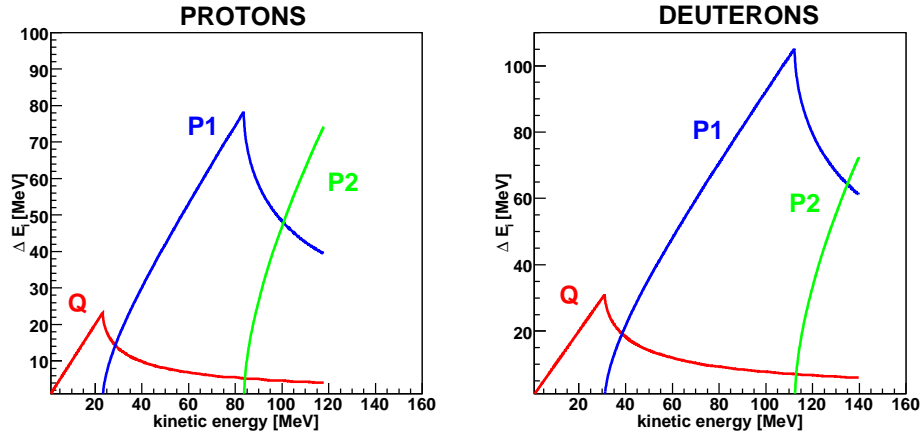


Figure 5.4: The energy lost in different GeWall components (Q- Quirl 1.8 mm thick, P1 - Pizza 1 15 mm thick and P2 - Pizza 2 14.4 mm thick) as a function of the kinetic energy of the measured particles: protons and deuterons.

angles, can be identified as single-track events or deuteron-proton coincidences (two-track events). In Fig. 5.5 three different identification spectra outside the angular range of the beam-like background ($\theta > 7^\circ$) are presented. Three groups of particles are clearly seen and separated: the long branch of the breakup protons, the spot of the elastic protons and, above the proton loci, the spot of the elastic deuterons together with the rest-overs of the deuteron beam.

In spite of the fact that the beam was focused to a spot with the size described by $\sigma \approx 1.0$ mm, the tails of the direct beam were still visible on the detector, especially for very small polar angles $\theta < 7^\circ$. These events are mainly responsible for accidental coincidences and can be eliminated by kinematical conditions.

To identify the breakup process, two-track events with at least Quirl and Pizza 1 detectors responding in each track were selected (two, at least medium, tracks), see also Sec. 5.2. The result of particle identification in that case is illustrated in Fig. 5.6.

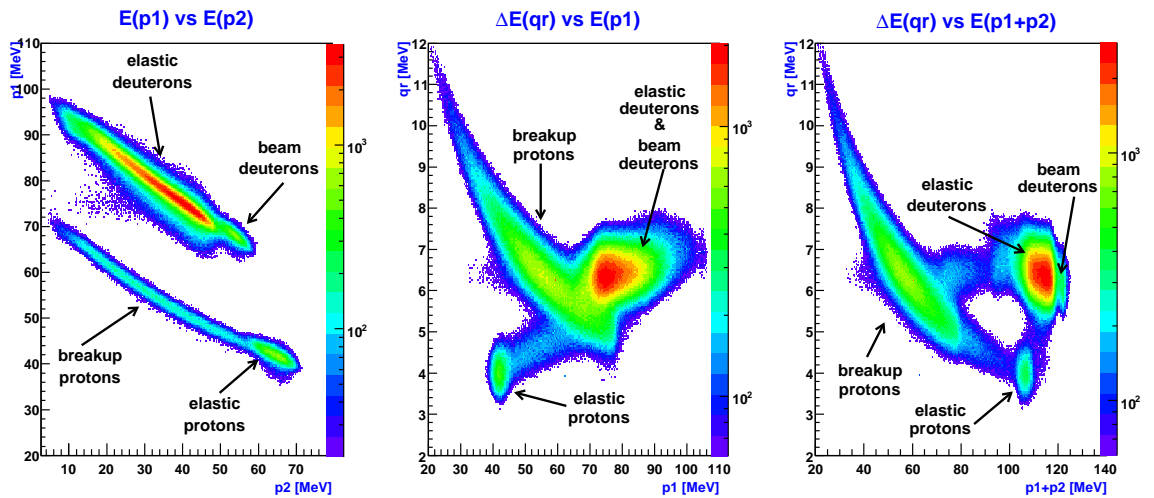


Figure 5.5: Examples of $\Delta E - E$ particle identification spectra for detector angular range of $\theta > 7^\circ$ and for single-track events.

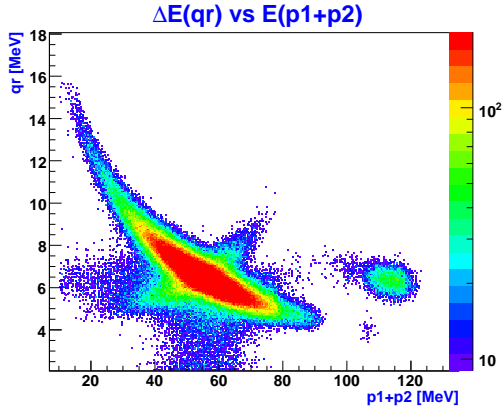


Figure 5.6: Identification spectrum for the two-track protons constructed with assumptions specified in the text.

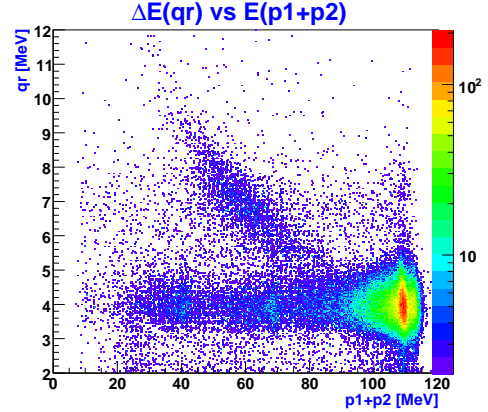


Figure 5.7: Protons identification spectrum for the events registered as the short-long tracks. All assumption are described in the text.

In the picture the long, “banana“ branch of protons comes from the breakup reaction and there are almost no elastic particles visible.

Another process of interest is the elastic d-p scattering which, as it was mentioned before, can be registered as single-track or two-track events. For high-energy protons with $\theta_{prot} < 7^\circ$, the coincident low-energy deuterons are stopped in the Quirl detector. These events belong to the second branch of the elastic kinematics (see Sec. 2.2) and together with the coplanarity condition $\varphi_{pd} = |\varphi_{prot} - \varphi_{deut}| = 180^\circ$, can be very well identified on the ΔE_{Quirl} versus $E_{Pizza1+Pizza2}$ spectrum. The events were selected as short - long tracks. In Fig. 5.7 such events of interest can be seen.

The dependency ΔE_{Quirl} versus $E_{Pizza1+Pizza2}$ is also useful for selection of the single-track events. The events with single protons are characteristic for the range $\theta_{prot} > 7^\circ$, whereas the elastic high-energy deuterons are single-track events over the whole detector acceptance (the coincident low-energy protons are emitted outside the detector acceptance). Examples of the identification spectra for single-track events are shown in Fig. 5.5.

5.5 Testing the detection system geometry

To test symmetry of the GeWall detectors, the elastic scattering particles were selected as single-track and two-track events (see previous section).

With the use of elastic deuterons, an important parameter, the relative azimuthal angle ϕ_0 between Pizza 1 and Pizza 2, which affects the procedure of matching E1 and E2 clusters in the track reconstruction routine, was established. Geometry, of the sectors of E1 or E2 can be observed on the Quirl XY - plane, for events selected with the condition of only one E1 (E2) sector responding in an event, see Fig. 5.8. Calculation of the centers of the images of the E1 and E2 sectors in terms of azimuthal angles Φ_i characterizing a given sector i , lead to the experimental dependencies between Φ_i and the *number of the sector* for both detectors. Confronting this findings with the theoretical relations, the ϕ_0 was found to be -6.7° . The two-track events (from the second branch of kinematics - see Sec. 2.2), refer

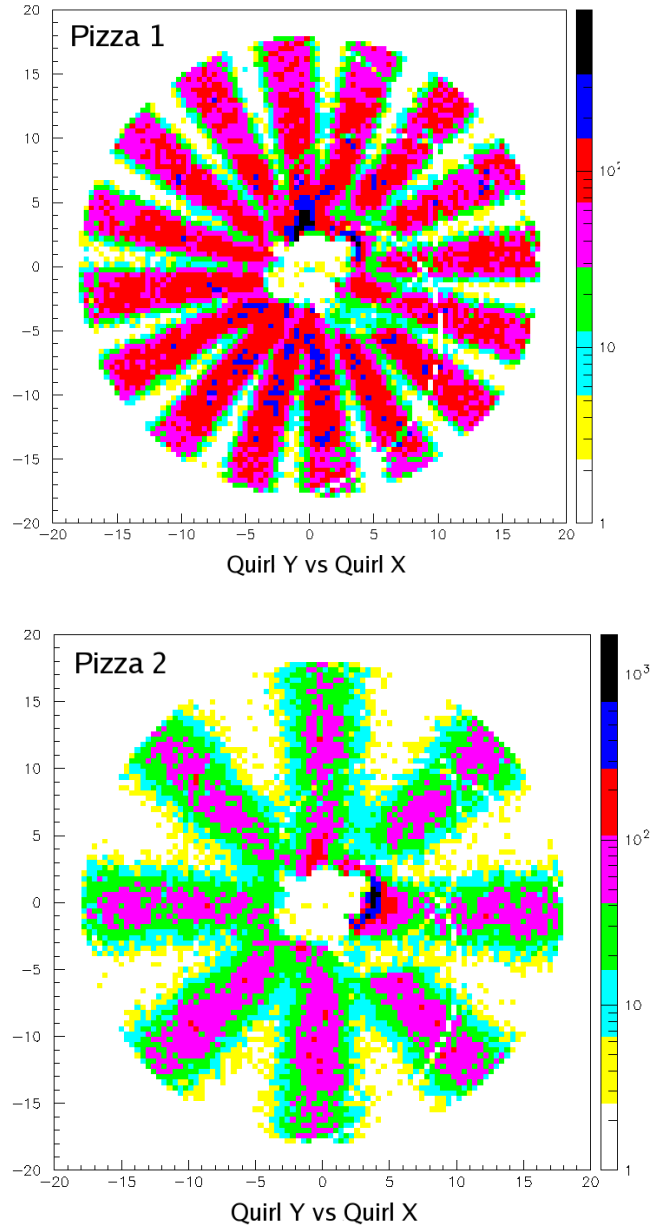


Figure 5.8: Response of the Quirl detector in the case of only one sector of Pizza 1 (upper panel) and Pizza 2 (lower panel) active in an event. For clearness only 16 sectors of the E1 detector and 8 sectors of the E2 detector are presented. Visible are also a few not working spirals.

to a high-energy proton accompanied by a low-energy deuteron. For proton polar angles $\theta_p \leq 7^\circ$ both particles reach the detector, with the deuteron being stopped in Quirl. Fig. 5.9 illustrates the distribution of the relative azimuthal angle $\varphi_{pd} = |\varphi_{prot} - \varphi_{deut}|$. The events are grouped around $\varphi_{pd} = 180^\circ$ in a prominent peak with only a low background of accidental coincidences. This global dependency can be inspected in more details in Fig. 5.10, where the relation φ_{prot} vs. φ_{deut} is shown for several θ_p angles. The events populate only the areas with $\varphi_{pd} = 180^\circ$, what demonstrates proper reconstruction of the azimuthal angles over the whole range and reflects detector symmetry.

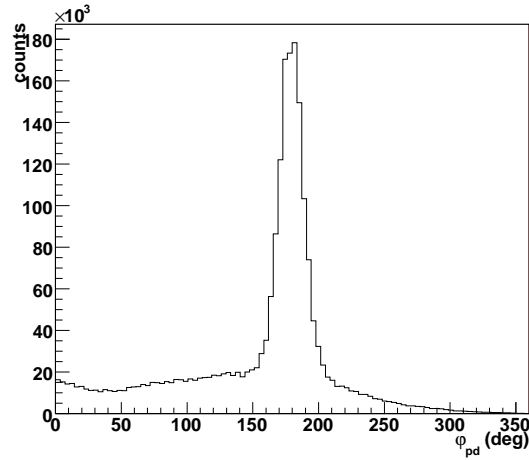


Figure 5.9: Number of counts as a function of φ_{pd} for the identified proton-deuteron coincidences.

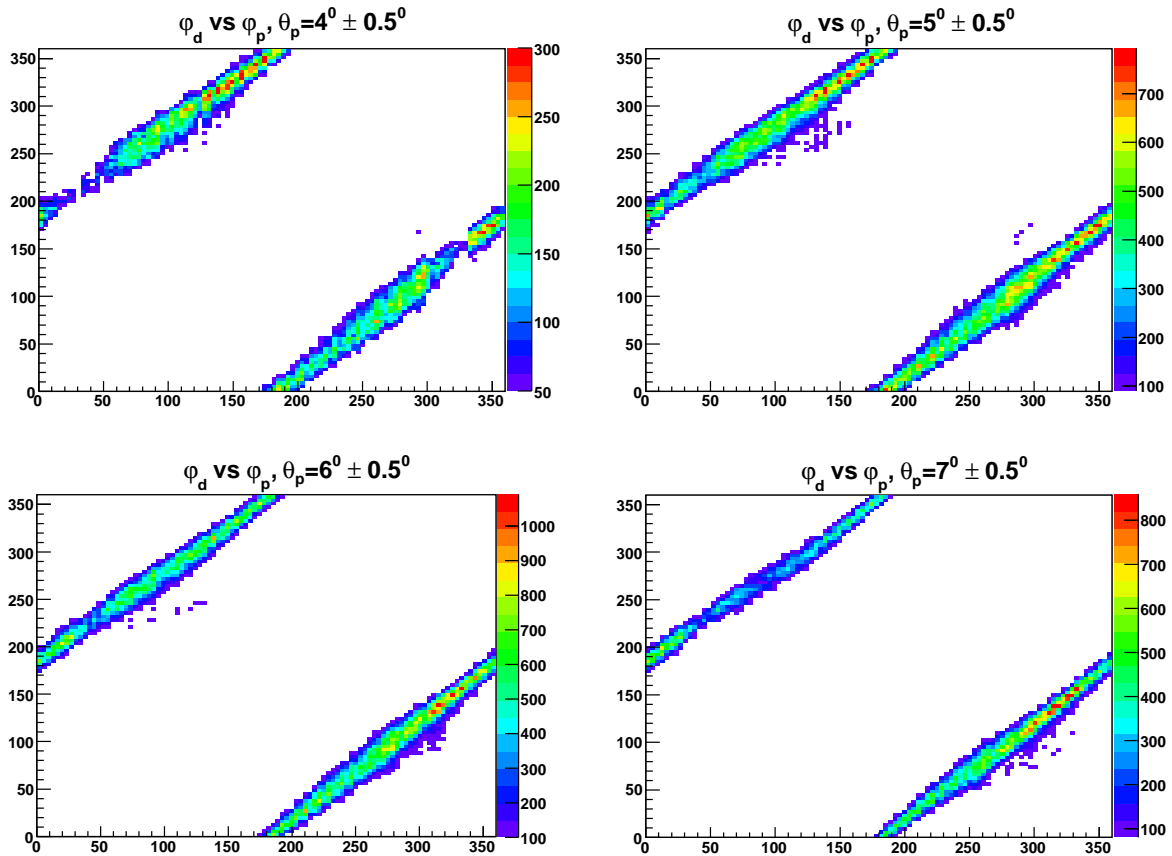


Figure 5.10: Azimuthal angle dependencies (φ_d vs. φ_p) of two coincident particles, one of which is identified as a proton emitted at different θ_p angles. The populated loci for the relative angle of $\varphi_{pd} = 180^\circ$ are due to the elastic scattering coincidences.

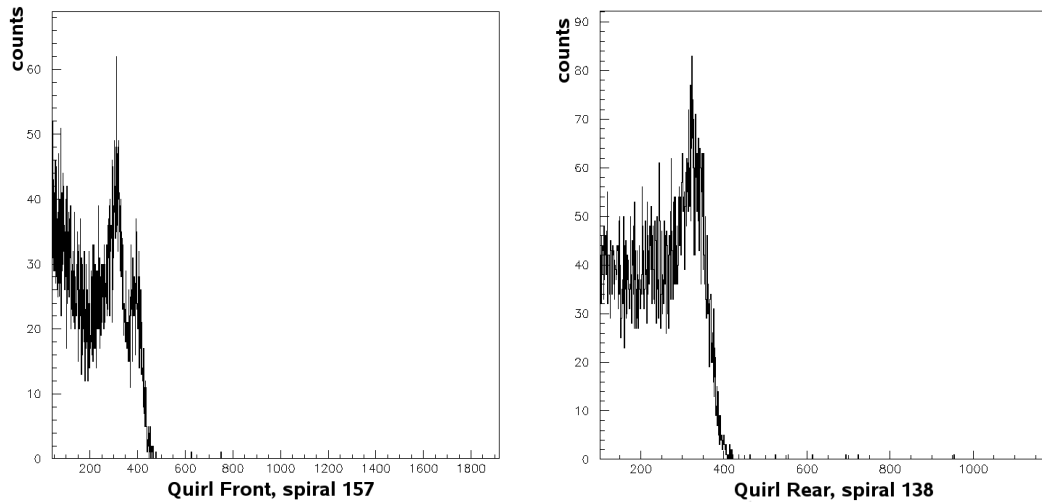


Figure 5.11: Response of single spirals for Quirl Front and Quirl Rear detectors to the direct beam. Malfunctioning of front side is visible in double peak structure.

5.6 Energy calibration

Calibration of the GeWall setup is a standard procedure of finding the relation between the *deposited energy* and the *ADC channel* for each individual detector element, i.e. spiral or segment. For this purpose 130 MeV deuteron direct beam with strongly reduced intensity was used. Germanium Wall was lit up with an about one millimeter beam spot, moved over the detector to obtain ADC spectra from all its elements. Typical ADC spectra coming from a calibration run for Quirl Front, Quirl Rear and Pizzas are presented in Fig. 5.11 and 5.12. The tails on the left side of the peaks correspond to particles hitting neighbouring elements, what caused that the charge produced in the detector material was distributed over more than just one element. Obviously, the main peak represents situations when the full particle energy is deposited in the spiral (sector) of interest.

As it turned out during the experiment the front side of the Quirl detector had been slightly damaged, so for the further energy analysis only the rear side was used. Because of the fact that the energy deposited by 128 MeV deuterons (about 2 MeV of the 130 MeV deuteron beam is lost in the 2 mm thick Veto counter) in each GeWall component is known from the theoretical calculations, calibration coefficients for all spirals and sectors can be easily determined and used in the further analysis. For Pizza 1 and Pizza 2 detectors the theoretical energy losses are 70.4 MeV and 51.1 MeV respectively, whereas for Quirl detector it is 6.3 MeV. For Quirl detector the energy reconstructed for the direct deuteron beam has a mean value of 6.7 MeV, therefore it deviates by about 6% from the theoretical value. For Pizza 1 the reconstructed energy was 69.8 MeV, while for Pizza 2 it was 51.0 MeV, the differences being below 1%.

Elastic scattering deuterons and protons were selected for further tests. This events are an ideal tool for studying energy reconstruction correctness, because of the fact that deuteron and proton energy loss in GeWall detectors can be easily calculated, see Sec. 5.3 for details. For each sector of Pizza 1 and Pizza 2 the experimental relation between the deposited energy and the polar angles of the particles was plotted and compared with

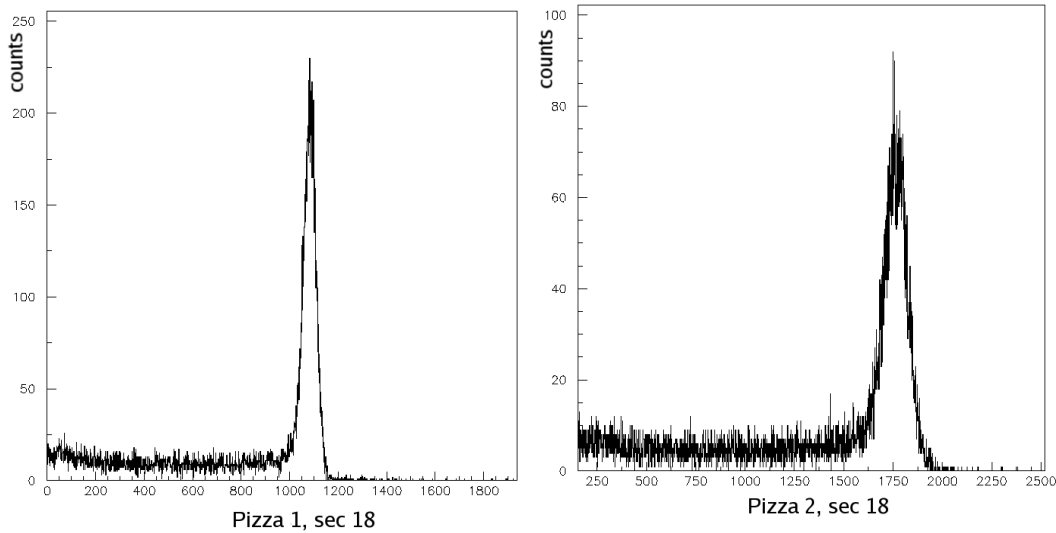


Figure 5.12: Response of single sectors of Pizza 1 and Pizza 2 detectors to the direct deuteron beam.

the theoretical one. As the result, correction coefficients for each individual sector were obtained and applied to the calibration procedure. In Fig. 5.13 the lower panel illustrates the situation when the experimental elastic kinematic reproduces the theoretical calculations, what corresponds to the adequate correction coefficient for this sector.

Final test of the calibration exactness was checking how the reconstructed energy reproduces the breakup kinematics. For this purpose the E_1 - E_2 coincidence spectra for several configurations of the two protons were created without calibration correction. In all situations experimental points lay above the theoretical curve (see Fig. 5.14, left panel). Applying the correction factors (for Pizza detector as above, and correcting also the Quirl energy response) leads to a perfect agreement between the experimental and theoretical kinematics (Fig. 5.14, right panel).

5.7 Energy resolution of GeWall detectors

In order to deduce the energy resolution of the GeWall detectors, the 130 MeV deuteron beam with strongly reduced intensity was used. One has to realize that the resolution is influenced by charge splitting effect, which causes division of the charge carriers produced by a particle in the detector material on more than one neighbouring spiral or sector. As it was mentioned before, the energy of such events is reconstructed by building a cluster from the responding channels and making the sum of all registered energies. Obviously the energy resolution is deteriorated with the increase of the cluster size.

Due to the fact that the front part of the Quirl detector was biased with poor resolution and only Quirl Rear was in fact used, the rear side defines an actual ΔE resolution. Table 5.7 contains information on the determined energy resolution for each GeWall detector. Second column presents energy resolutions $\Delta E/E$ from the individual ADC spectra (see also Figs. 5.15 and 5.16, left panels). Third column presents the energy resolution for the

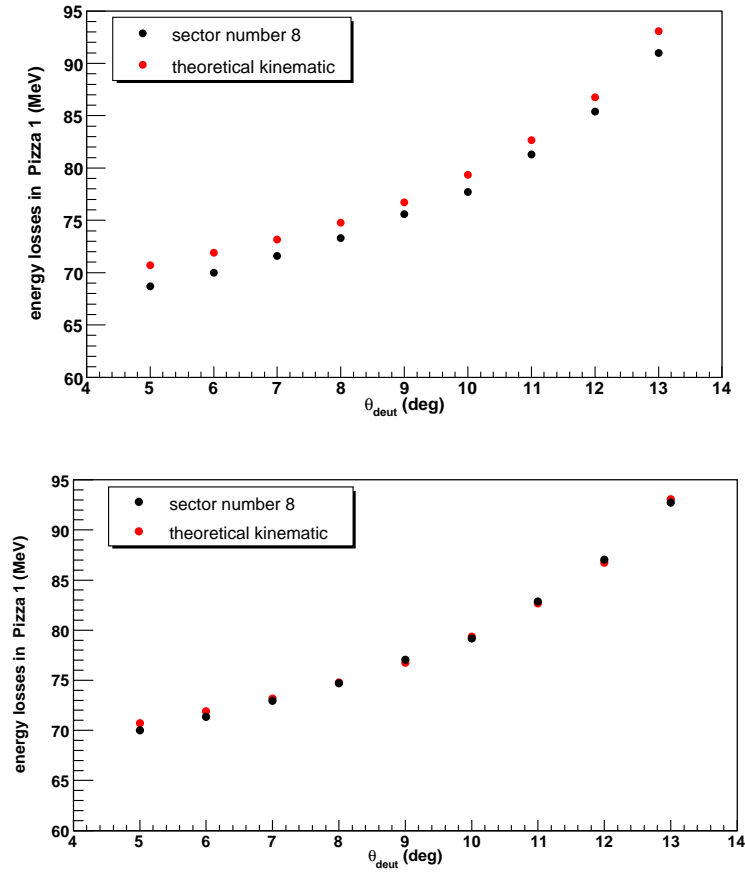


Figure 5.13: Theoretical elastic scattering kinematics compared with the experimental points for a single sector of Pizza 1 detector, before (upper panel) and after (lower panel) applying the calibration correction.

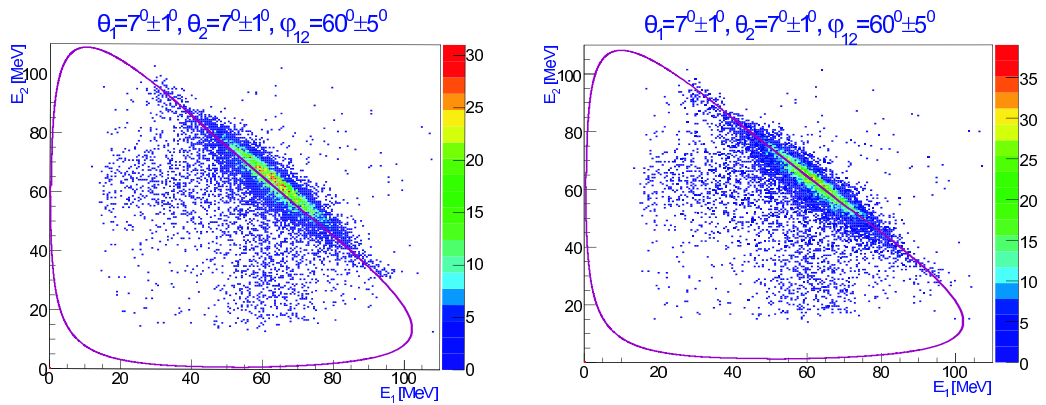


Figure 5.14: E_2 vs. E_1 coincidence spectra for two registered protons in the angular ranges specified in the pictures. The violet lines represents kinematical curve calculated for the central values of the chosen angular ranges. Difference between the initial (left panel) and final (right panel) calibration is visible.

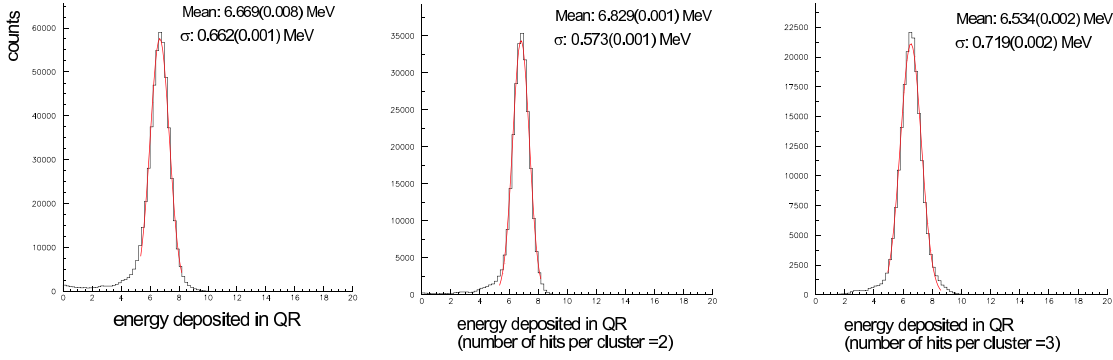


Figure 5.15: Reconstructed energy of the deuteron beam at the Quirl rear detector side (left panel), and for additional conditions: two spirals register the full energy (middle panel), three spirals register the full energy (right panel). Lines show the Gaussians fitted to the peaks - parameters displayed in the panels.

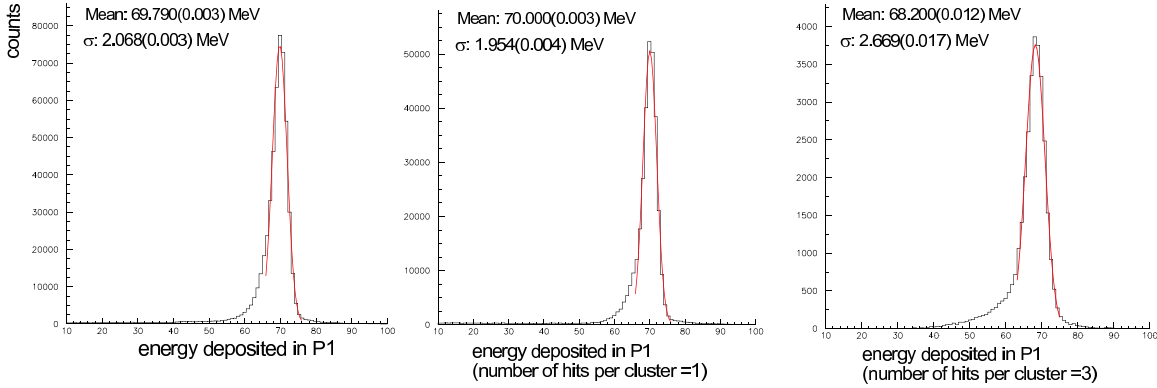


Figure 5.16: Reconstructed energy of the deuteron beam at the Pizza 1 detector (left panel), and for additional conditions: two sectors register the full energy (middle panel), three sectors register the full energy (right panel). Lines show the Gaussians fitted to the peaks - parameters displayed in the panels.

| detector | $\Delta E/E$ for individual ADC spectrum [%] | $\Delta E/E$ for all spirals/sectors [%] | $\Delta E/E$ for one or two spirals/sectors [%] | $\Delta E/E$ for three spirals/sectors [%] |
|----------|-------------------------------------------------------|---------------------------------------------------|----------------------------------------------------------|-----------------------------------------------------|
| Quirl | 14 | 20 | 17 | 22 |
| Pizza 1 | 5.6 | 5.9 | 5.5 | 7.8 |
| Pizza 2 | 7.2 | 7.7 | 7.8 | 8.4 |

Table 5.1: Experimentally determined energy resolutions of the GeWall detectors.

sum of the energies of all spirals or sectors after applying energy reconstruction and clustering procedures (see also Figs. 5.15 and 5.16, middle panels). Fourth column contains $\Delta E/E$ in the case of one or two spirals or sectors registering the full energy, whereas the fifth one is the case of three spirals or sectors registering the full energy (see also Figs. 5.15 and 5.16, right panels).

As one can notice the effect of charge splitting (clustering procedure) causes a broadening of the reconstructed energy distribution for particles with given energy (130 MeV deuteron

beam) for Quirl and Pizzas detectors. Another important contribution deteriorating the energy resolution is the radiation damage, which was not investigated in this experiment.

5.8 Determination of the beam polarization

Knowledge of the beam polarization value is necessary for studies of polarization observables of the elastic scattering and breakup processes. In order to determine the beam polarization three kinds of the elastic scattering events were used: single high-energy deuterons (protons emitted outside the detector acceptance) or protons (accompanied by the low-energy deuterons stopped in Quirl and not identified), as well as the $d - p$ coincidences. These three groups of particles were identified, selected and prepared for further study by applying a background subtraction procedure.

Despite the fact that 130 MeV deuteron beam has been produced in a few polarization states, only pure vector polarized state $(P_z, P_{zz}) = (-\frac{2}{3}, 0)$ and unpolarized one $(P_z, P_{zz}) = (0, 0)$ were acquired in the statistically sufficient periods. Unfortunately, the tensor polarized states have been found to be characterized by very low level of polarization, precluding extraction of the corresponding observables. Consequently, the following analysis is limited to the two states mentioned above.

5.8.1 Selection of the elastic scattering events

The elastic scattering events were identified using $\Delta E - E$ technique, described in details in Sec. 5.4. Moreover, further energy cuts were defined and imposed to clearly isolate the events of interest. First, a curve separating the proton loci from the deuteron one was carefully defined. These two groups of events were projected onto $E_{P1} + E_{P2}$ energy axis. Fig. 5.17 shows examples of such projections for deuterons and protons in selected angular ranges. As one can notice, the deuteron spectrum contains two kinds of events: the elastic deuterons localized in a prominent peak and rest-overs of the deuteron beam. In the proton branch projection spectrum, the elastic protons and the breakup continuum events are present.

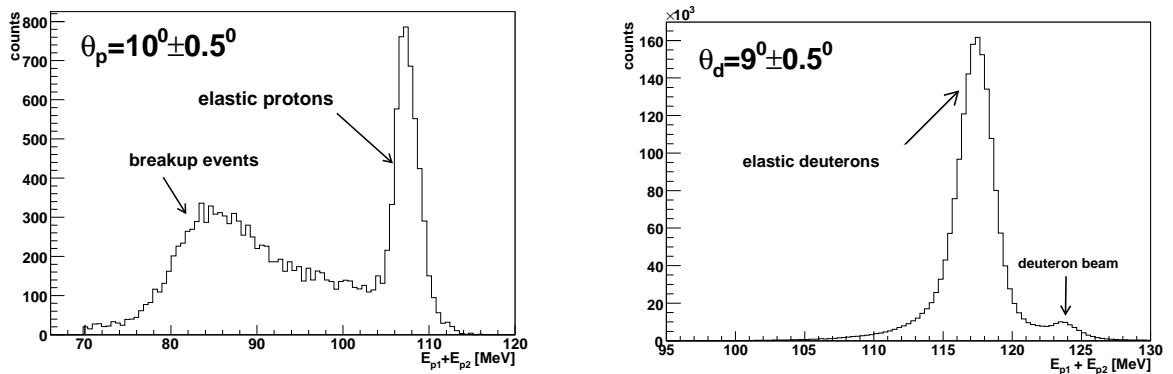


Figure 5.17: Projections of the elastically scattered protons (left panel) and deuterons (right panel) onto $\Delta Pizza1 + \Delta Pizza2$ ($E_{P1} + E_{P2}$) energy axis, for chosen polar angles θ . Origins of the spectra components are marked in the panels.

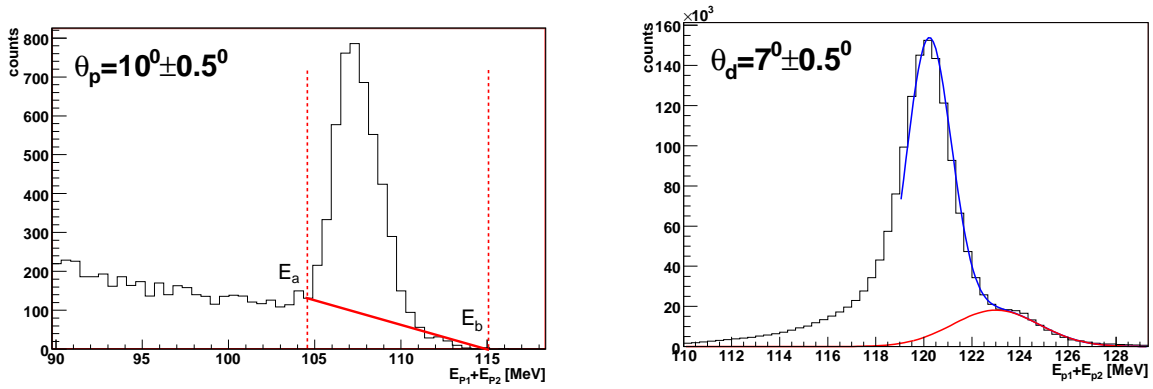


Figure 5.18: Sample spectra presenting the background subtraction methods for the elastically scattered protons (left panel) and deuterons (right panel). The red lines represent the assumed background functions.

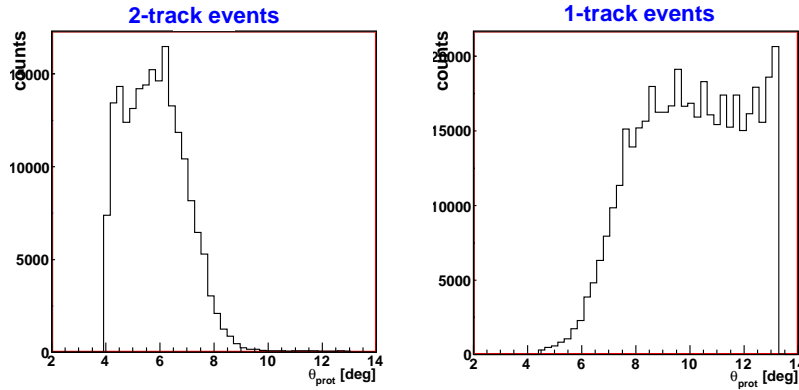


Figure 5.19: Elasticity scattered protons shown as proton-deuteron coincidences (2-tracks events) below $\theta_p = 7^\circ$ (left panel) and as single-track events (right panel). The border of $\theta_p = 7^\circ$, separating the two event classes is well distinguishable.

For each polar angle analogous projections were prepared with the integration range of $\Delta\theta = 1^\circ$.

In the next step of the analysis background subtraction was performed. For the elastic protons in their energy spectrum an arbitrary E_a and E_b values (dashed lines in Fig. 5.18, left panel) were chosen for each $\Delta\theta$ bin, which defined the accepted energy range. As one can notice, the elastic protons are grouped in a prominent peak with only a low background of the breakup events. Due to this fact the choice of the integration limits was not so critical. Between E_a and E_b a linear dependence of background was assumed and its subtraction in each bin of the spectrum was done. Linear function, which describes the background fitted to a sample distribution is presented in Fig. 5.18, left panel. Additionally, due to the fact that the elastic protons are also recognized as $p-d$ coincidences for $\theta_p < 7^\circ$ (see Fig. 5.19), the relative angle between the two particles $\varphi_{pd} = 180^\circ \pm 30^\circ$ was also imposed, as it is shown in Fig. 5.20.

In case of the elastically scattered deuterons background is mainly caused by beam particles. A typical energy distribution is shown in Fig. 5.18, right panel. Gaussian function

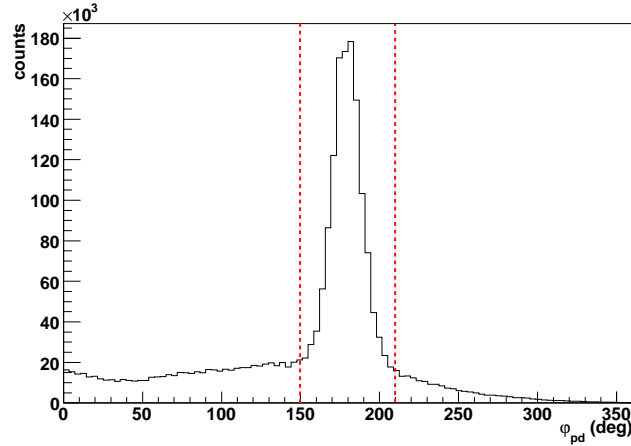


Figure 5.20: Number of events presented as a function of φ_{pd} for the proton-deuteron coincidences for $\theta_p < 7^\circ$. Vertical lines show the range of φ_{pd} angles accepted in the analysis.

(red curve in Fig. 5.18 on the right panel) with fixed mean position and fwhm value was used as a background model and fitted to the deuteron energy distribution at each θ range. The background events were almost completely eliminated for higher polar angles, whereas for very small ($\theta < 7^\circ$) polar angles the rest-overs of the beam are still present.

5.8.2 Beam polarization

In result of the above procedures, the numbers of the elastically scattered protons and deuterons at given polar angle θ_p and azimuthal angle φ for polarized and unpolarized beam states were obtained. They have been relatively normalized to the number of counts collected in the Veto detector, which is proportional to the beam current. Afterwards, the event numbers have been corrected for the dead time and scaled by an adequate trigger factor. On their basis a ratio $f^{\theta_p}(\varphi)$ was constructed:

$$f^{\theta_p}(\varphi) = \frac{N_{pol}^{\theta_p} - N_0^{\theta_p}}{N_0^{\theta_p}}, \quad (5.7)$$

where $N_{pol}^{\theta_p}$ and $N_0^{\theta_p}$ denote final numbers of events evaluated for the polarized and unpolarized beam, respectively. In the ratio corrections connected with the background subtraction are significant, whereas all factors constant in time e.g. target thickness, detection efficiency, etc., are cancelled.

In general, number of the elastically scattered events $N_{pol}^{\theta_p}$ obtained from polarized state is described by a formula:

$$N_{pol}^{\theta_p}(\varphi) = N_0^{\theta_p}(\varphi) \cdot \kappa \cdot \left[1 + iT_{11}(\theta_p) \cdot \sqrt{3}P_z \cos \varphi - T_{22}(\theta_p) \frac{\sqrt{3}}{2} P_{zz} \cos 2\varphi - T_{20}(\theta_p) \frac{\sqrt{2}}{4} P_{zz} \right], \quad (5.8)$$

where $iT_{11}(\theta)$ and $T_{22}(\theta)$, $T_{20}(\theta)$ are spherical vector and tensor analyzing powers, and κ is the ratio of normalization factors for the two states. Due to the fact that only pure

vector beam polarization state was available in the experiment, the formula 5.8 simplifies as follows:

$$N_{pol}^{\theta_p}(\varphi) = N_0^{\theta_p} \cdot \kappa \cdot [1 + iT_{11}(\theta_p)\sqrt{3}P_z \cos \varphi]. \quad (5.9)$$

Substituting the formula 5.9 into Eq. 5.7 allows to obtain the final expression for the theoretical dependency $f^{\theta_p}(\varphi)$ as a function of the angle φ for vector polarized beam state:

$$f^{\theta_p}(\varphi) = \kappa \cdot iT_{11}(\theta_p)P_z\sqrt{3} \cos \varphi + \kappa - 1. \quad (5.10)$$

This expression can be rewritten with the use of two parameters a, b, which can be extracted from a fit of the experimental asymmetry function $f^{\theta_p}(\varphi)$, obtained as in Eq. 5.7:

$$f^{\theta_p}(\varphi) = a \cdot \cos \varphi + b, \quad (5.11)$$

therefore the P_z value and κ coefficient can be calculated in a very simple way if the analyzing power iT_{11} is known:

$$P_z = \frac{a}{(b+1)iT_{11}\sqrt{3}}, \quad (5.12)$$

$$\kappa = b + 1. \quad (5.13)$$

In the region of very forward polar angles $\theta^{LAB} \leq 13^\circ$ values of the elastic scattering analyzing powers were obtained in the KVI experiment [71,72]. The values for $\theta^{LAB} = 13^\circ$ (for protons and deuterons) were used here to evaluate final beam polarization. The final results for the two experimental runs are presented in Fig. 5.21 and summarized in Table 5.2. Additionally, the κ coefficients were estimated in order to control the normalization procedure. The procedure proves to work reliably taking into consideration their close to unity values and the errors.

| run number | (P_z, P_{zz}) | P_z | ΔP_z^{stat} | P_{zz} | ΔP_{zz}^{stat} | κ | $\Delta \kappa^{stat}$ |
|------------|---------------------|--------|---------------------|----------|------------------------|----------|------------------------|
| 1 | $(-\frac{2}{3}, 0)$ | -0.562 | 0.018 | -0.054 | 0.064 | 1.0067 | 0.0025 |
| 2 | $(-\frac{2}{3}, 0)$ | -0.484 | 0.027 | 0.13 | 0.11 | 0.9895 | 0.0046 |

Table 5.2: Values of the vector beam polarization and of the normalization coefficients κ obtained for both experimental runs.

5.8.3 Vector analyzing power of the elastic scattering

The extracted beam polarization P_z at one angular point can be further used to determine iT_{11} analyzing powers for the $^1H(\vec{d}, d)p$ elastic scattering process. Fitting $f(\varphi)$ asymmetry function at other θ angles within the acceptance of the detector, the iT_{11} values can be obtained. These by-product results constitute a valuable contribution to the angular range of data for this observable in the area not covered by other experiments. Obtained in this work values, together with other data sets, are presented in Fig. 5.22. The data agree very well with the theoretical predictions of various approaches. In the very small angles region one can even tend to deduce correct Coulomb force corrections to the iT_{11} distribution.

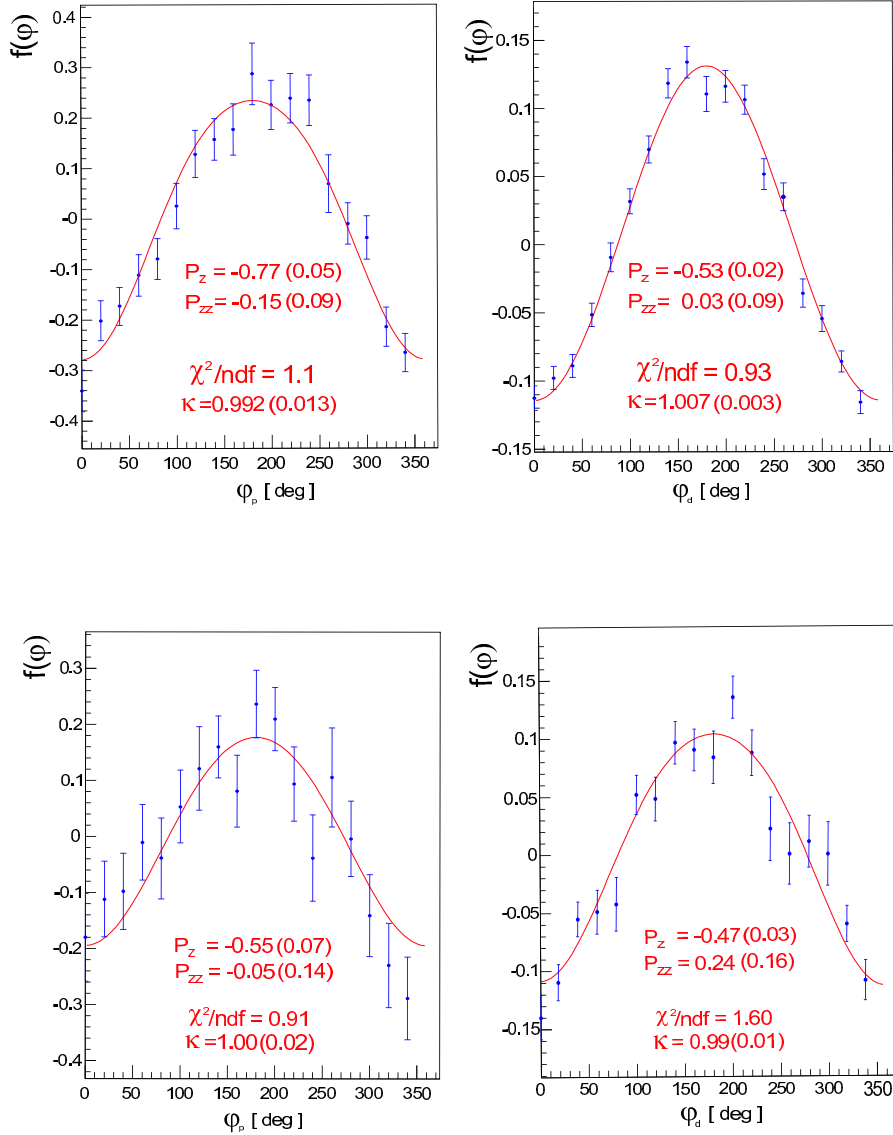


Figure 5.21: Ratios $f(\varphi)$ for vector polarization state (the nominal polarizations value $(P_z, P_{zz}) = (-2/3, 0)$) obtained for the protons (left panels) and deuterons (right panels) for one chosen polar angle $\theta^{LAB} = 13^\circ$. The error bars represent statistical uncertainties. The lines refer to the results of the fit, as specified in the text. Presented are results from the first (upper panels) and the second (lower panels) experimental runs.

5.9 Efficiency of the detection system

In order to obtain the absolute values of the breakup cross section, it is necessary to take into account inefficiency of the detection system. Determining the GeWall detectors efficiencies is a procedure of finding scaling factors for the obtained numbers of the breakup coincidences $N_{br}(S, \Omega_1, \Omega_2)$ registered at the angles $\Omega_1 \equiv (\theta_1, \varphi_1)$ and $\Omega_2 \equiv (\theta_2, \varphi_2)$. Probability of detecting a charge particle is connected with a finite efficiency of each element of the Quirl detector (spiral) and the Pizza detectors (sector). During the exper-

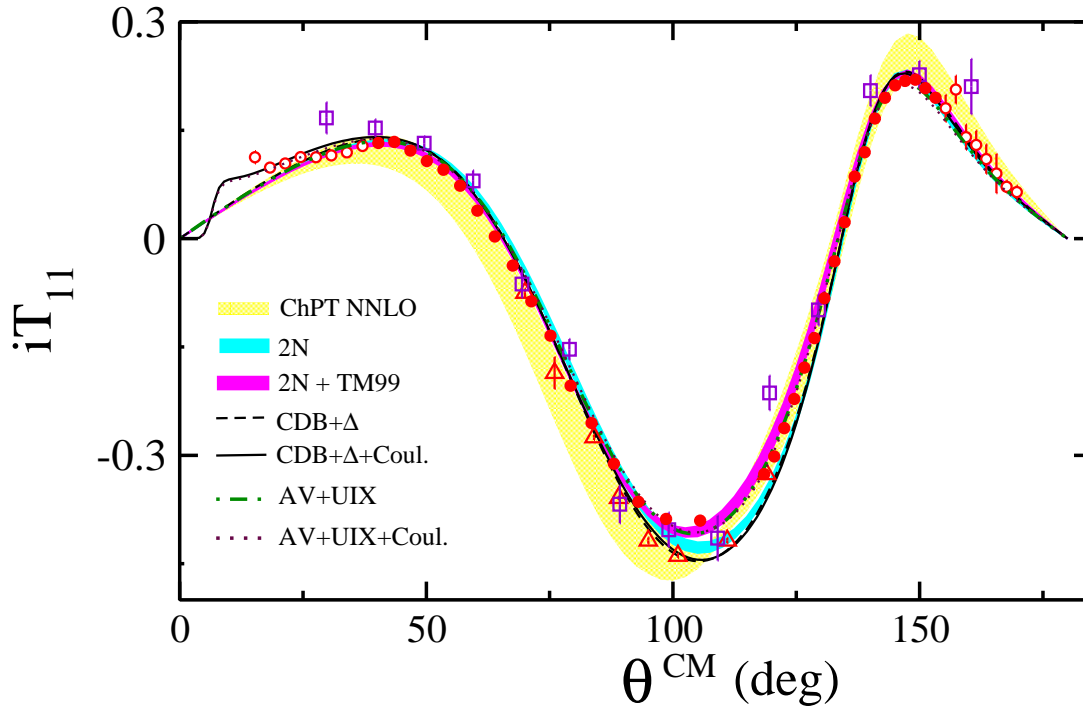


Figure 5.22: Vector analyzing power iT_{11} for the $d-p$ elastic scattering at 130 MeV: present experiment (red circles), KVI data (full red dots) [71] and earlier data sets: RIKEN data (red triangles) [73] and data from Ref. [74] (violet squares). Theoretical predictions of different approaches specified by the legend are also presented.

iment certain spirals or sectors can become inefficient i.e. they can function with lower efficiency or cease to function at all (“dead” spirals/sectors), what causes quite significant effect. Additionally, due to the fact that the events of interest are coincidences of two particles, the obtained clusters, which represent the particles, can overlap if the protons are at a very small distance from each other (for the relative azimuthal angle $\varphi_{12} \leq 60^\circ$). This factor influences only Quirl and Pizza 1 detectors.

The above effects can affect the measured angular distributions and even distort them. In order to eliminate their role and compensate the experimental counting rates, the correction factors and maps of efficiency were prepared for the GeWall components.

5.9.1 Efficiency of the Quirl detector

In the case of the Quirl detector the correction factors were determined mainly with the use of simulation. This has been achieved in few steps.

In the first step the Monte Carlo simulations of the breakup process were performed with the use of GEANT 4 package. A software image of the experimental setup, i. e. the materials, dimensions and distances of all GeWall detectors, was implemented. Then the simulation was performed for all kinematical configurations which are analyzed in this dissertation. As the results, all information on the emitted protons, like energy losses in each GeWall detector, polar and azimuthal angles, were obtained. In order to establish the size of the “overlapping cluster” effect and its influence on the breakup cross section

values, additional routine was used. In this procedure radius of the spots characterizing the charge splitting on the spirals R_Q was assumed to be 0.2 mm (for both sides of the detector) chosen such, that the experimental distributions of cluster hit multiplicities were reproduced. The above model is very naive and obtained efficiency factors are biased with high systematic uncertainties. They only affect cross section distributions for few kinematical configurations characterized by the relative angles φ_{12} between 20° and 100° , see Sec. 5.11 for more details). In order to obtain reliable estimation of the efficiency correction parameters the model needs further improvements. The inefficiency connected with the "dead" (see Fig. 5.23) or noisy spirals of the Quirl detector, were taken into account in the model. The clusters, which contain any of the damaged spirals were removed from the analysis. However, events with the clusters containing damaged spirals on the edges of the given cluster were counted, but they appeared as the ones with the lower energy. Existence of the two above effects contributes to the efficiency of the Quirl detector and the associated correction factor (probability of registration of two coincident protons) for a given configuration is described as follows:

$$\varepsilon_Q(\Omega_1, \Omega_2) = 1 - \frac{N_1(\Omega_1, \Omega_2)}{N(\Omega_1, \Omega_2)}, \quad (5.14)$$

where N_1 denotes the number of the simulated breakup events counted as the ones, which were affected by the overlapping clusters or by the non-functional spirals, whereas N is the total number of events for a given configurations of the two protons.

In case of the single-track events there are no such effect like "overlapping clusters". Therefore, the correction factor, which contributes to the total efficiency is connected only with the existence of "dead" or noisy spirals of the Quirl detector. In order to establish the factors, referred to as $\varepsilon_Q^{sp}(\theta^{el})$, an analogous procedure to the one applied for the two-track events was used with the same value of the parameter R_Q . The correction

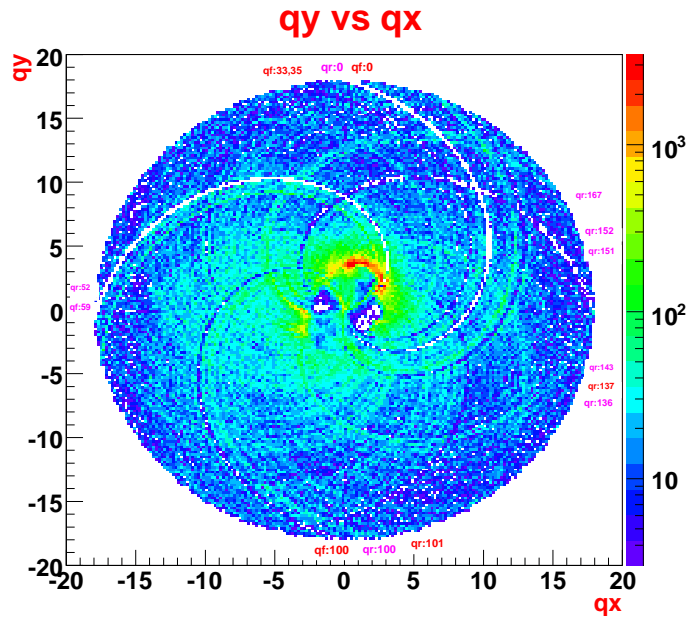


Figure 5.23: Events projected on the x-y plane of the Quirl detector. Not working spirals on both detector sides are visible. The numbers of malfunctioning spirals are indicated in the picture.

factors are given by:

$$\varepsilon_Q^{sp}(\theta^{el}) = 1 - \frac{N_1(\theta^{el})}{N(\theta^{el})}, \quad (5.15)$$

where N_1 denotes the number of the simulated $d - p$ elastic scattering events, which were affected by the non-functional spirals, whereas N is the total number of events for a given polar angle θ^{el} of the elastic proton.

5.9.2 Efficiency of Pizza 1 detector

In the case of the Pizza 1 detector the factors $\varepsilon_{P1}^{cl}(\Omega_1, \Omega_2)$ connected with the ‘‘overlapping clusters’’ were determined in the same way as for the Quirl detector. Here, the radius of the spot characterizing the charge splitting on the sectors was established on the experimental basis to be 0.5 mm. Additionally, the map of efficiency was obtained. Due to the fact that there was no trigger for single particle not registered in Pizza 1, only coincident events were investigated (GW2 trigger condition - see Sec. 4.3.5). For this purpose unusual tracks were built as a combination of QF/QR and Pizza 2 (incomplete track), and two kinds of medium track - long track coincidences were counted in the angular ranges of $\Delta\theta = 2^0$, $\Delta\varphi = 10^0$:

1. (Quirl-Pizza 1) - (Quirl-Pizza 1-Pizza 2) - complete track,
2. (Quirl-Pizza 1) - (Quirl-Pizza 2) - incomplete track with missing Pizza 1 information.

The detection efficiency of Pizza 1 is defined as follows:

$$\varepsilon_{P1}^{cl}(\theta, \varphi_1) = \frac{N_{Q-P1-P2}(\theta, \varphi)}{N_{Q-P1-P2}(\theta, \varphi) + N_{Q-P2}(\theta, \varphi)}, \quad (5.16)$$

where $N_{Q-P1-P2}(\theta, \varphi)$ denotes the number of coincidences of the type 1 and θ, φ are related to the particle with the long track, whereas the $N_{Q-P2}(\theta, \varphi)$ defines the number of coincidences of the type 2. The obtained efficiency in function of φ angles for four chosen θ angles is presented in Fig. 5.25 and for all angular bins the efficiency map is shown in Fig. 5.24. The efficiency is generally above 85%.

5.9.3 Efficiency of the Pizza 2 detector

In order to obtain the map of efficiency for the Pizza 2 detector the single-track events were used. Having $\Delta E(qr)$ vs $E(p1)$ dependency (see Fig. 5.5 in Sec. 5.4), the elastic protons were chosen with the $\Delta E(qr)$ energy range of $2.5 \div 5.5$ MeV and $\Delta E(p1)$ energy range of $30 \div 48$ MeV. These particles have energies large enough to always pass the Pizza 1 and reach the Pizza 2 detector. Thus, the numbers of the elastically scattered protons were counted in the angular segments of $\Delta\theta = 2^0$, $\Delta\varphi = 10^0$ separately under the two following conditions:

1. energy loss in the Pizza 2 detector $E(p2) = 0$: $N_{Q,P1}(\theta, \varphi)$,
2. energy loss in the Pizza 2 detector $E(p2) > 0$: $N_{Q,P1,P2}(\theta, \varphi)$.

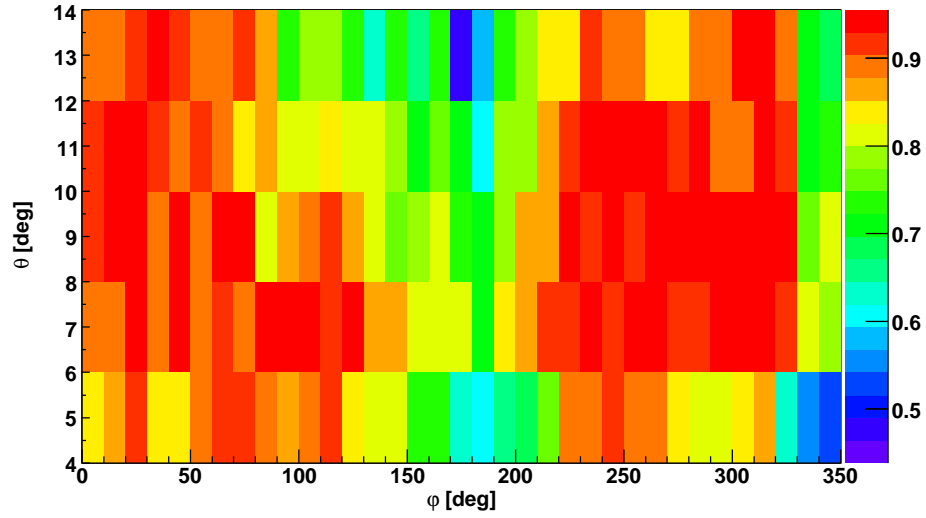


Figure 5.24: Efficiency map of Pizza 1 presented in function of polar (θ) and azimuthal (ϕ) angles. The range of polar angle θ is from 3° to 14° with the binning of 2° and the azimuthal angle ϕ covers the full range, with the binning of 10° .

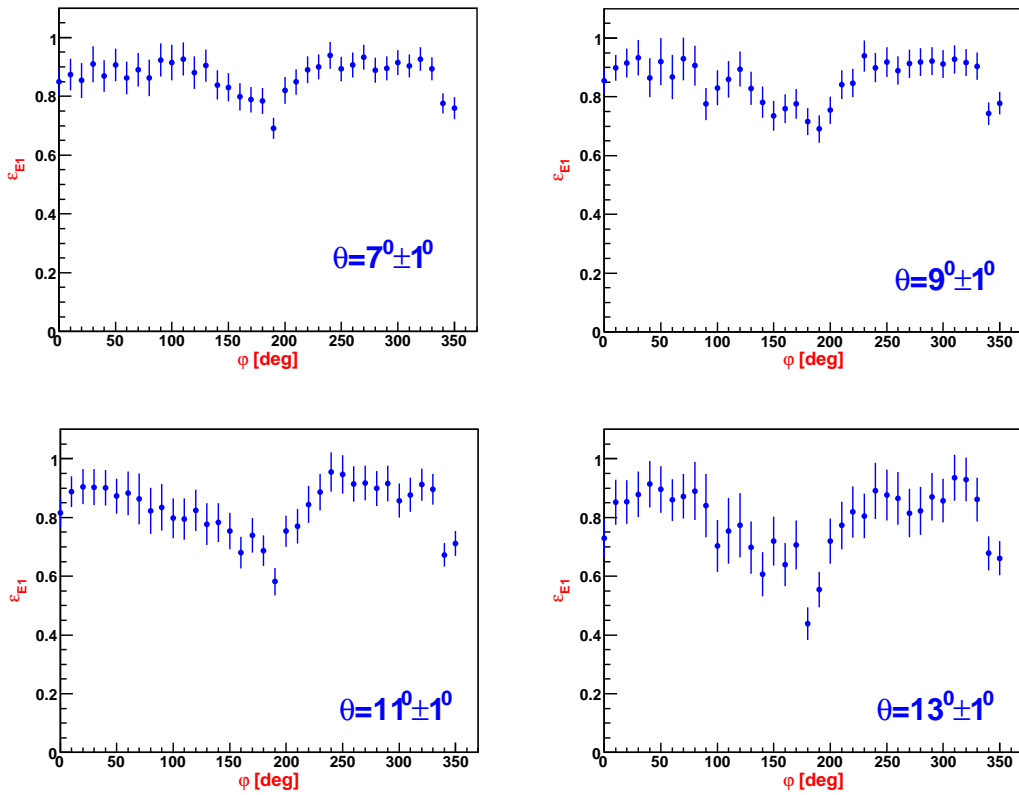


Figure 5.25: Detection efficiency of the Pizza 1 detector for four chosen θ angles.

The efficiency of Pizza 2 is given as:

$$\varepsilon_{P2}(\theta, \varphi) = \frac{N_{Q,P1,P2}(\theta, \varphi)}{N_{Q,P1,P2}(\theta, \varphi) + N_{Q,P1}(\theta, \varphi)}. \quad (5.17)$$

The obtained map of Pizza 2 efficiency is presented in Fig. 5.26. The efficiency in function of φ angles for four chosen θ angles is shown in Fig. 5.27. As one can notice, the efficiency of the Quirl detector clearly influences the efficiency of Pizza 2, what is visible in Figs. 5.26, 5.27 as the “floating“ dips. This effect is connected with the inefficient places on the Quirl detector plane due to non-functional spirals (see Fig. 5.23), what causes the movement of the dips with the θ angle. The bending direction of the front or rear spirals is reflected in the dips movement direction.

Finally the Pizza 2 efficiency was assumed to be constant at a given polar angle and was calculated from the weighted average of the numbers of counts at several azimuthal angles (the regions with very low efficiency were omitted). The resulting efficiency values are marked with red lines in the sample distributions in Fig. 5.27. The efficiency is generally above 90%, but at the edges of the experimental acceptance it decreases to about 77%.

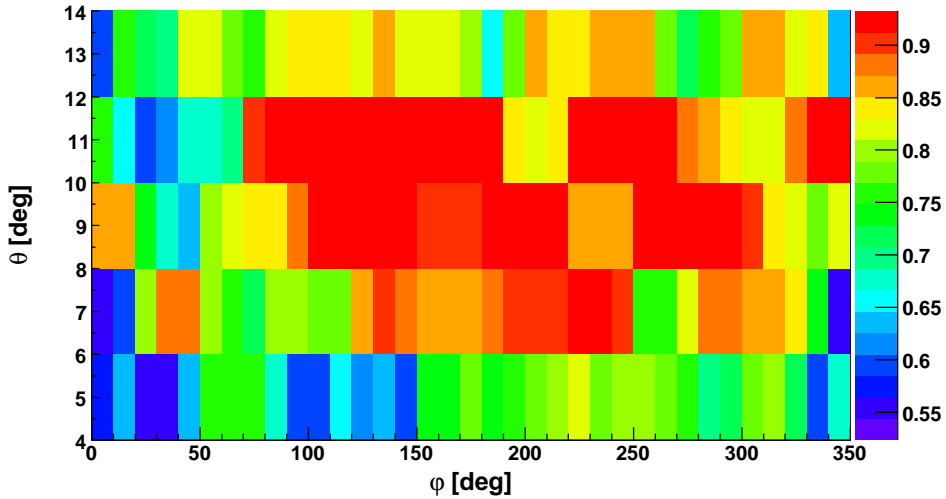


Figure 5.26: Efficiency map of Pizza 2 presented in function of polar (θ) and azimuthal (φ) angles. The range of polar angle θ is from 3° to 14° with the binning of 2° and the azimuthal angle φ covers the full range, with the binning of 10° .

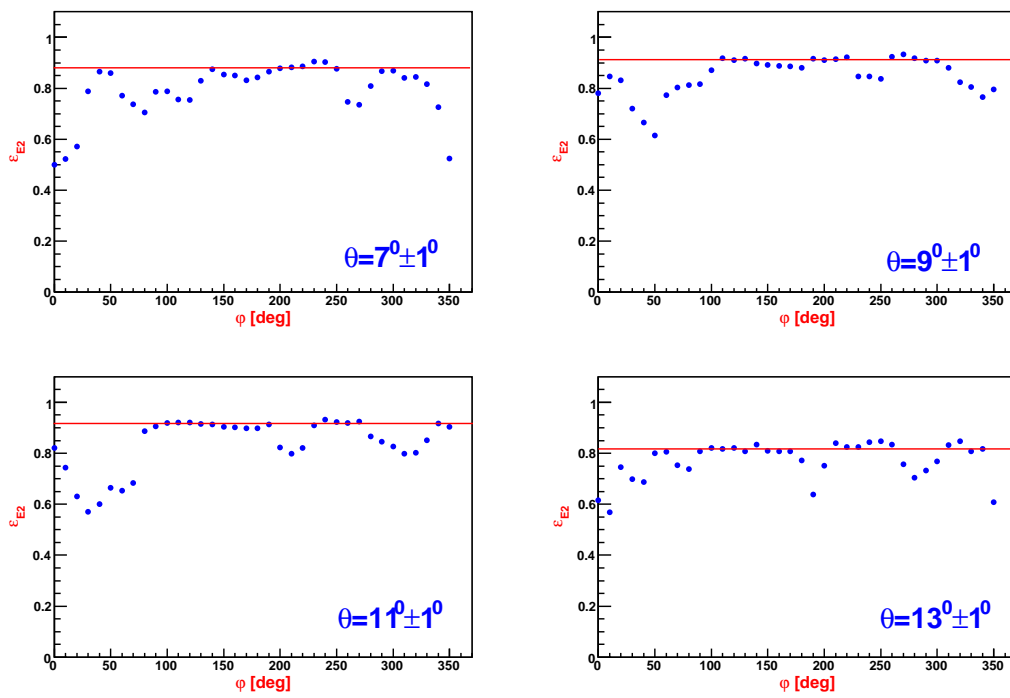


Figure 5.27: Detection efficiency of the Pizza 2 detector for four chosen θ angles. The statistical errors are within the dot size. The red lines correspond to the calculated weighted averages from the numbers of counts for several azimuthal angles, with regions of very low efficiency omitted.

5.10 Evaluation of the breakup observables

In the analysis of the breakup reaction two new variables were introduced in the $E_1 - E_2$ plane: D denoting the distance of the (E_1, E_2) point from the theoretical kinematical curve, and S , which defines the arc-length along the kinematics with the starting point at the E_2 minimum, see Chap. 2. These new variables are presented in Fig. 5.28.

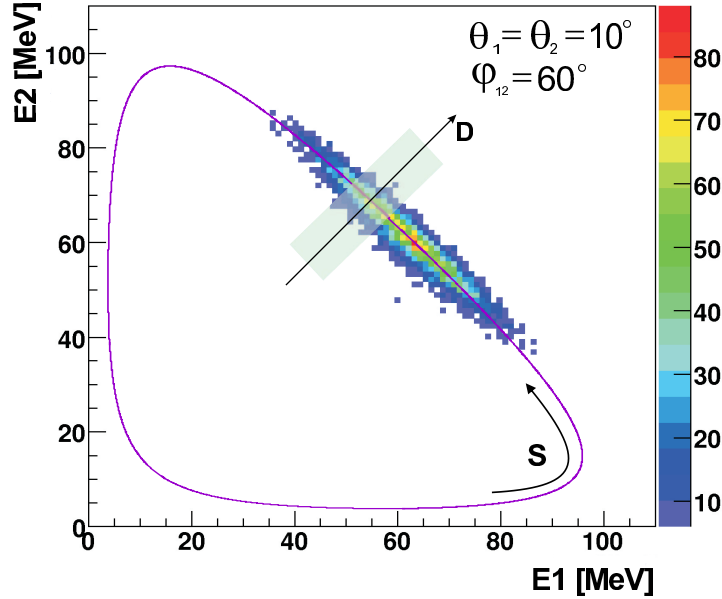


Figure 5.28: A sample E_2 vs. E_1 energy spectrum for a selected angular configuration of the breakup process: $\theta_1 = 10^\circ$, $\theta_2 = 10^\circ$, $\varphi_{12} = 60^\circ$. Direction of arc-length S and the D -axis in one ΔS bin of events integration (schematically marked) are shown.

5.10.1 Selection of events

With the use of the $\Delta E - E$ technique, the proton events were chosen (see also Sec. 5.4). The events grouped on the $\Delta E(qr)$ versus $E(p1 + p2)$ spectrum were surrounded by lines which define an arbitrary area, wide enough to avoid any losses of protons. Fig. 5.29 presents such an identification spectrum with the chosen gate. Two-track events, with both particles identified as protons, were selected as coincident breakup events.

Both of the selected coincident protons are characterized by their emission angles θ_1 and θ_2 and their relative azimuthal angle φ_{12} , which altogether defines geometrical configuration of the outgoing protons. In the first step a kinematical spectra E_1 vs E_2 for certain two-proton configurations were constructed. The events integration ranges were chosen for the breakup cross section analysis to be: $\Delta\theta_1 = \Delta\theta_2 = 2^\circ$, $\Delta\varphi_{12} = 10^\circ$ and for the analyzing powers study as: $\Delta\theta_1 = \Delta\theta_2 = 3^\circ$, $\Delta\varphi_{12} = 40^\circ$. These integration limits are wide enough to reach good statistical accuracy. As one can notice in Fig. 5.28, the events are concentrated along the kinematical curve, what proves that the breakup events were extracted quite cleanly. For further analysis only the events lying within the band of D -values ranging from -8 MeV to $+8$ MeV were used, as shown in Fig. 5.30. The

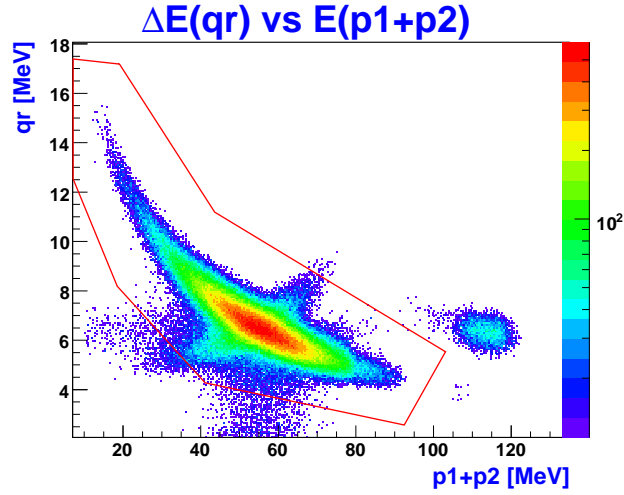


Figure 5.29: Example of the particle identification spectrum. Lines surround arbitrary chosen area, within which particle is identified as a breakup proton.

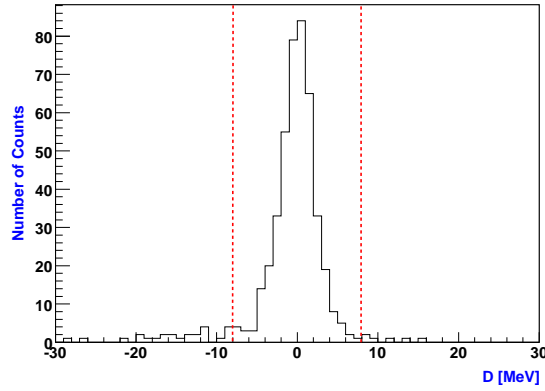


Figure 5.30: Projection of the events originating from the marked ΔS bin area (presented in Fig. 5.28) onto D-axis. The accepted range of D-values is indicated with the red lines.

spectrum in Fig. 5.30 was obtained by projecting the events from one slice $\Delta S=8$ MeV (marked area in Fig. 5.28) onto the D-axis. As one can notice, the breakup events are grouped in a prominent peak with only a very low background of accidental coincidences. Due to this fact the choice of the integration limits was not so critical and the selected ranges were practically the same for all investigated kinematical configurations.

5.10.2 Determination of the breakup cross section

The breakup cross section normalization was performed with the use of the known $p-d$ elastic scattering cross section data [42]. This procedure was possible due to the fact that the breakup and elastic scattering reactions were measured simultaneously. Therefore, a crucial quantity, which had to be determined was the number of the elastic scattering events. In order to achieve this purpose, elastic deuterons were selected and their numbers corrected for the background subtraction in a way described in details in Sec. 5.8.1. The numbers of such events were counted for each polar θ angle within the angular ranges of $\Delta\theta = 2^\circ$ and $\Delta\varphi_{12} = 10^\circ$.

The breakup protons grouped around the kinematical curve were divided into $\Delta S=8$ MeV and projected onto the central kinematic. For a given S -bin in the selected configuration, number N_{br} of the coincident protons was established.

Number of the breakup coincidences $N_{br}(S, \Omega_1, \Omega_2)$ registered at the $\Omega_1 \equiv (\theta_1, \varphi_1)$ and $\Omega_2 \equiv (\theta_2, \varphi_2)$ and in a given ΔS arc-length bin, could be written as follows:

$$\begin{aligned} N_{br}(S, \Omega_1, \Omega_2) &= \sum_{i=0}^{i=35} N_{br}(S, \Omega_1, \Omega_2, \varphi_1^i) \\ &= \frac{d^5\sigma}{d\Omega_1 d\Omega_2 dS}(S, \theta_1, \theta_2, \varphi_{12}) \cdot \Delta\Omega_1 \Delta\Omega_2 \Delta S \cdot C(t) \cdot \varepsilon(S, \Omega_1, \Omega_2), \end{aligned} \quad (5.18)$$

where the sum runs over 10^0 bins of φ_1 due to the fact that the cross section does not depend on that variable - thus, to improve statistics the events can be summed over φ_1 and for $\pm\varphi_{12}$ configurations. The $\frac{d^5\sigma}{d\Omega_1 d\Omega_2 dS}$ is the breakup cross section for a chosen angular configuration, $\Delta\Omega_j = \Delta\theta_j \Delta\varphi_j \sin\theta_j$, $j = 1, 2$, are the solid angles. The $\varepsilon(S, \Omega_1, \Omega_2)$ contains all efficiencies and correction factors (see Chap. 5.9) and is given in general by:

$$\begin{aligned} \varepsilon(S, \Omega_1, \Omega_2) &= \varepsilon_Q(\Omega_1, \Omega_2) \cdot \varepsilon_{P1}^{cl}(\Omega_1, \Omega_2) \varepsilon_{P2}(\theta_1) \varepsilon_{P2}(\theta_2) \times \\ &\times \sum_{i=0}^{i=35} \varepsilon_{P1}(\theta_1, \varphi_1^i) (\varepsilon_{P1}(\theta_2, \varphi_1^i + \varphi_{12}) + \varepsilon_{P1}(\theta_2, \varphi_1^i - \varphi_{12})). \end{aligned} \quad (5.19)$$

The term of the sum given as $(\varepsilon_{P1}(\theta_2, \varphi_1^i + \varphi_{12}) + \varepsilon_{P1}(\theta_2, \varphi_1^i - \varphi_{12}))$ is taking into account common treatment of the mirror configurations $\varphi_2 = \varphi_1 \pm \varphi_{12}$. Moreover, one has to realize that depending on the energy of the protons, efficiency of the Pizza 2 detector can contribute or not to the total efficiency $\varepsilon(S, \Omega_1, \Omega_2)$, what leads to the following scenarios:

1. proton number 1 was registered in Pizza 2, whereas proton number 2 reached only Pizza 1 detector:

$$\begin{aligned} \varepsilon(S, \Omega_1, \Omega_2) &= \varepsilon_Q(\Omega_1, \Omega_2) \cdot \varepsilon_{P1}^{cl}(\Omega_1, \Omega_2) \varepsilon_{P2}(\theta_1) \times \\ &\times \sum_{i=0}^{i=35} \varepsilon_{P1}(\theta_1, \varphi_1^i) (\varepsilon_{P1}(\theta_2, \varphi_1^i + \varphi_{12}) + \varepsilon_{P1}(\theta_2, \varphi_1^i - \varphi_{12})). \end{aligned} \quad (5.20)$$

2. proton number 2 was registered in Pizza 2, whereas proton number 1 reached only Pizza 1 detector:

$$\begin{aligned} \varepsilon(S, \Omega_1, \Omega_2) &= \varepsilon_Q(\Omega_1, \Omega_2) \cdot \varepsilon_{P1}^{cl}(\Omega_1, \Omega_2) \varepsilon_{P2}(\theta_2) \times \\ &\times \sum_{i=0}^{i=35} \varepsilon_{P1}(\theta_1, \varphi_1^i) (\varepsilon_{P1}(\theta_2, \varphi_1^i + \varphi_{12}) + \varepsilon_{P1}(\theta_2, \varphi_1^i - \varphi_{12})). \end{aligned} \quad (5.21)$$

3. both of the detected protons reached only Pizza 1 detector:

$$\begin{aligned} \varepsilon(S, \Omega_1, \Omega_2) &= \varepsilon_Q(\Omega_1, \Omega_2) \cdot \varepsilon_{P1}^{cl}(\Omega_1, \Omega_2) \times \\ &\times \sum_{i=0}^{i=35} \varepsilon_{P1}(\theta_1, \varphi_1^i) (\varepsilon_{P1}(\theta_2, \varphi_1^i + \varphi_{12}) + \varepsilon_{P1}(\theta_2, \varphi_1^i - \varphi_{12})). \end{aligned} \quad (5.22)$$

4. both of the detected protons reached Pizza 2 detector (this situation never occurs):

$$\begin{aligned} \varepsilon(S, \Omega_1, \Omega_2) &= \varepsilon_Q(\Omega_1, \Omega_2) \cdot \varepsilon_{P1}^{cl}(\Omega_1, \Omega_2) \varepsilon_{P2}(\theta_1) \varepsilon_{P2}(\theta_2) \times \\ &\times \sum_{i=0}^{i=35} \varepsilon_{P1}(\theta_1, \varphi_1^i) (\varepsilon_{P1}(\theta_2, \varphi_1^i + \varphi_{12}) + \varepsilon_{P1}(\theta_2, \varphi_1^i - \varphi_{12})). \end{aligned} \quad (5.23)$$

Depending on the situation, one has to apply one of the above formulae.

The $C(t)$ is the factor related to the luminosity, which depends on the total beam current I_0 , the density ρ_t and the thickness Δx_t of the target, as well as the electronic dead time τ . Therefore, the above parameter could be written as follows:

$$C(t) = (1 - \tau) I_0 \rho_t \Delta x_t. \quad (5.24)$$

In the similar way one can write the number of the elastic scattering events, $N_{el}(\Omega_1^{el})$, with the deuteron registered at the angle Ω_1^{el} (what defines the proton detection angle Ω_2^{el}), which is expressed by:

$$\begin{aligned} N_{el}(\Omega_1^{el}) &= \sum_{i=0}^{i=35} N_{el}(\theta_1^{el}, \varphi_1^i) \\ &= \frac{d\sigma}{d\Omega_1^{el}}(\theta_1^{el}) \cdot \Delta\Omega_1^{el} \cdot C(t) \cdot \varepsilon(\Omega_1^{el}, E_1^{el}), \end{aligned} \quad (5.25)$$

where the $\frac{d\sigma}{d\Omega_1^{el}}$ is the elastic scattering cross section, and the other factors are analogous to the ones defined above.

The $\varepsilon(\Omega_1^{el}, E_1^{el})$ is related to the efficiencies and correction factors obtained with respect to the single-track events and is expressed as:

$$\varepsilon(\Omega_1^{el}, E_1^{el}) = \varepsilon_Q^{sp}(\theta_1^{el}) \varepsilon_{P2}(\theta_1^{el}) \sum_{i=0}^{i=35} \varepsilon_{P1}(\theta_1^{el}, \varphi_1^i) \varepsilon_{P1}(\theta_1^{el}, \varphi_1^i + \pi), \quad (5.26)$$

Finally, the breakup cross section could be expressed in terms of the elastic scattering cross section due to the fact that both of these reactions were measured simultaneously. Therefore, the factor $C(t)$ is the same in the Eqs. 5.18 and 5.25. Taking advantage of the above conclusion, the final formula for the differential breakup cross section for a given angular configuration can be expressed as follows:

$$\begin{aligned} \frac{d^5\sigma}{d\Omega_1 d\Omega_2 dS} (S, \theta_1, \theta_2, \varphi_{12}) &= \frac{d\sigma_{el}}{d\Omega_1^{el}}(\theta_1^{el}) \cdot \frac{N_{br}(S, \Omega_1, \Omega_2)}{N_{el}(\Omega_1^{el})} \times \\ &\times \frac{\Delta\Omega_1^{el}}{\Delta\Omega_1 \Delta\Omega_2 \Delta S} \cdot \frac{\varepsilon(\Omega_1^{el}, E_1^{el})}{\varepsilon(S, \Omega_1, \Omega_2)}. \end{aligned} \quad (5.27)$$

The elastic scattering cross section was taken from [42].

Fig. 5.31 shows a sample breakup cross section distribution for a chosen kinematical configuration, together with the full set of theoretical calculations. More results are presented in Appendix A.

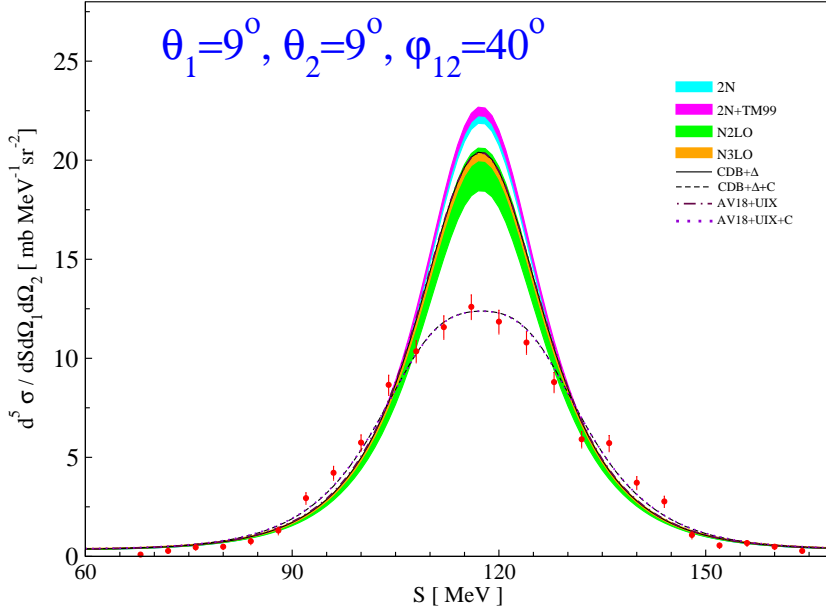


Figure 5.31: Example of the differential breakup cross section for the angular configuration specified in the picture. Theoretical predictions are shown as bands and lines, as specified in the legend.

5.10.3 Vector analyzing powers of the breakup process

In the case of the vector analyzing powers analysis the protons grouped around the kinematical curve were divided into ΔS bins having width of 16 MeV and projected on the central kinematics. For a given S – bin in the selected configuration and assumed D – bin of 16 MeV (see also previous Section), the numbers of the breakup events as a function of the azimuthal angle φ_1 have been counted. The width of φ_1 bin was chosen to be 20° . The obtained numbers of events were normalized to the beam current, corrected for the dead time and scaled by an adequate trigger factor.

In the next step, the ratios, similar to the ones introduced in the elastic scattering analysis (see Sec. 5.8.2), were built for each S bin:

$$f^\xi(\varphi_1) = \frac{N_{pol}^\xi(\varphi_1) - N_0^\xi(\varphi_1)}{N_0^\xi(\varphi_1)}, \quad (5.28)$$

where (ξ, φ_1) defines a given kinematical point $(\theta_1, \theta_2, \varphi_{12}, S, \varphi_1)$ and $N_{pol}^\xi(\varphi_1)$, $N_0^\xi(\varphi_1)$ denote the numbers of events for polarized ($P_z = -\frac{2}{3}$, $P_{zz} = 0$) and unpolarized ($P_z = 0$, $P_{zz} = 0$) beam states, respectively.

For the breakup process $f^\xi(\varphi_1)$ is in general expressed by the formula:

$$\begin{aligned} f^\xi(\varphi_1) = & -\frac{3}{2} \sin \varphi_1 P_z A_z(\xi) + \frac{3}{2} \cos \varphi_1 P_z A_y(\xi) \\ & + \frac{1}{2} \sin^2 \varphi_1 P_{zz} A_{xx}(\xi) + \frac{1}{2} \cos^2 \varphi_1 P_{zz} A_{yy}(\xi) \\ & - \cos \varphi_1 \sin \varphi_1 P_{zz} A_{xy}(\xi), \end{aligned} \quad (5.29)$$

where A_x and A_y denote vector analyzing powers, whereas A_{xx} , A_{yy} and A_{xy} are the

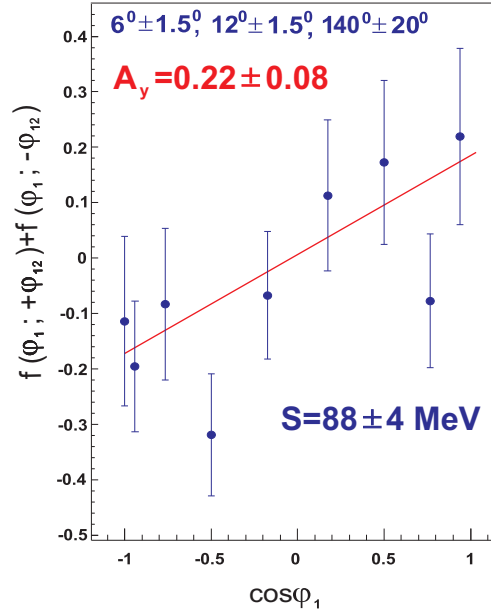


Figure 5.32: A sample dependency of f^ξ combination from Eq. 5.32 vs. $\cos \varphi_1$ for 16 MeV wide S-bin centered at 88 MeV for the chosen kinematical configuration specified in the picture. The solid line represents fit of the linear function 5.32 to the data points with experimental value of P_z taken from Tab. 5.2. The resulting from the fit value of A_y is displayed in the panel.

tensor analyzing powers.

The $f^\xi(\varphi_1)$ dependency for pure vector polarized beam state simplifies to:

$$f^\xi(\varphi_1) = \frac{3}{2} P_z (A_y(\xi) \cos \varphi_1 - A_x(\xi) \sin \varphi_1). \quad (5.30)$$

Thus, the values of A_x and A_y can be extracted in a very simple way, if one computes combinations of $f^\xi(\varphi_1)$ obtained separately for $+\varphi_{12}$ and $-\varphi_{12}$ (taking advantage of the parity restrictions, see Sec. 2.3):

$$f^{\xi \equiv (\theta_1, \theta_2, +\varphi_{12}, S)}(\varphi_1) - f^{\xi \equiv (\theta_1, \theta_2, -\varphi_{12}, S)}(\varphi_1) = 3P_z A_x(\xi) \sin \varphi_1, \quad (5.31)$$

$$f^{\xi \equiv (\theta_1, \theta_2, +\varphi_{12}, S)}(\varphi_1) + f^{\xi \equiv (\theta_1, \theta_2, -\varphi_{12}, S)}(\varphi_1) = 3P_z A_y(\xi) \cos \varphi_1. \quad (5.32)$$

Using the beam polarization P_z obtained from the elastic scattering analysis (see Sec. 5.8.2), the breakup vector analyzing powers were evaluated from linear fits of the above combinations of f^ξ as functions of the sine or cosine of the first proton azimuthal angle φ_1 , respectively. A sample dependency of f^ξ combination from Eq. 5.32 vs. $\cos \varphi_1$ for one configuration is illustrated in Fig. 5.32. In Fig. 5.33 sample results for the two vector analyzing powers, A_x and A_y , are shown for one chosen kinematical configuration. The full sets of the theoretical calculations are also presented. More results are given in Appendix B.

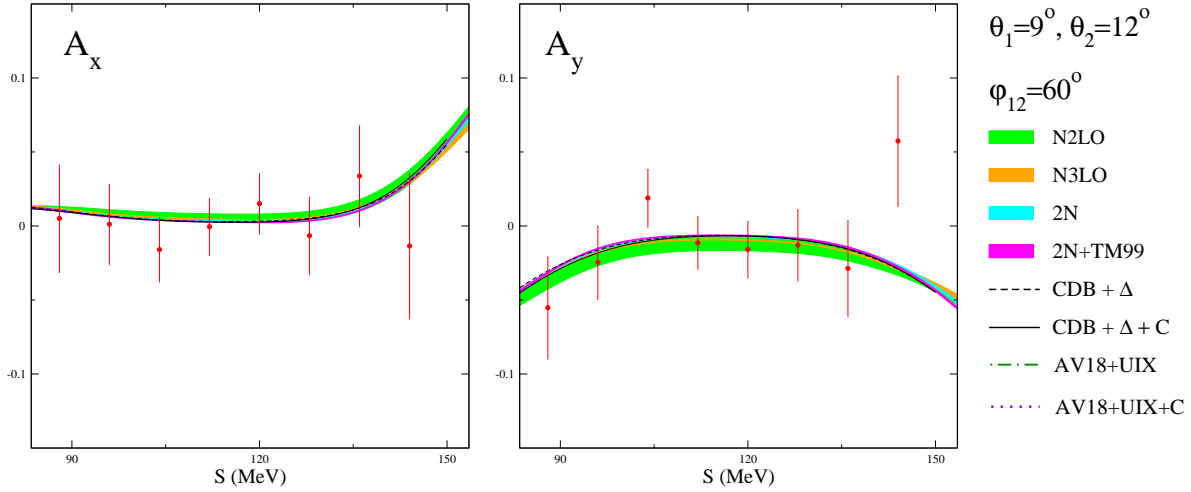


Figure 5.33: Examples of the $d - p$ breakup vector analyzing powers A_x and A_y for one kinematical configuration of the two coincident protons, specified in the legend. Theoretical predictions are shown as bands and lines, as specified in the legend.

5.11 Discussion of possible sources of uncertainties

The observables obtained in the analysis i.e. cross sections and analyzing powers are affected by statistical and systematic uncertainties in a slightly different way. This section contains a brief discussion of the potential sources of the above errors.

5.11.1 Statistical uncertainties

The statistical error of the number n of independent events is in this case given by the Poisson distribution:

$$\Delta n = \sqrt{n}. \quad (5.33)$$

For this experiment the number of collected events n was downscaled by an appropriate factor related to the trigger type (see Sec. 4.3.5). Thus, the real number of events together with its statistical error can be written as:

$$N = n \cdot 2^x, \quad (5.34)$$

$$\Delta N = \sqrt{n} \cdot 2^x = \sqrt{N} \cdot 2^x, \quad (5.35)$$

where 2^x is the downscaling factor, which for the single (elastic) events is equal 4, whereas for the coincident (breakup) ones is equal to 1.

Statistical uncertainties of the measured cross section distributions comprise the error of the measured number of the breakup coincidences, as well as statistical uncertainties of all quantities used in the normalization. These quantities are:

- number of the elastic scattering events,
- efficiencies of the Pizza 1 (obtained from the coincident events) and Pizza 2 detectors (obtained from the elastic events) - see Sec. 5.9.2. The estimated value of the statistical errors are around 2% and 0.1%, respectively,

- values of the elastic scattering cross sections given by Shimizu et al. [42] and used in normalization. The value of this errors is about 1%.

In the case of the vector analyzing powers, the statistical uncertainties have following sources:

- the fit procedure, which are the main contributions. The values vary depending on configuration.
- statistical error of the vector beam polarization P_z , which also contains the statistical error of the experimentally obtained value of the iT_{11} analyzing power of the elastic scattering. The mentioned above values introduced the uncertainties of about 3% and 1% [72], respectively. See Sec. 5.8.2 for more details,
- statistical error of the normalization factor κ . The estimated value of the statistical error is about 0.2%, see also Sec. 5.8.2.

5.11.2 Systematic uncertainties

Influence of the systematic errors was reduced significantly by detailed study of the setup geometry and the detection efficiency. Potential sources of the systematic uncertainties and their influences on the observables are listed below:

1. Luminosity.

The luminosity (total beam current) is different for the polarized I_{pol} and unpolarized I_0 states, what is reflected in the normalization factor $\kappa = \frac{I_{pol}}{I_0}$. It has been checked that its value is stable in time and does not depend on the downscaling factors applied to the triggers. κ is obtained in the analysis as a parameter of the fit (Eq. 5.11) to the elastic scattering data and is directly applicable for the breakup reaction. Normalization to the luminosity is not expected to cause any systematic uncertainty on the analyzing power results.

2. Reconstruction of the particle emission angles.

The errors due to the reconstruction of the particle emission angles θ and φ originate from the finite thickness of the target and size of the beam spot on the target. Moreover, they depend on angular granulation related to the overlapping front and rear spirals of the Quirl detector, what gives 20000 pixels of the size from 0.011 mm² to 0.1 mm² (see Sec. 4.3.4). The determination of the distance between the target and Quirl also influences the accuracy of the angle reconstruction. This kind of uncertainties can affects the results only when the reconstructed angles are shifted from the real ones. The analysis of the elastic scattering events (see Sec. 5.3) allowed for an accurate verification of the measured target-Quirl distance and confirmed that there is no systematic shift of the reconstructed polar angles. In conclusion, the accuracy of determination of the azimuthal angle φ is connected to the number of spirals of the Quirl detector (200 spirals on the both sides) and is given by the formula $\frac{2\pi}{200} \sim 0.0314[\text{rad}] \sim 1.8^\circ$. In case of the solid angle, the accuracy vary from 10^{-6} to 10^{-5} depending on the size of the pixels. Only systematic uncertainties originating from determination of the azimuthal angle φ can affect the analyzing power results and are estimated to be below 1%.

3. Calibration and energy correction procedures.

The errors are related to the determination of the peak centers in the ADC spectra obtained in the calibration run (see Sec. 5.6) for each GeWall detector. Further uncertainties could also originate from the determination of the peak centers, when checking the correctness of the calibration i.e. obtaining the kinematical relations of the deposited energy vs. θ (polar angle) for the elastic scattering events. This procedure provided the scaling factors for the energy losses correction - see Sec. 5.6. The obtained uncertainties of the calibration correction procedure were established to be about 3%. In conclusion, their influence on the breakup cross section distributions is less than 1%.

4. Energy cuts.

Selection of the interesting events (protons and deuterons) is connected with imposing different energy cuts or applying defined gates on the $\Delta E - E$ spectra. Thus, "leaking" of interesting particles to and from the identification ranges can be a source of uncertainties. It has been checked for the identification gate of protons, that slight changing of the defined region borders introduces the uncertainty of at most 1%.

5. Background subtraction.

The background subtraction procedure is used for determination of the vector beam polarization P_z , as well as in normalization of the breakup cross section. In case of the elastic deuterons, the errors originate from the gaussian extrapolation of the background below the elastic peak (see Sec. 5.8.1, Fig. 5.18). For the elastic protons, the linear fit was assumed as the background model and the parameters obtained in this procedure are the sources of uncertainties (see Sec. 5.8.1, Fig. 5.18). Moreover, the limits of integrating of the breakup peak (see Sec. 5.10.1, Fig. 5.30) for separate slices along S, were chosen arbitrarily, what also can cause additional errors. The estimated value of uncertainty originating from the background subtraction procedure is about 1.5%.

6. Efficiencies.

The calculated efficiencies of the detectors are a source of possible errors. The assumed model (with its parameters) for calculating the factors describing the contribution of different effects to the total efficiency causes very significant systematic errors, what affects the cross section distributions in a serious way. In order to estimate their values the calculations were performed for additional two sets of the parameters R_Q (radius of the spot characterizing the charge splitting on the spirals) and R_{P1} (radius of the spot in case of the Pizza 1 sectors) - see Sec. 5.9 for more details. The parameters in this auxiliary calculations were assumed to be $R_Q = 0.22$ mm, $R_{P1} = 0.6$ mm and $R_Q = 0.18$ mm, $R_{P1} = 0.4$ mm. The estimated values of the uncertainty obtained for the relative azimuthal angles between the two protons $\varphi_{12} \geq 120^\circ$ is about 4÷8%. The evaluated values of the systematic errors for $\varphi_{12} < 120^\circ$ are quite large and affect the cross section distributions in a serious way, what is demonstrated in Fig. 5.34. The model of charge distribution over spirals in the Quirl detector does not completely reproduce, crucial for the efficiency analysis, geometrical effects connected with the "overlapping clusters". This simple model needs further developments to be able to produce correction factors in a proper way.

Therefore, the results of the Quirl efficiency resulting from that model are biased with rather large systematic uncertainties, which are estimated to be as large as 60% (for 13 configurations) and 35% (for another 8 configurations). Within the discussed range of $\varphi_{12} < 120^\circ$ only a fraction of geometries is affected, corresponding to the lay out of the spirals. It has been established that the strongest effect is observed for configurations fulfilling the condition $\frac{\varphi_{12}}{|\theta_1 - \theta_2|} = 10$ (60%), and smaller for a few neighbouring geometries with $\varphi_{12} \neq 60^\circ$ and described by the formula $\frac{\varphi_{12}}{\Delta\theta + \text{sign}(\varphi_{12} - 60^\circ) * 2} = 10$, where $\Delta\theta = |\theta_1 - \theta_2|$ (35%), (see Table 5.3).

| $\varphi_{12} [^\circ]$ | $\Delta\theta = \theta_1 - \theta_2 $ | | | | |
|-------------------------|----------------------------------------|-----|-----|-----|-----|
| | 0 | 2 | 4 | 6 | 8 |
| 20 | 60% | 60% | 35% | - | 35% |
| 40 | - | - | 35% | 35% | - |
| 60 | - | - | - | 35% | - |
| 80 | - | - | - | 35% | 60% |
| 100 | - | - | - | - | 35% |

Table 5.3: Systematic uncertainties for configurations very strongly affected by calculations of the detection system efficiencies. For majority of configurations systematic uncertainties due to that effect are around 4-8%.

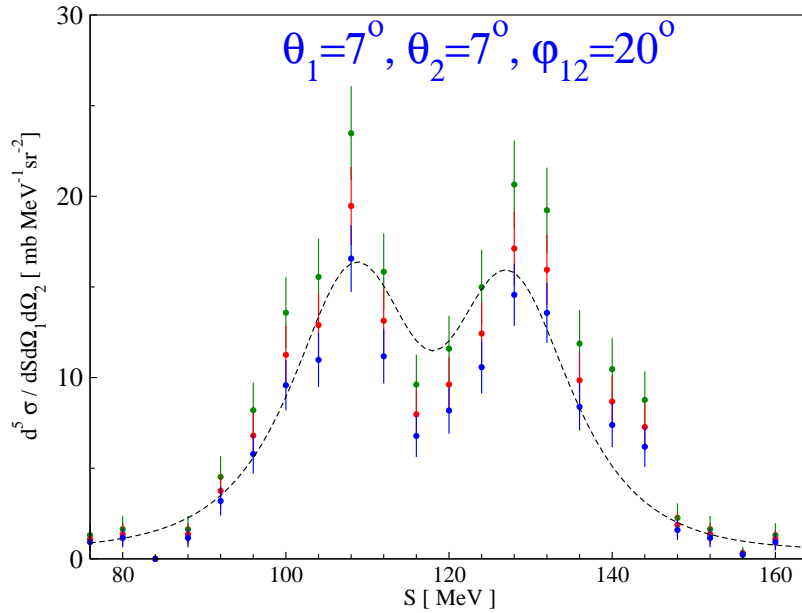


Figure 5.34: Example of the breakup cross section distribution for the configuration characterized by very small value of the relative azimuthal angle $\varphi_{12} = 20^\circ$. The red points are the experimental data obtained with the model parameters $R_Q = 0.2$ mm, $R_{P1} = 0.5$ mm. The blue and green points refer to the same data, but with parameters $R_Q = 0.4$ mm, $R_{P1} = 0.18$ mm and $R_Q = 0.6$ mm, $R_{P1} = 0.22$ mm, respectively. The dashed line represents the cross section calculated on the basis of CDB+ Δ +C potential.

7. Normalization to the elastic scattering.

The breakup cross sections were normalized to the elastic scattering data in order to obtain the absolute values. Thus, the obtained results are affected by the error of 1.6% quoted by Shimizu et al. [42].

In determination of the absolute values of the cross section the most significant systematic uncertainty is due to efficiencies. The other uncertainties discussed above also contribute, but they are much less important. Therefore, the overall systematic error of the breakup cross section for a majority of the studied configurations is established to be 5-10%, depending on the geometry.

Analysis of the polarization observables relies on the determination of rates measured with the polarized and unpolarized beams. Thus, the advantage of this approach is obvious i.e. the experimental factors, which appear in the analysis, like efficiency of the detection system or identification methods (applying different identification cuts in the $\Delta E - E$ spectra), as well as uncertainties connected with determination of solid angles are cancelled. In the ratio given by Eq. 5.28 in Sec. 5.10.3 only corrections connected with the background subtraction play a significant part and are included in denominator of the ratio. The overall value of the systematic errors for A_x and A_y is estimated to be around 1-2%.

Chapter 6

Results

6.1 Experimental results

Experimental results of the cross section values are obtained for 135 kinematical configurations of the two breakup protons. Polar angles θ_1 and θ_2 of the two protons are changing between 5° and 14° with the step of 2° and their relative azimuthal angle φ_{12} is taken in the range from 20° to 180° , with the step of 20° . The experimental results were integrated (see Sec.5.10.3) within the ranges of $\Delta\theta_1 = \Delta\theta_2 = 2^\circ$ and $\Delta\varphi_{12} = 10^\circ$ for each combination of the central values θ_1 , θ_2 and φ_{12} . The bin size along the kinematic curve S was chosen to be 8 MeV.

In the case of vector analyzing powers A_x and A_y , the experimental results were obtained in 24 kinematical configurations for each observable. In the analysis the event integration limits were chosen to be $\Delta\theta_1 = \Delta\theta_2 = 3^\circ$ and $\Delta\varphi_{12}=20^\circ$. The bin size of the S value was 16 MeV.

The choice of event integration limits enabled to reach quite sufficient statistical accuracy enabling comparisons with different theoretical predictions.

Sample results of the cross section and analyzing powers A_x and A_y for chosen kinematical configurations were presented in Sec. 5.10 in Figs. 5.31 and 5.33, together with the full set of the theoretical calculations. The bulk of such individual comparisons for all the evaluated configurations for cross section and vector analyzing powers is collected in Appendix A and Appendix B, respectively.

6.2 Averaging of the theoretical predictions over the integration limits

The chosen angular ranges which define the geometrical configurations of the breakup protons are wide enough to obtain quite good statistical accuracy, however, the obtained results are very sensitive to the averaging effects. Thus, in order to perform reasonable comparisons of the data with the theoretical models, the averaging over the same limits had to be applied to the calculated values of the vector analyzing powers and the cross sections. For that purpose, for each configuration given by the central values of angles θ_1^c , θ_2^c , φ_{12}^c , the analyzing powers and cross section σ_0 values have been calculated for all combinations of angles $\theta_1^c \pm \frac{1}{2}\Delta\theta_1$, $\theta_2^c \pm \frac{1}{2}\Delta\theta_2$, $\varphi_{12}^c \pm \frac{1}{2}\Delta\varphi_{12}$ and the central values, with the step of 1 MeV in variable S. There was, however, one exception for the configurations

defined by the central values of the polar angles of the two protons equal to $\theta_1^c = 13^\circ$, $\theta_2^c = 13^\circ$. Due to the detection system acceptance (the highest available values of the polar angle is 13.5°) the calculations for this geometry were performed within the ranges of the polar angles $\theta_1^c = 13_{-1}^{+0.5^\circ}$, $\theta_2^c = 13_{-1}^{+0.5^\circ}$.

It is important to remember that S is defined individually for each kinematical curve, thus the same values of S for two different combinations of angles are related to two different pairs of proton energies (E_1, E_2).

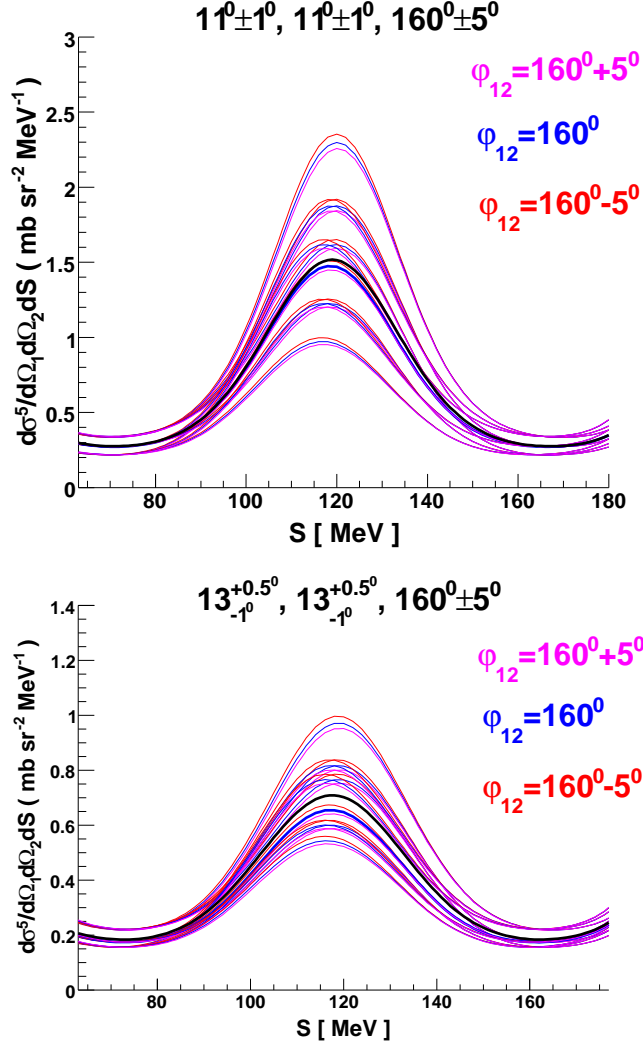


Figure 6.1: Figures present the results of the theoretical calculations with the AV18 NN potential combined with the Urbana IX 3NF and with the Coulomb interaction included (AV18+UIX+C) for two chosen configurations described in the picture. The theoretical curves marked with red, dark blue and magenta colours refer to various combinations of the θ_1 , θ_2 and φ_{12} (specified in the legend) within the integration limits, which were taken into account in the averaging procedure. The thick dark blue lines represent the calculations for the central configurations, whereas the black ones present the final results of the averaging approach. The differences between the thick dark blue lines and the black ones are clearly seen.

Analyzing power values obtained for a given configuration and S were weighted with a product of σ_0 and the solid angle factor, whereas the cross section values were only corrected with the the solid angle factor. Finally, the evaluated data were placed on the E_2 vs. E_1 plane and projected onto the curve corresponding to the relativistic kinematics, calculated for the central geometry $(\theta_1^c, \theta_2^c, \varphi_{12}^c)$. The importance of the averaging procedure is demonstrated in Fig. 6.1.

This approach is similar to the analysis of the experimental data, therefore it assures that averaging of the theoretically calculated vector analyzing powers and cross sections is equivalent to event integration within the ranges accepted in the analysis. The applied procedure also projects the results of non-relativistic calculations onto relativistic kinematics. In this way they can be directly compared to the S distributions of the data, without necessity to correct for difference of arc-lengths calculated along relativistic and non-relativistic kinematic curves.

Moreover, it has been checked that employing of more dense grid of angles for averaging has no influence on the results.

6.3 Comparisons of the results with theory

The obtained cross section values and the vector analyzing power data for the $d-p$ breakup reaction at 130 MeV were compared to the state-of-the-art theoretical calculations, described briefly in Sec. 3. The theoretical predictions were obtained with realistic NN potentials (referred to as 2N), with the NN forces combined with the TM99 3NF (2N+TM99), as well as with the AV18 potential combined with the Urbana IX 3NF (AV18+UIX) and also with the Coulomb interaction included (AV18+UIX+C). In addition calculations within the coupled-channel approach with the CD Bonn + Δ potential (CDB+ Δ) and with the Coulomb force included (CDB+ Δ +C) were also used in comparisons. Moreover, the data were confronted with the prediction based on the ChPT framework at two orders: N2LO and incomplete N3LO.

In the figures the results are presented as bands reflecting the spread of the results of calculations obtained with the following realistic potentials: CD Bonn, AV18, Nijm I and Nijm II. In a similar way the above 2N potentials complemented with the TM99 3NF are presented. The ChPT results are also shown as bands, but in this case width of the band represents theoretical uncertainty estimated along with the calculations. The remaining approaches are shown as lines. A sample set of the obtained cross section values and the analyzing powers were presented in Figs. 5.31 and 5.33, whereas the whole bulk of the evaluated data is displayed in Appendices A and B, respectively.

In order to quantitatively inspect the description of the whole data set provided by various models and to identify regions where some interesting effects or problems exist, the value of χ^2 per degree of freedom have been calculated. This kind of calculations was performed for each observable i.e. A_x , A_y and the cross section, for each type of the theoretical prediction. In case of the theoretical results presented in the figures as bands, the χ^2 values were calculated with respect to the center of the band.

Table 6.1 presents the global χ^2 per degree of freedom for the whole data sets of the differential cross section and of the polarization observables A_x and A_y . These results are also shown graphically in Figs. 6.2 and 6.3.

Based on the above information one can draw some global conclusions concerning the

| THEORY | OBSERVABLE | | |
|------------------|--------------------------------------------|-------|-------|
| | $\frac{d\sigma^5}{d\Omega_1 d\Omega_2 dS}$ | A_x | A_y |
| 2N | 26.0 | 0.75 | 1.57 |
| 2N+TM99 | 26.5 | 0.75 | 1.59 |
| ChPT N2LO | 18.6 | 0.76 | 1.60 |
| ChPT N3LO | 17.0 | 0.75 | 1.55 |
| CDB+ Δ | 18.0 | 0.75 | 1.56 |
| CDB+ Δ +C | 3.0 | 0.74 | 1.55 |
| AV18+UIX | 17.3 | 0.74 | 1.57 |
| AV18+UIX+C | 3.2 | 0.74 | 1.54 |

Table 6.1: Global χ^2 per degree of freedom for the experimental cross section and analyzing powers values with respect to different theoretical predictions. In the case of cross section important are the differences between various model approaches.

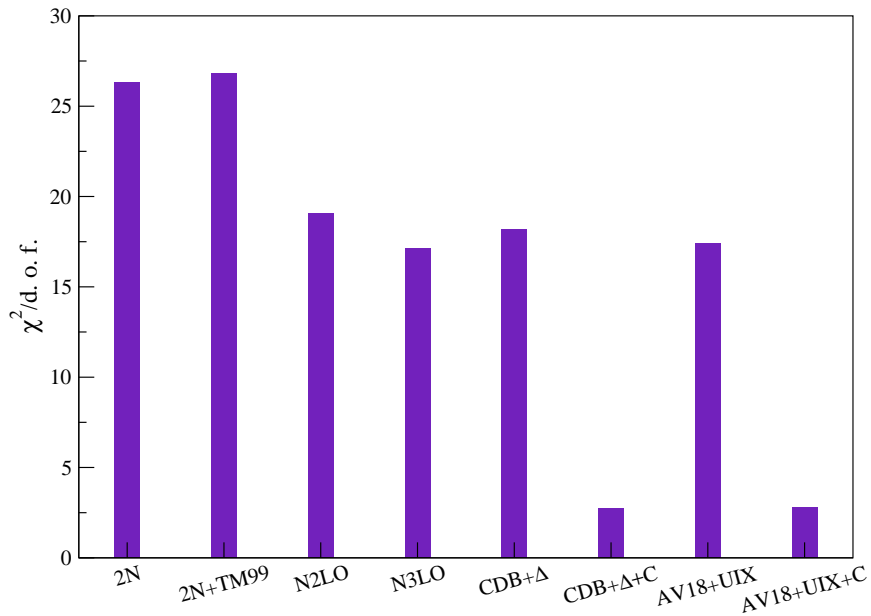


Figure 6.2: Global $\chi^2/\text{d.o.f.}$ for the cross section data with respect to various model predictions presented as histogram. See remark in Tab. 6.1 caption.

theoretical description of the data. In case of A_x , all values of $\chi^2/\text{d.o.f}$ agree with each other and are smallest than 1, what can be due to the overestimated statistical errors. For A_y the obtained values of $\chi^2/\text{d.o.f}$ are higher, around 1.55, independently on the considered theoretical prediction. This fact indicates that the calculational approaches in this case are less successful in describing the data. In general one can conclude that none of the two vector analyzing powers, A_x and A_y , reveal any significant sensitivity to the dynamical effects and that they are quite well reproduced by the state-of-the-art calculations. The calculations predict the small values (in the investigated region) of A_x and A_y correctly over the whole data set and, in contrast to the obtained cross section values, no sensitivity to the Coulomb interaction is visible.

The global features of the cross section data were also investigated. Quality of these data strongly depends on the obtained correction factors related to the efficiencies of

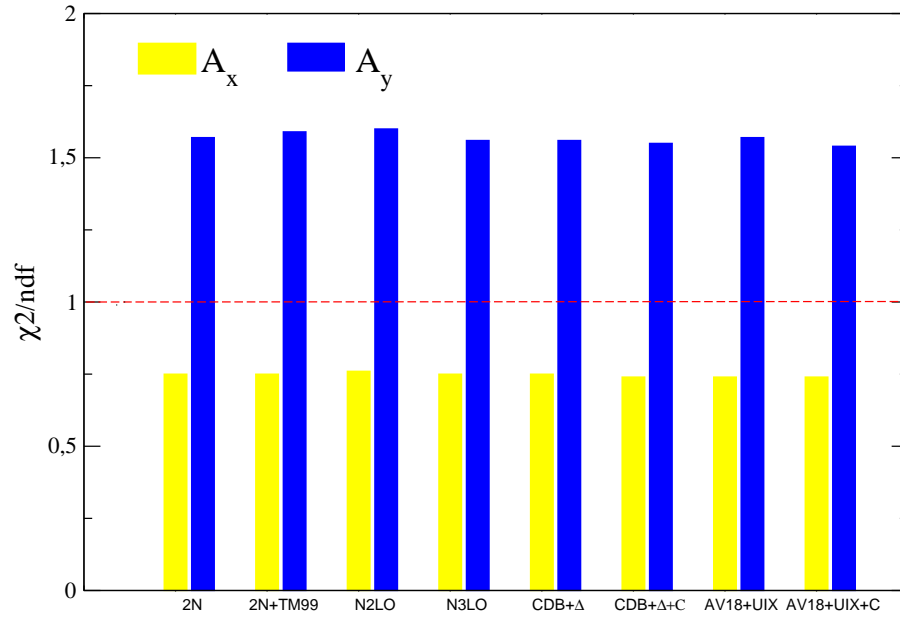


Figure 6.3: Global $\chi^2/\text{d.o.f.}$ results from Table 6.1 presented as histogram and grouped with respect to the type of the theoretical model, with colours differentiating between the A_x and A_y observables.

the detection system. As it was mentioned in Sec. 5.9.1 and discussed in detail in Sec. 5.11, the efficiency analysis provided very high systematic errors, which affect several breakup configurations characterized by rather small values of the relative azimuthal angles $\varphi_{12} < 120^\circ$. Size of this effect depends on the kinematical configuration within the mentioned above range of φ_{12} . The configurations in which the obtained breakup cross sections are biased with the highest systematic uncertainties are listed in Table 6.2. The systematic errors connected with these particular configurations are presented in Sec. 5.11, in Table 5.3.

In the $\chi^2/\text{d.o.f.}$ analysis the experimental points belonging to the “unreliable” configurations were biased with their systematic uncertainties instead of the statistical ones. The obtained global value of $\chi^2/\text{d.o.f.}$ with respect to the theories with the Coulomb interaction included is about 3. The values of $\chi^2/\text{d.o.f.}$ obtained with respect to the theories without Coulomb interaction included are about six (N2LO, N3LO, CDB+ Δ , AV18+UIX) and nine (2N, 2N+TM99) times larger than for the calculations based on the CDB+ Δ +C, AV18+UIX+C potentials.

| φ_{12} [$^\circ$] | $\Delta\theta = \theta_1 - \theta_2$ [$^\circ$] | | | | |
|-----------------------------|---------------------------------------------------|-----------------------|-----------------|------------|------|
| | 0 | 2 | 4 | 6 | 8 |
| 20 | 7/7, 9/9, 11/11 | 5/7, 7/9, 9/11, 11/13 | 5/9, 7/11, 9/13 | | 5/13 |
| 40 | | | 5/9, 7/11, 9/13 | 5/11, 7/13 | |
| 60 | | | | 5/11, 7/13 | |
| 80 | | | | 5/11, 7/13 | 5/13 |
| 100 | | | | | 5/13 |

Table 6.2: The configurations very strongly affected by calculations of the detection system efficiencies. The table lists pairs of θ_1/θ_2 angles (in degrees).

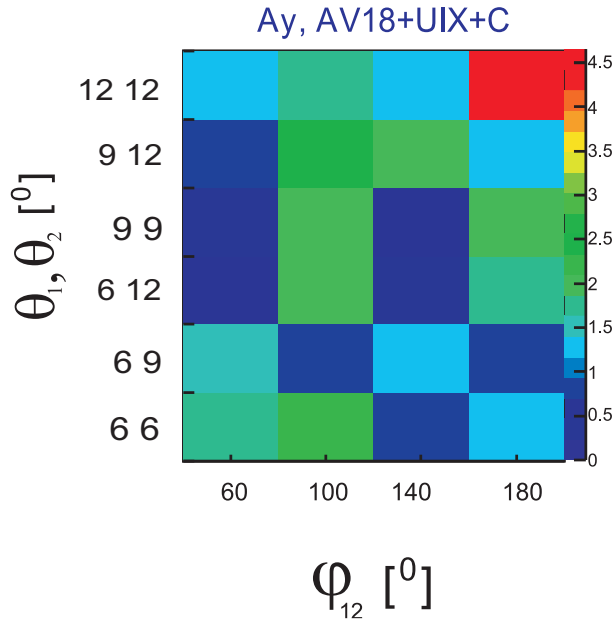


Figure 6.4: Example of a map of $\chi^2/\text{d.o.f}$ values, calculated for the measured distributions of the vector analyzing power A_y compared to predictions of the AV18+UIX+C. Cells of the map refer to individual configurations defined by combination of angles given on the axes. The same convention is in force for the calculated $\chi^2/\text{d.o.f}$ values of the cross sections but on a grid used in that case.

In conclusion, only the theories with implemented electromagnetic interaction reproduce the experimental data of the cross sections in a reasonable way. Moreover, the obtained results of $\chi^2/\text{d.o.f.}$ for 2N potentials and for the AV18+UIX predictions can indicate the importance of the 3NF for the description of the data. In contrary to the analyzing power results, here the dynamical effects are significant.

These global features can be investigated more carefully with the use of the maps of $\chi^2/\text{d.o.f}$ values, which were calculated for each individual geometrical configuration of the two outgoing protons. An example of such a map is shown in Fig. 6.4. The obtained values of $\chi^2/\text{d.o.f}$ for all configurations are plotted on the θ_1, θ_2 (polar angles of the two protons) vs. φ_{12} (the relative azimuthal angle) plane as colour boxes. Colour of each individual box is related to the $\chi^2/\text{d.o.f}$ value for the whole distribution of the scrutinized observable (summed along S), calculated with respect to a particular theory. The full set of such maps for cross sections and polarization observables is presented in the next two subsections.

6.3.1 The vector analyzing powers - individual configurations

Figs. 6.5 and 6.6 present the full set of the obtained $\chi^2/\text{d.o.f}$ values for each individual configuration. Based on this maps few conclusions can be drawn. A quite good description of the vector analyzing power A_x data is confirmed in practically the full studied range of the phase-space, except two configurations with the uncommonly high value of the $\chi^2/\text{d.o.f.}$, close to 1.4 for each considered theory. In the case of the vector analyzing power A_y one can notice that in the majority of the configurations value of the $\chi^2/\text{d.o.f.}$ is higher than 1, what is true for all used calculations.

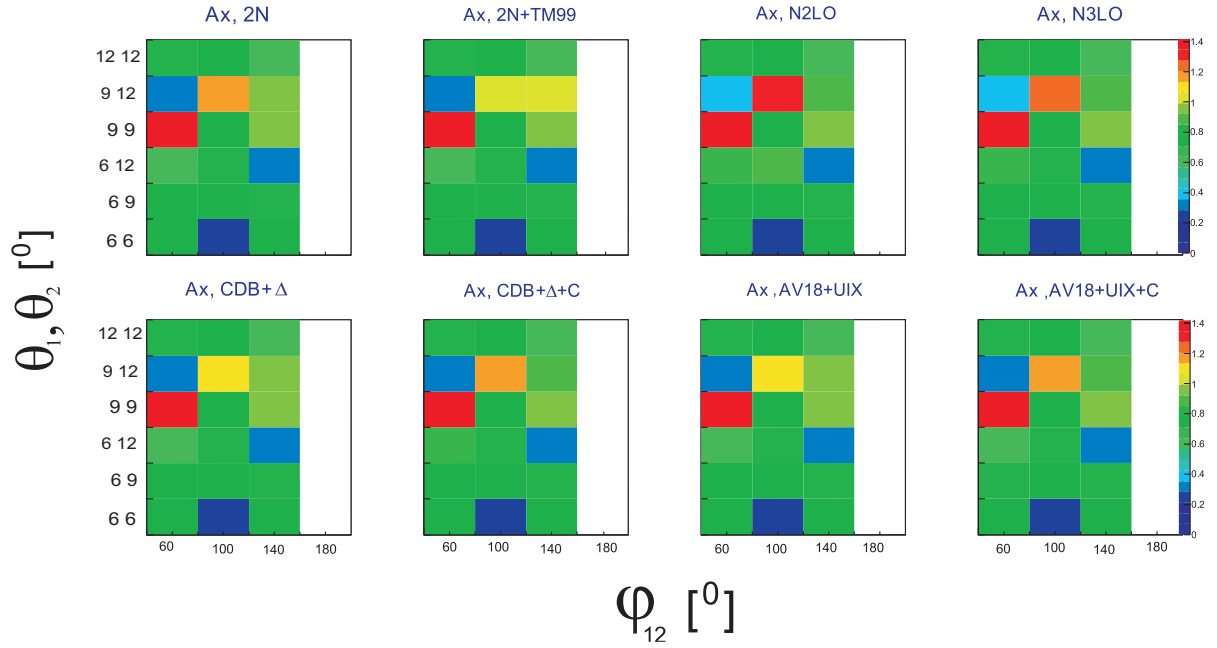


Figure 6.5: Set of $\chi^2/\text{d.o.f.}$ maps, analogical to the example presented in Fig. 6.4, obtained for vector analyzing powers A_x compared to various theoretical predictions. A_x for $\varphi_{12} = 180^\circ$ is required (parity constraints) to be zero.

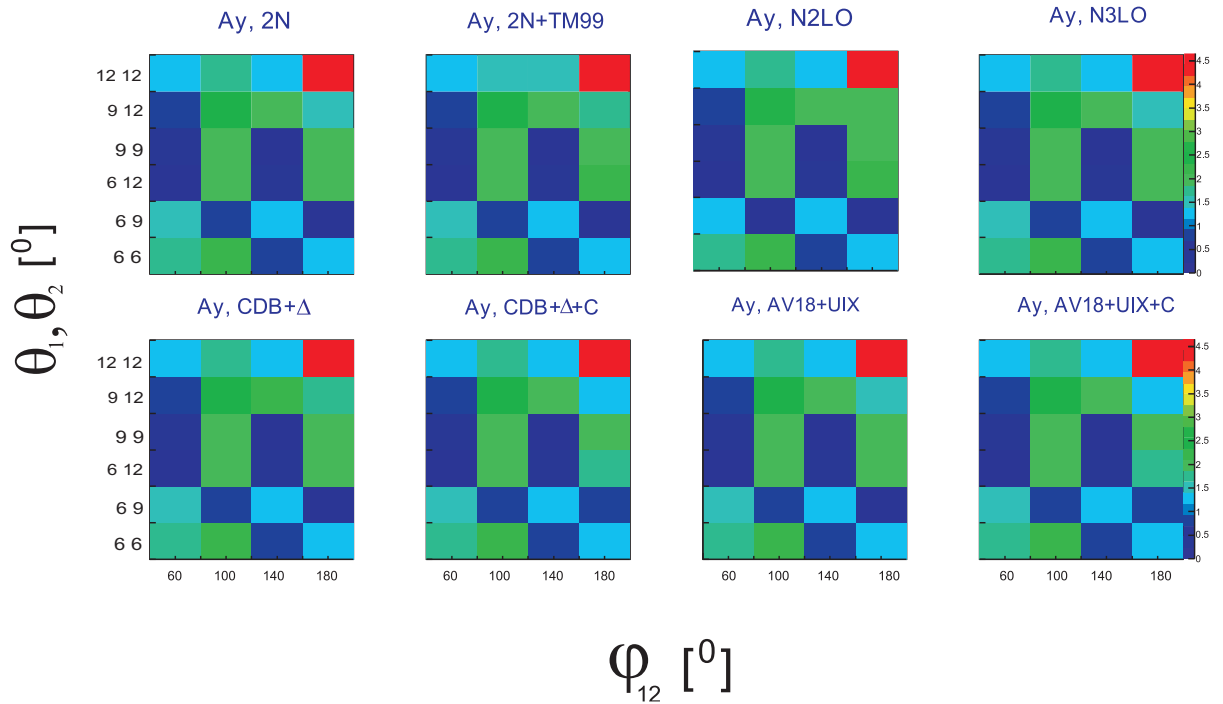


Figure 6.6: Set of $\chi^2/\text{d.o.f.}$ maps, analogical to the example presented in Fig. 6.4, obtained for vector analyzing powers A_y compared to various theoretical predictions.

Nevertheless, there are certain configurations with the $\chi^2/\text{d.o.f.}$ smaller than 1, and only one with extremely high value of the $\chi^2/\text{d.o.f.}$ close to 4.5, what is observed for all theoretical predictions. One can conclude that there is evidently a problem with the description of A_y by the presently available theoretical approaches. The obtained values of the A_x and A_y analyzing powers are very small and as it was mentioned above, they do not reveal any sensitivity to neither the 3NF nor Coulomb effects in the studied part of the phase-space.

Apart from the studies of the global χ^2 and examinations of the individual kinematical configurations, the analysis with respect to other kinematical variables was performed. For that purpose the variables were chosen to be: the energy of the relative motion of the two protons E_{12} , relative azimuthal angle φ_{12} of the breakup protons, pair of the polar angles of the two protons θ_1, θ_2 .

In the first case (Fig. 6.7) the $\chi^2/\text{d.o.f.}$ values were calculated for all experimental points grouped with respect to the energy of the relative motion of the two protons. The results obtained for A_x presented in Fig. 6.7 are distributed randomly with respect to the $\chi^2/\text{d.o.f.}$ values, which are smaller than 1 for the majority of the data points. There is no significant differences observed between the used for comparisons theoretical predictions. In the case of A_y the majority of the points have $\chi^2/\text{d.o.f.}$ around 1.5. At the highest E_{12} values some systematic increase of the $\chi^2/\text{d.o.f.}$ values can be observed, what can be a hint to certain dynamical origin, missing in the theories.

The data sorted according to the φ_{12} values are presented in Fig. 6.8. The results are quite consistent with each other considering various theoretical predictions for both observables. For A_y the distribution is rather random, whereas for A_x the experimental points agree with each other.

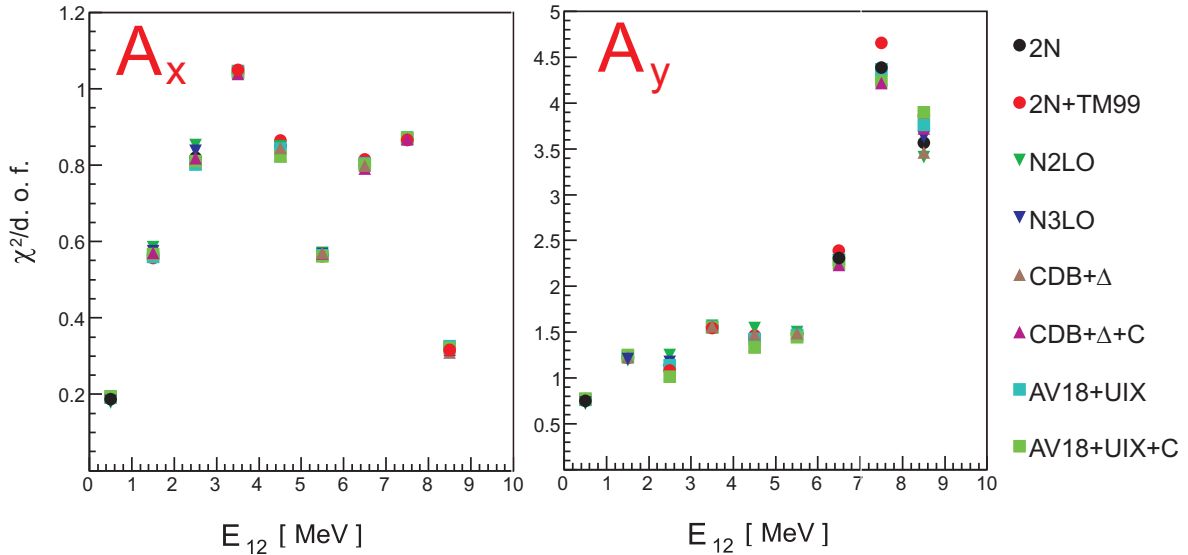


Figure 6.7: Quality of description of the vector analyzing power data with various theoretical predictions (defined in the legend), expressed as dependence of $\chi^2/\text{d.o.f.}$ on the relative energy of the two breakup protons.

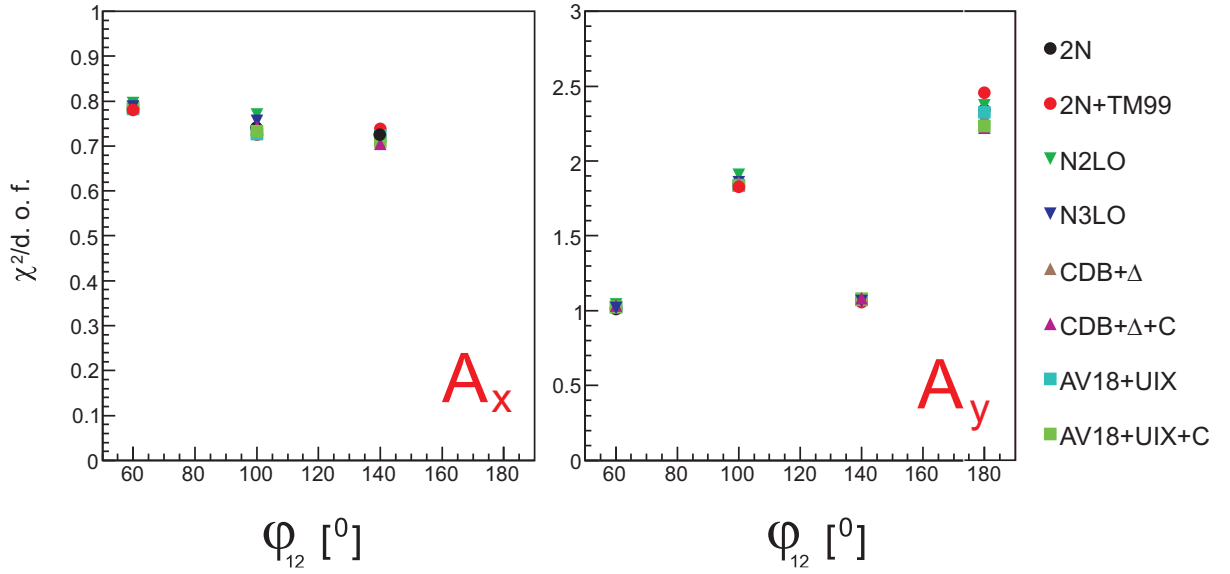


Figure 6.8: Quality of description of the vector analyzing power data with various theoretical predictions (defined in the legend), expressed as dependence of $\chi^2/\text{d.o.f.}$ on the relative azimuthal angle φ_{12} of the two breakup protons.

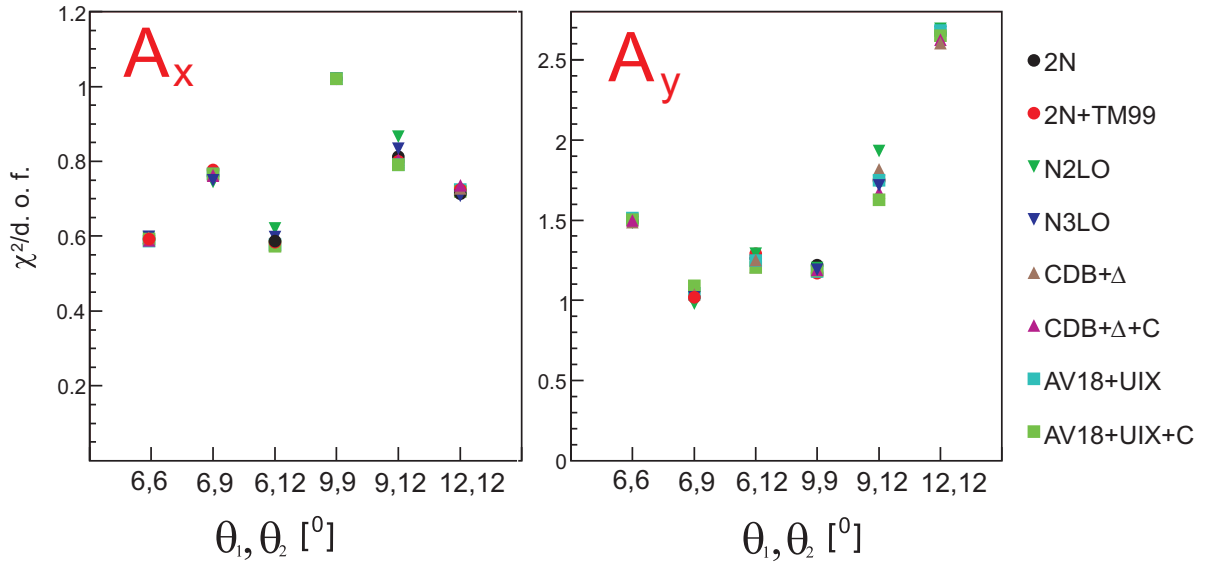


Figure 6.9: Quality of description of the vector analyzing power data with various theoretical predictions (defined in the legend), expressed as dependence of $\chi^2/\text{d.o.f.}$ on combination of the proton emission polar angles.

Examining the distributions shown in Fig. 6.9 one can notice that various theoretical approaches agree with each other, except the one point described with $\theta_1 = 90^\circ$, $\theta_2 = 90^\circ$. Here also random pattern of $\chi^2/\text{d.o.f.}$ distributions is observed.

In conclusion, the investigated region of the phase-space does not reveal any interesting effects connected with the 3N dynamics and in general the data confirm all theoretical models.

6.3.2 The cross section values - individual configurations

The conclusion of the importance of the Coulomb force for the description of the experimental data is also confirmed when studying $\chi^2/\text{d.o.f.}$ for the individual configurations. Such results are presented in Fig. 6.3.2. As one can notice, the smallest values of $\chi^2/\text{d.o.f.}$ are obtained when the data are compared with the CDB+ Δ +C and AV18+UIX+C approaches and, in general, the same pattern is observed for both of the predictions. However, there exist configurations with quite large values of $\chi^2/\text{d.o.f.}$, which appear for the $\varphi_{12} \leq 120^\circ$ and can indicate indigences in the model providing the efficiency correction factors for the cross section data. In the map one can also observe areas characterized by the values of $\chi^2/\text{d.o.f.} \leq 2$, which are present in all panels related to different theories. In these particular configurations different theoretical predictions agree with each other and do not reveal sensitivity to any dynamical effect. In case of the calculations which do not take into account the Coulomb force the obtained values of $\chi^2/\text{d.o.f.}$ are generally very high and can even achieve values of $\chi^2/\text{d.o.f.} \approx 300$. This fact confirms that these models fail to reproduce the experimental data in the majority of the investigated configurations, what is reflected in the pattern of the maps related to these theories.

Importance of the Coulomb force for proper description of the experimental data also demonstrates itself in the analysis with respect to the kinematical variables like relative azimuthal angle φ_{12} of the breakup protons, pair of the polar angles of the two protons θ_1 , θ_2 and the energy of the relative motion of the two protons E_{12} . These dependencies are presented in Figs. 6.11 - 6.13. In the first case (see Fig. 6.11) the obtained values of $\chi^2/\text{d.o.f.}$ for Coulomb-containing predictions are between 2 and 4. One can observe that for $\varphi_{12} = 80^\circ$ the inclusion of the electromagnetic interaction almost does not change the cross sections. In case of the rest of the theoretical predictions one can distinguish two groups (2N, 2N+TM99, N2LO and CDB+ Δ , AV18+UIX, N3LO), which provide slightly different, but generally large values of $\chi^2/\text{d.o.f.}$ Better description is obtained for the models of the second group. Moreover, quite significant 3NF effects are also visible when comparing the red and black circles (about 10%), as well as the cyan squares and black circles.

The obtained dependency of $\chi^2/\text{d.o.f.}$ on different combinations of θ_1, θ_2 (see Fig. 6.12) can provide some interesting conclusion. With increasing $\Delta\theta = |\theta_1 - \theta_2|$ value the Coulomb effects play less important part in reproducing the experimental data and for high $\Delta\theta$ all the theories predict almost the same values of the cross sections.

The results obtained for calculations with respect to the energy of the relative motion of the two protons E_{12} (see Fig. 6.13) stay in agreement with the previous conclusions. In the case of small values of E_{12} the Coulomb effects are extremely high and disagreement between the experimental data and theoretical predictions decreases with the increasing relative energy. For very large $E_{12} \geq 5.5$ MeV the discrepancies are still present, but become much smaller. This range of E_{12} corresponds to a quick separation of the two

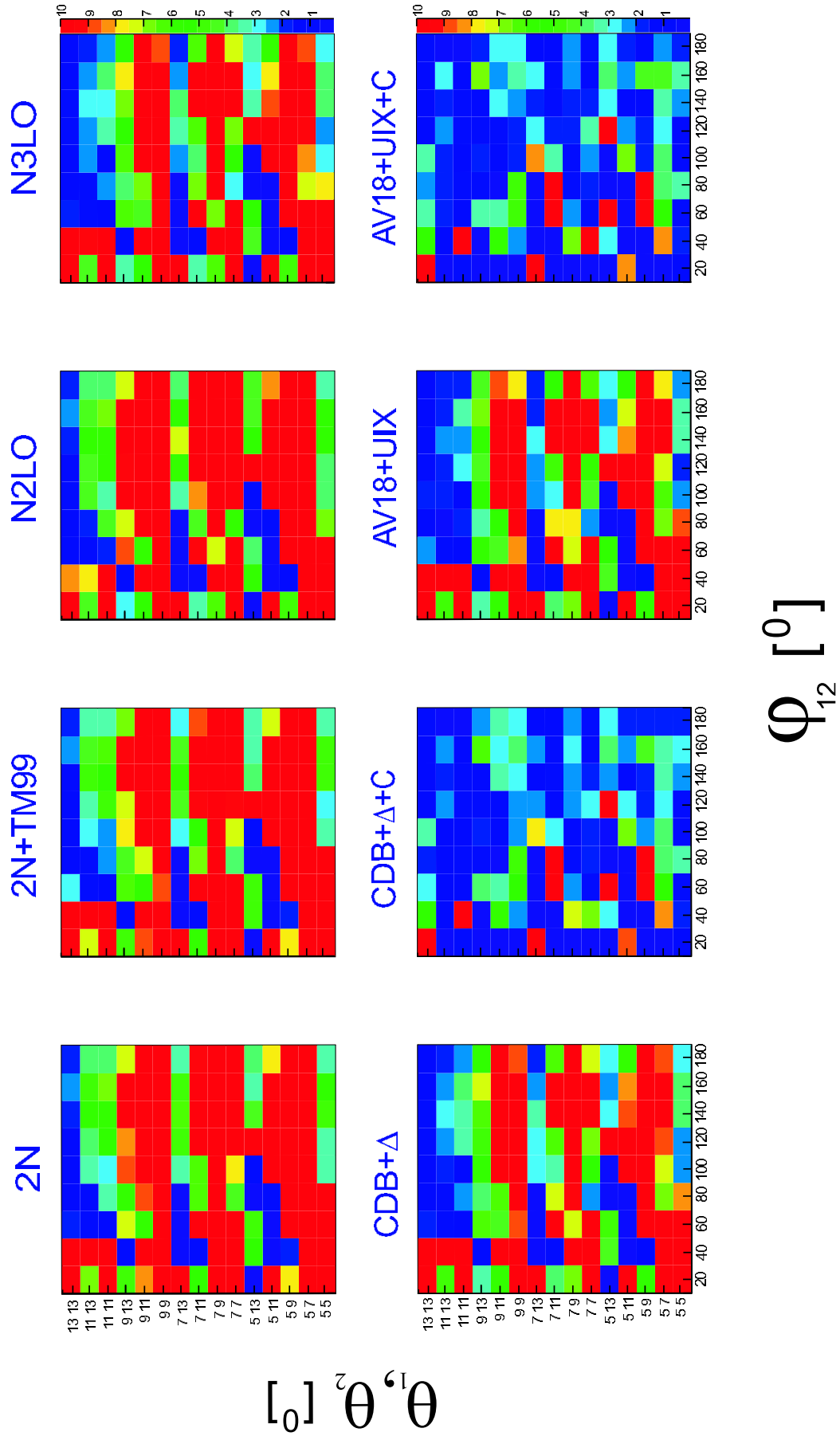


Figure 6.10: Set of $\chi^2/\text{d.o.f.}$ maps, analogous to the example presented in Fig.6.4, obtained for the differential cross sections and compared to various theoretical predictions.

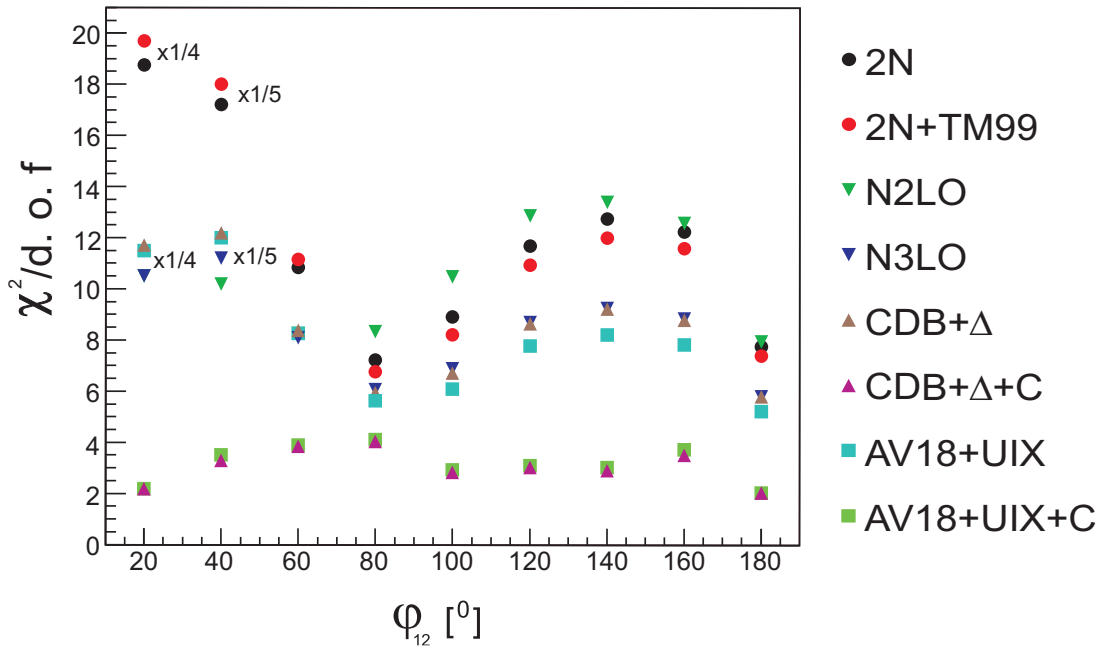


Figure 6.11: Quality of description of the cross section data with various theoretical predictions (defined in the legend), expressed as dependence of $\chi^2/\text{d.o.f.}$ on the relative azimuthal angle φ_{12} . Points with very large $\chi^2/\text{d.o.f.}$ values are scaled down by factors indicated in the panels.

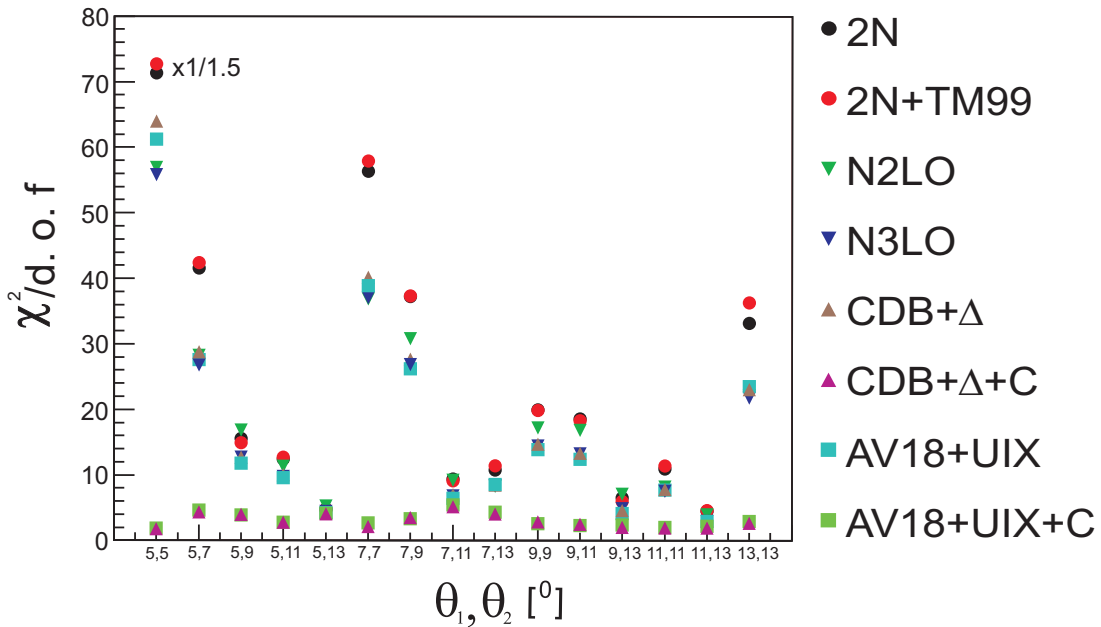


Figure 6.12: Quality of description of the cross section data with various theoretical predictions (defined in the legend), expressed as dependence of $\chi^2/\text{d.o.f.}$ on the combination of the proton emission polar angles. Points with very large $\chi^2/\text{d.o.f.}$ values are scaled down by factors indicated in the panels.

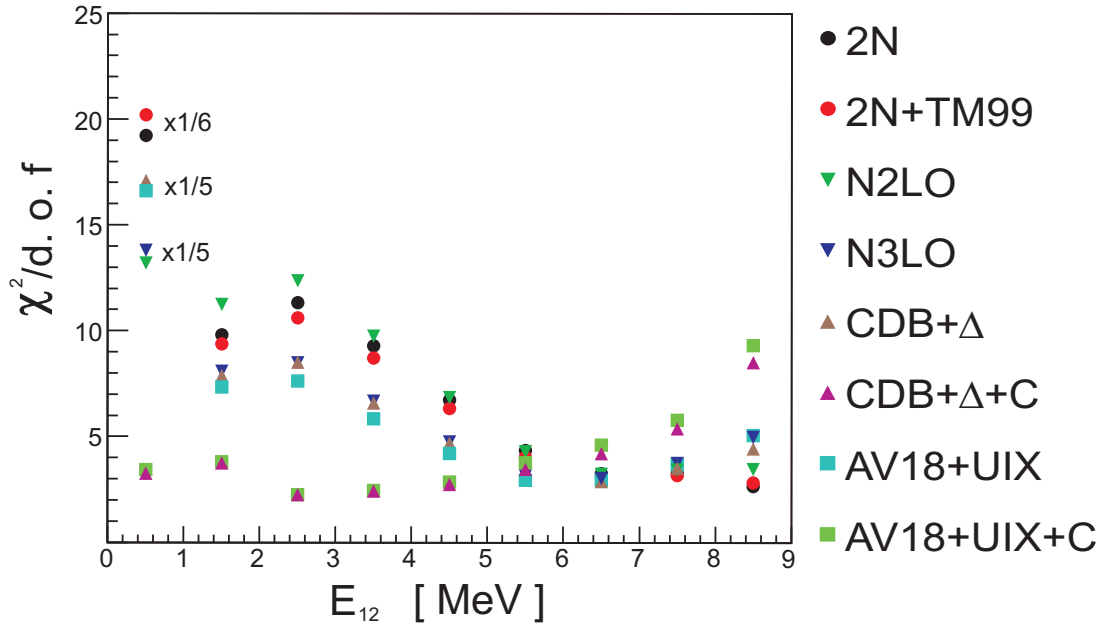


Figure 6.13: Quality of description of the cross section data with various theoretical predictions (defined in the legend), expressed as dependence of $\chi^2/\text{d.o.f.}$ on the relative energy of the two breakup protons E_{12} . Points with very large $\chi^2/\text{d.o.f.}$ values are scaled down by factors indicated in the panels.

protons, and therefore is less sensitive to the electromagnetic interaction.

In general, one can conclude that the Coulomb force is a very important ingredient in the 3N system dynamics. The inclusion of the electromagnetic interaction in the theories which model the 3N system properties dramatically changes the quality of the data descriptions.

Chapter 7

Summary and conclusions

The goal of this dissertation was the experimental investigation of the ${}^1H(\vec{d}, pp)n$ breakup reaction at 130 MeV in the forward angular region. The measurement was performed on one of the external beam lines of the COSY accelerator in the Research Center Jülich. The Germanium Wall detection system used in this experiment covered a very narrow range of the forward angles for the breakup process. As the result of the data analysis the vector analyzing powers A_x and A_y , as well as the differential cross sections $\frac{d\sigma^5}{d\Omega_1 d\Omega_2 dS}$ of the investigated reaction have been obtained. The vector analyzing powers have been evaluated for 42 kinematical configurations resulting in about 300 data points. The values of cross sections have been analyzed for 145 kinematical configurations, what forms a data base of about 2700 data points. In addition, as a byproduct of the beam polarization studies, angular distributions for the iT_{11} analyzing power of the $d - p$ elastic scattering process at the same energy have been obtained. These results complemented the existing data base in the angular area not covered by other experiments.

The results have been compared to the theoretical predictions which model the nuclear dynamics in various ways. They comprise approaches based on the purely realistic NN (CD Bonn, AV18, Nijm I, Nijm II) potentials and combining them with the TM99 3NF and Urbana IX models. Moreover, the data are confronted with the calculations of the coupled-channel approach obtained with the CD Bonn + Δ potential and the similar predictions but including the Coulomb interaction. Finally, they are compared to the results obtained within the ChPT framework at N2LO including full dynamics and, currently not complete, at N3LO.

For the vector analyzing powers all the theoretical predictions agree with each other and do not reveal any sensitivity to the dynamical effects like 3NF or Coulomb interaction. In the case of A_x the theoretical models quite well describe the experimental data, whereas they fail to reproduce A_y equally well.

From the theoretical point of view, the situation is totally different for the predicted values of the differential cross sections in the context of the Coulomb force. Only the models with the Coulomb interaction included (i.e. CD Bonn+ Δ +C, AV18+UIX+C) not only stay in good agreement with each other, but also reproduce the evaluated data in a consistent way. These general conclusions can be drawn already for the configurations described with $\varphi_{12} \geq 120^\circ$. The most sensitive region of the phase-space characterized by the geometries with very small relative azimuthal angles φ_{12} turned out to be very challenging for investigations of such effects. The assumed model which provides correction factors of the detection system efficiencies to the cross section data, what is crucial in this

analysis, fails to completely reproduce the overlapping clusters effects of the Quirl detector and needs further developments. Fortunately, even in the region $\varphi_{12} < 120^\circ$ there is a large number of configurations which are not much affected by the efficiency corrections and for which absolute values of the cross sections are not biased by large systematic uncertainties. The results obtained in the $\chi^2/\text{d.o.f}$ analysis confirm the necessity of inclusion of the electromagnetic interaction into the calculations in order to assure reasonable agreement between the theoretical conclusions and the experimental data. Influences of the 3NF effects on the cross section data are rather small, but still visible, in the studied region of the phase-space.

Appendix A

Breakup Cross Sections Results

This Appendix contains experimental results of the differential cross sections for the reaction ${}^1\text{H}(\vec{d}, pp)n$ at 130 MeV. The results are obtained for the two protons registered at given θ_1 , θ_2 and φ_{12} angles, with the event integration ranges of $\Delta\theta_1 = \Delta\theta_2 = 2^\circ$ and $\Delta\varphi_{12} = 10^\circ$. The evaluated data are compared with a set of theoretical predictions, presented in the figures as colour bands and lines listed in the included legend. The experimental results and theoretical calculations are presented as a function of the arc-length S along the kinematical curve. In the figures the error bars represent the statistical uncertainties only. Configurations biased with large systematic uncertainties appear in the sets of figures as the ones with red frames.

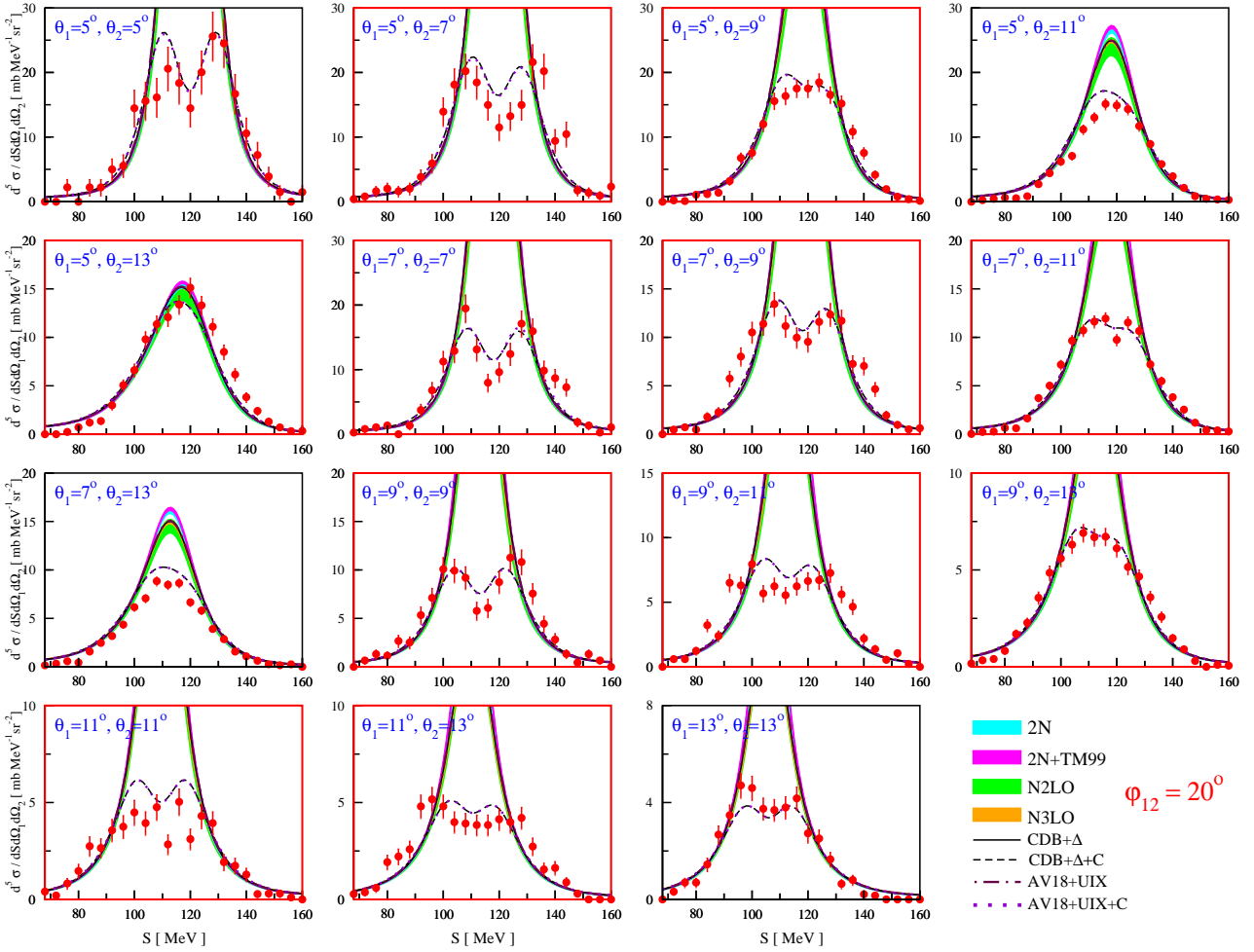


Figure 7.1: The differential breakup cross sections for the same relative azimuthal angle $\varphi_{12} = 20^\circ$. Cyan and magenta bands represent calculations based on realistic potentials (with and without 3NF included, respectively), green and orange - chiral theories (at N2LO and N3LO, respectively), black lines - calculations of the coupled channel approach (solid with and dashed without Coulomb interaction included), dashed maroon line - calculations based on the realistic AV18 potential combined with the Urbana IX 3NF and dotted violet line - the same predictions, but with the Coulomb force implemented.

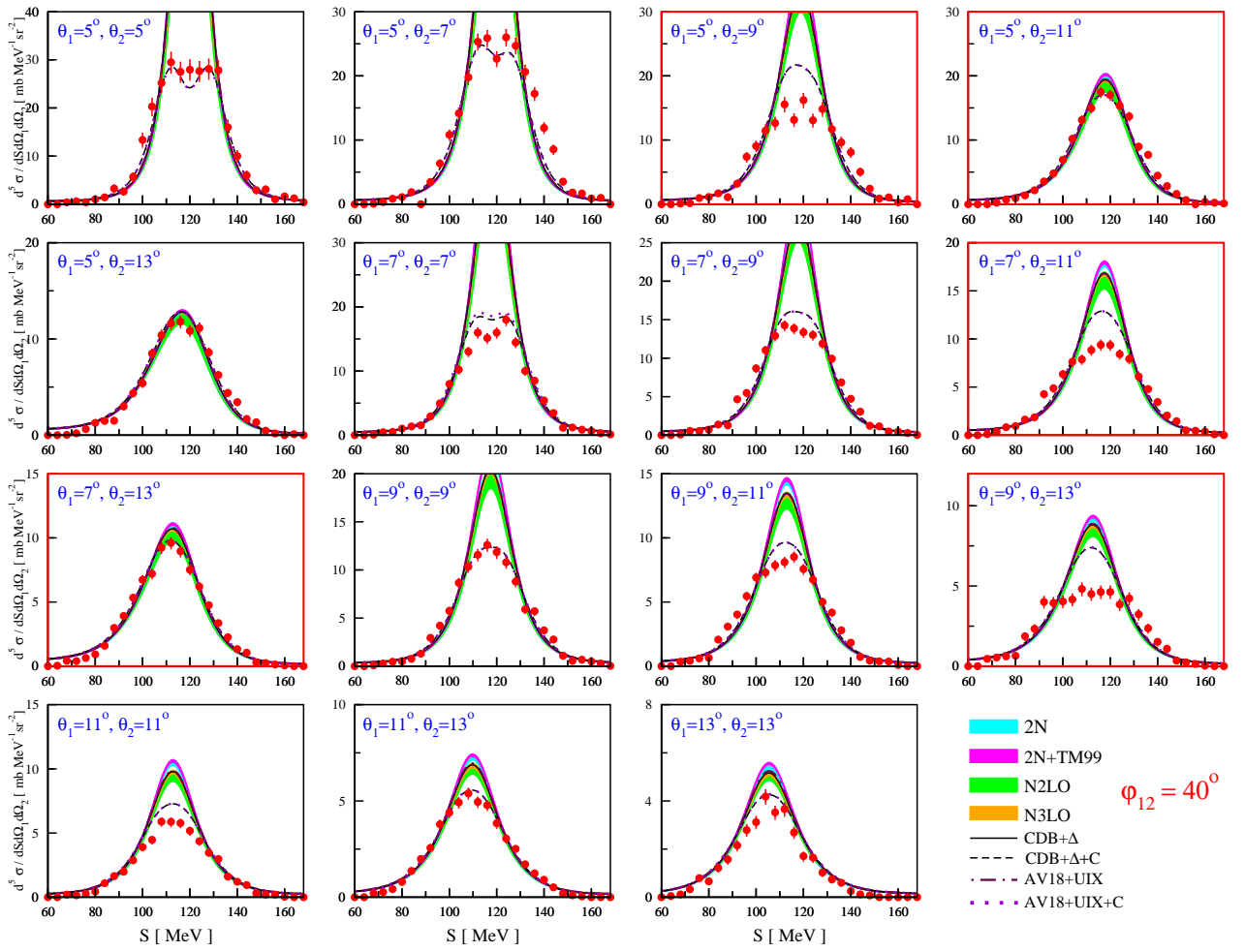
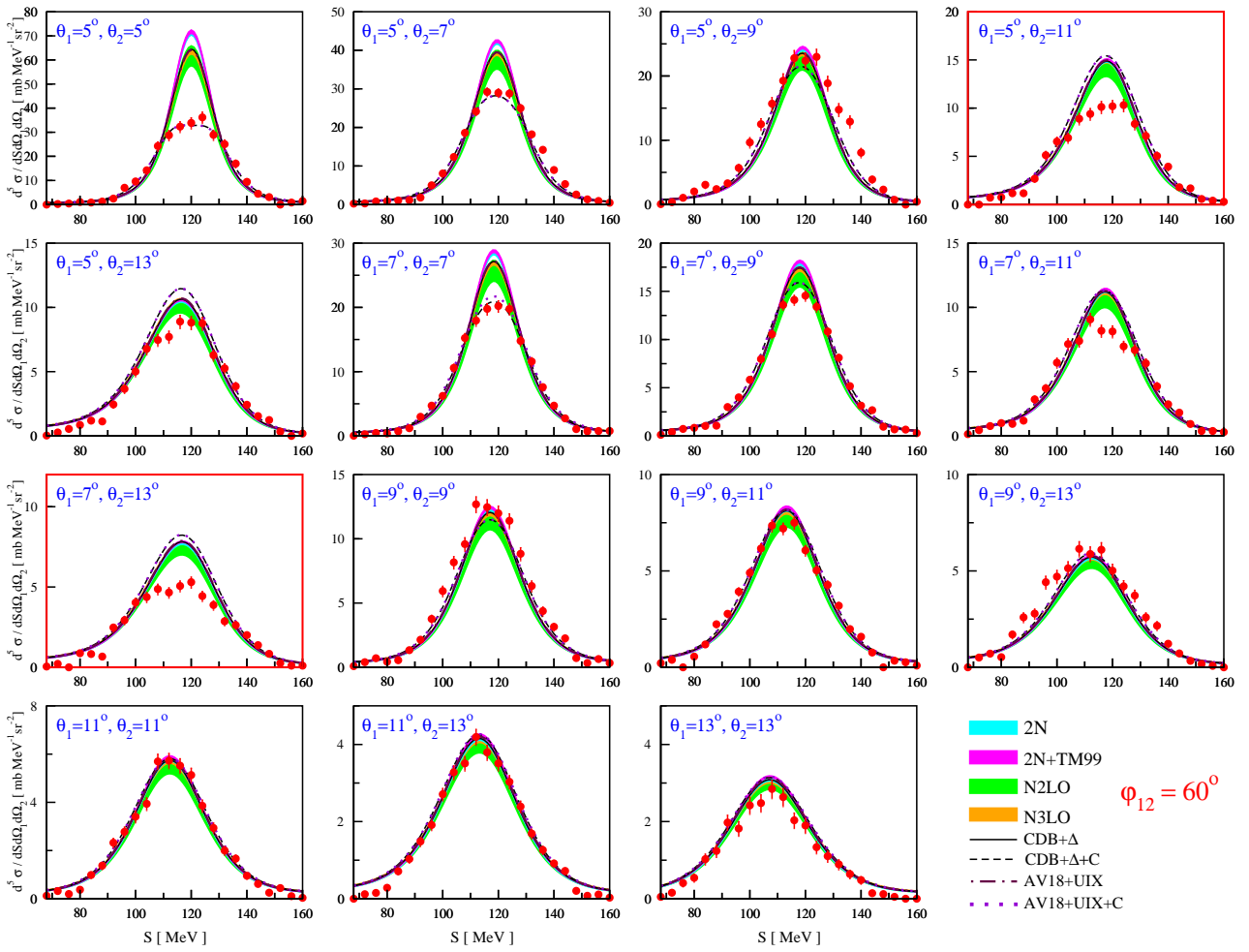


Figure 7.2: Same as in Fig. 7.1, but for $\varphi_{12} = 40^\circ$.

Figure 7.3: Same as in Fig. 7.1, but for $\varphi_{12} = 60^\circ$.

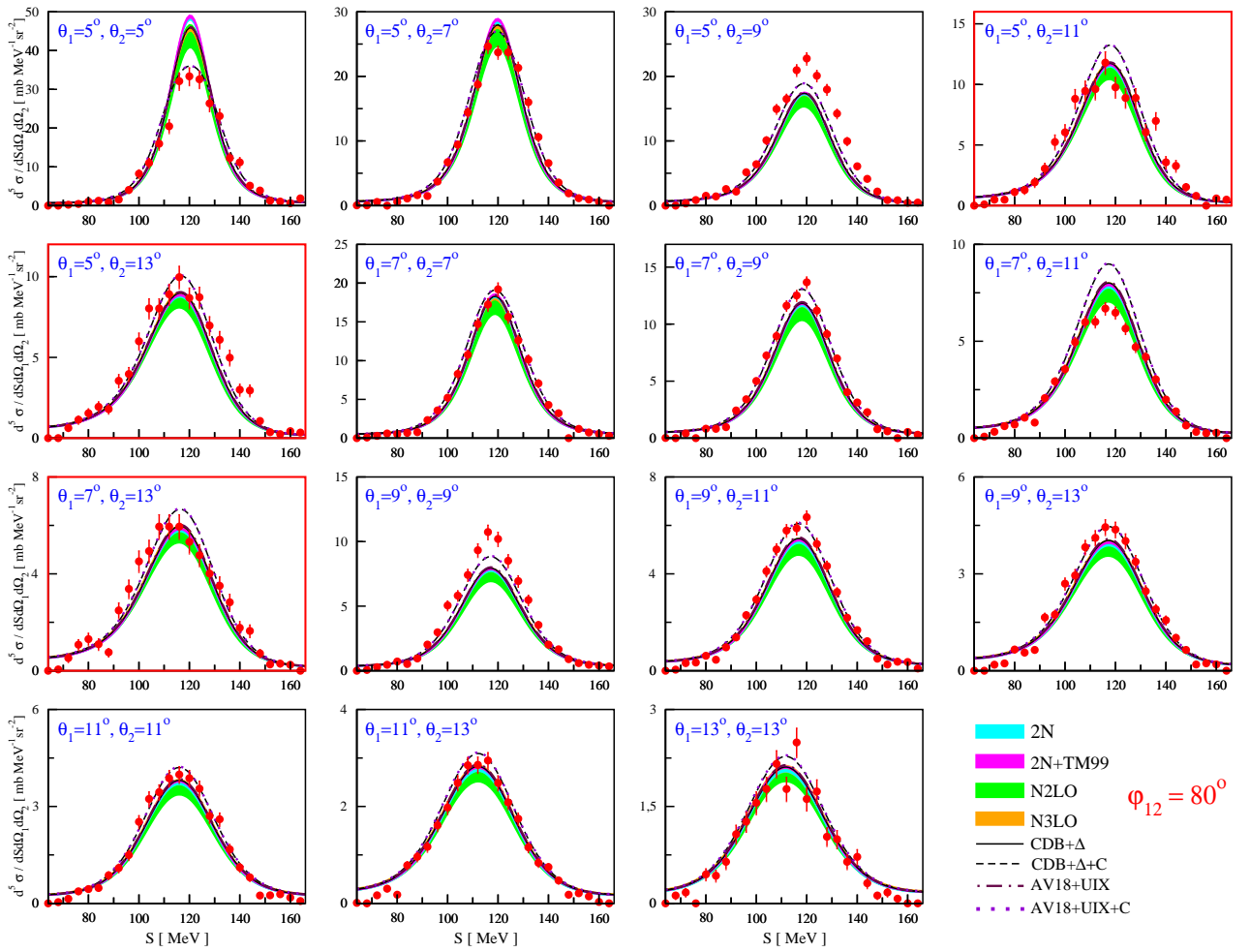


Figure 7.4: Same as in Fig. 7.1, but for $\varphi_{12} = 80^\circ$.

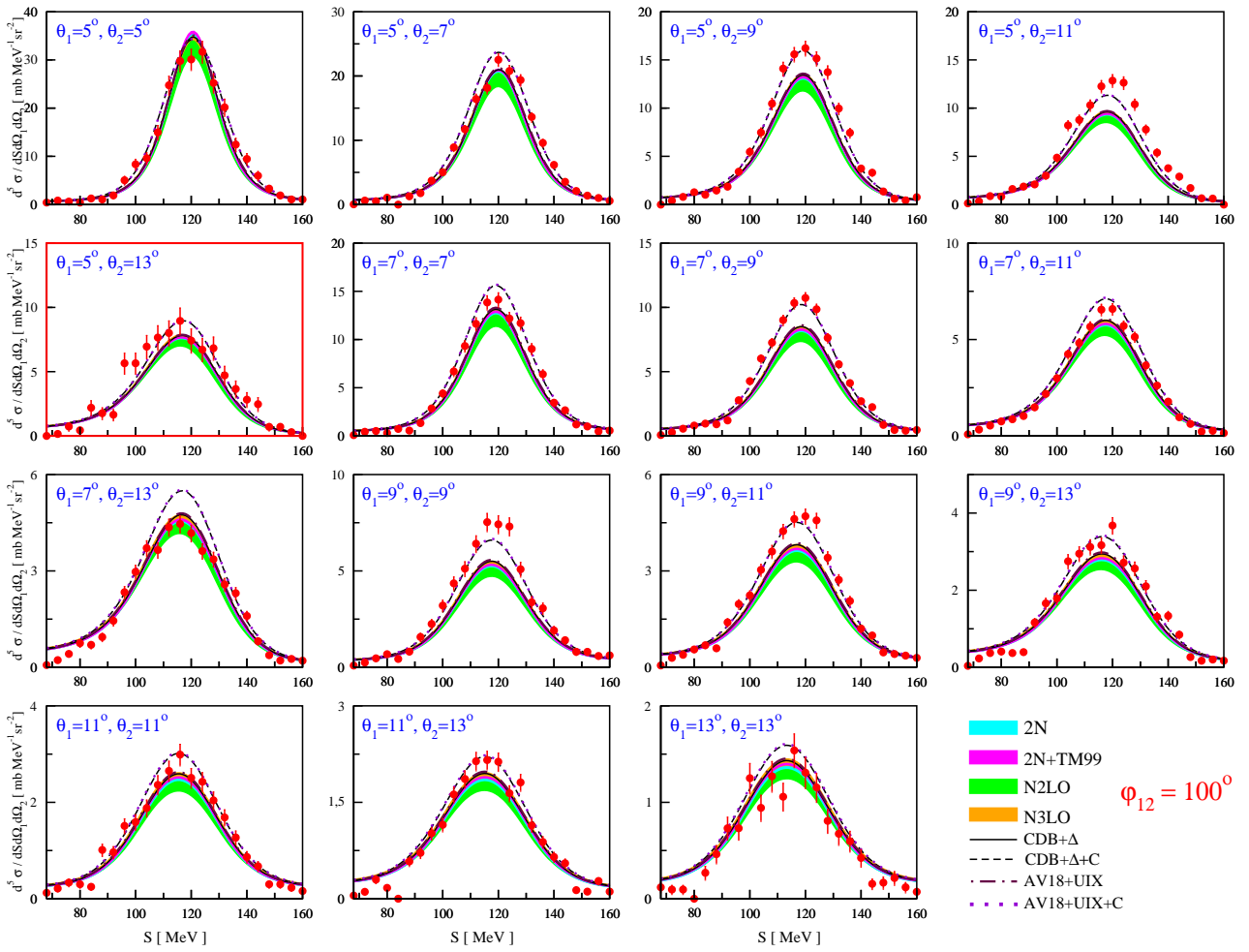


Figure 7.5: Same as in Fig. 7.1, but for $\varphi_{12} = 100^\circ$.

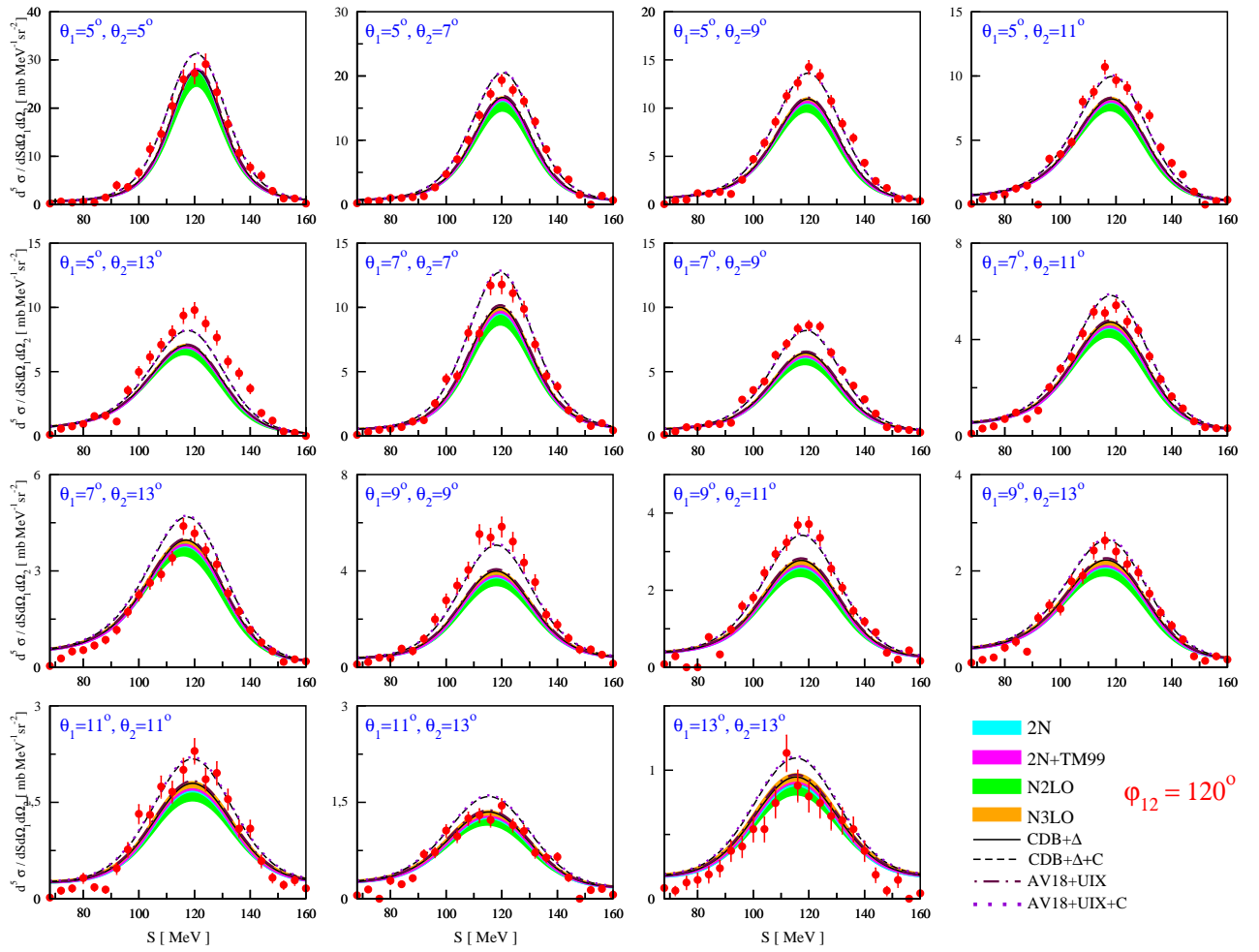


Figure 7.6: Same as in Fig. 7.1, but for $\varphi_{12} = 120^\circ$.

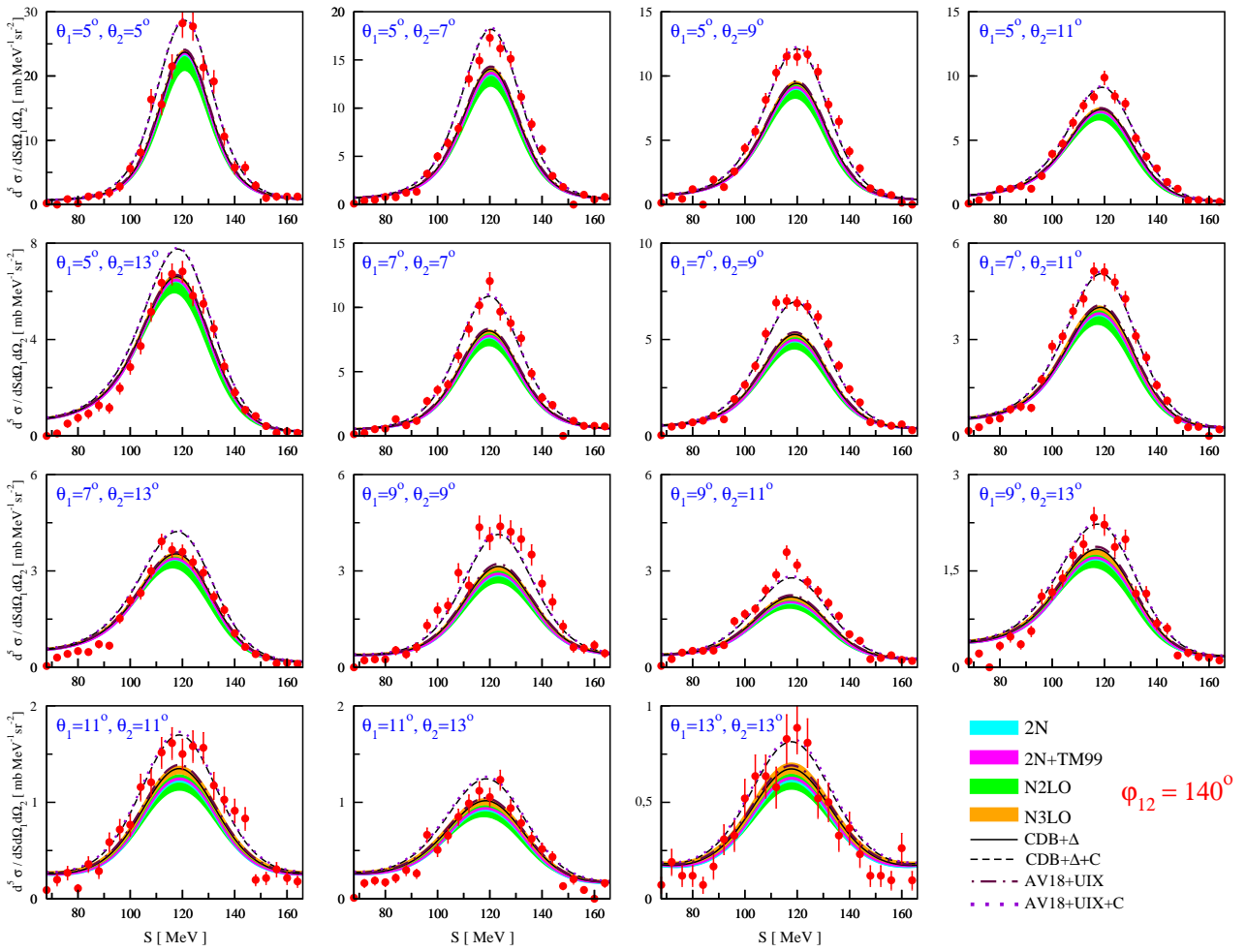


Figure 7.7: Same as in Fig. 7.1, but for $\varphi_{12} = 140^\circ$.

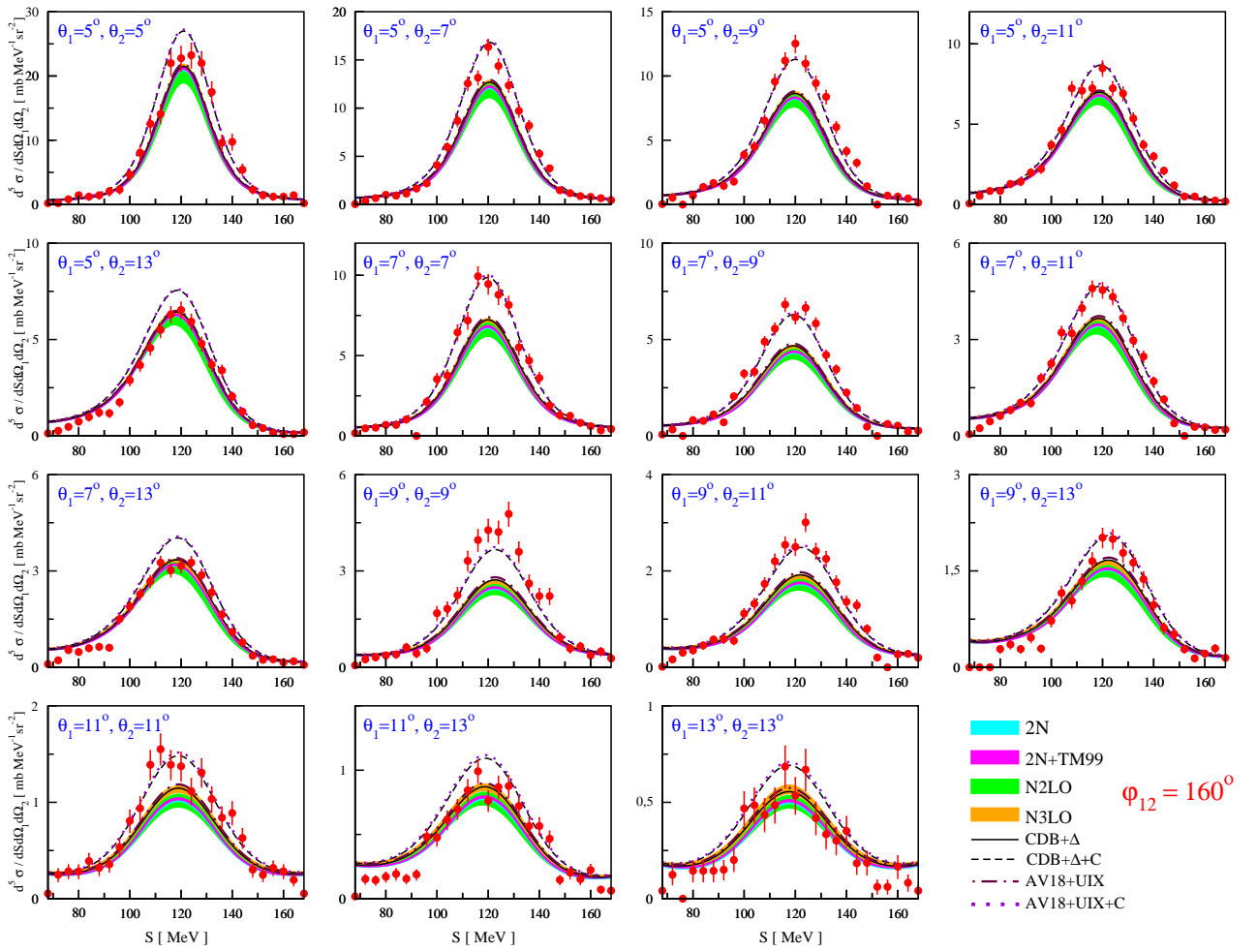


Figure 7.8: Same as in Fig. 7.1, but for $\varphi_{12} = 160^\circ$.

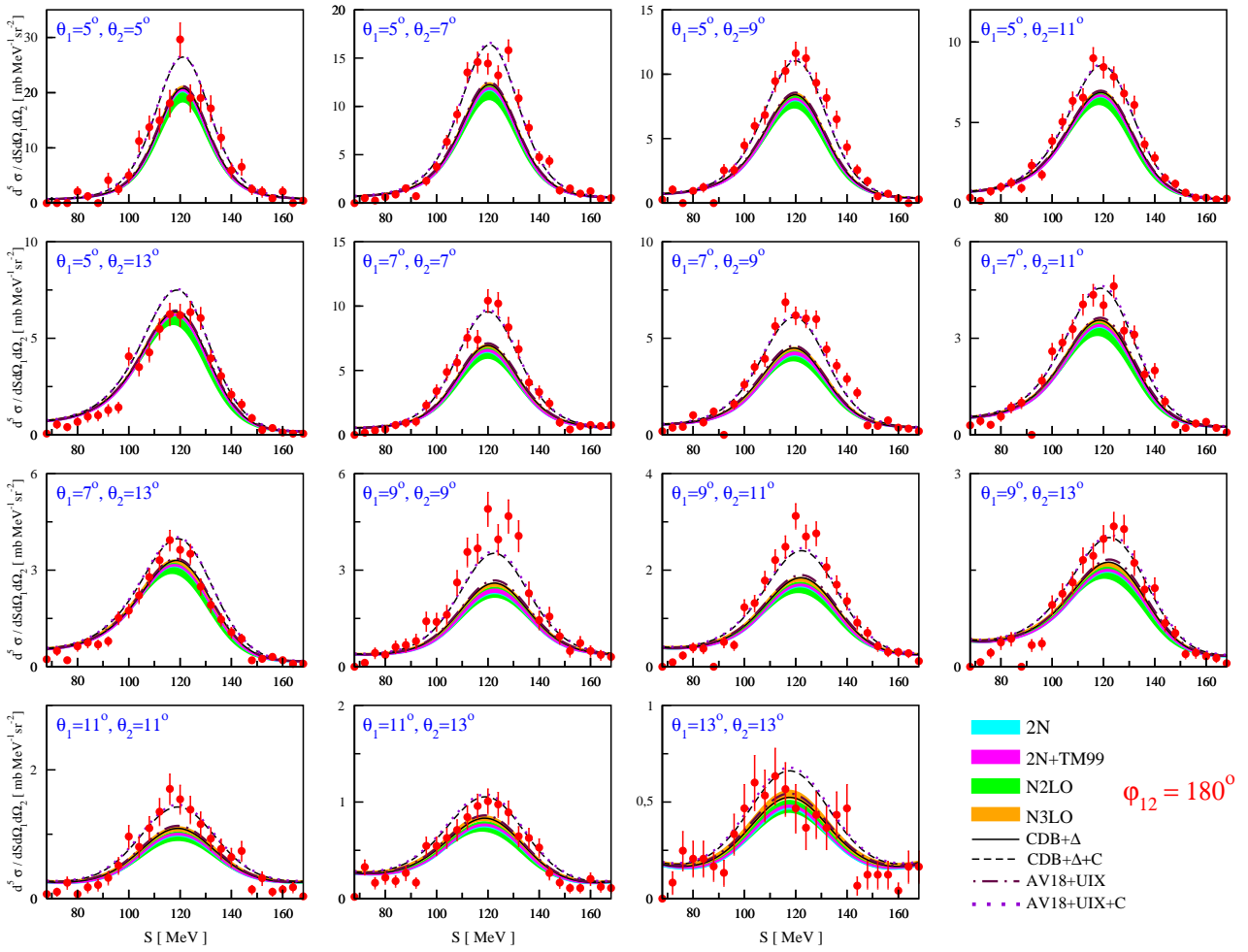


Figure 7.9: Same as in Fig. 7.1, but for $\varphi_{12} = 180^\circ$.

Appendix B

Breakup Vector Analyzing Powers Results

This Appendix contains experimental results of the vector analyzing powers for the reaction ${}^1H(\vec{d}, pp)n$ at 130 MeV. The results are obtained for the two protons registered at given θ_1 , θ_2 and φ_{12} angles, with the ranges of $\Delta\theta_1 = \Delta\theta_2 = 3^\circ$ and $\Delta\varphi_{12} = 40^\circ$. The evaluated data are compared with a set of theoretical predictions, which are presented in the figures as colour bands and lines listed in the included legend. The experimental results and theoretical calculations are presented as a function of the arc-length S along the kinematical curve. In the figures the error bars represent the statistical uncertainties only.

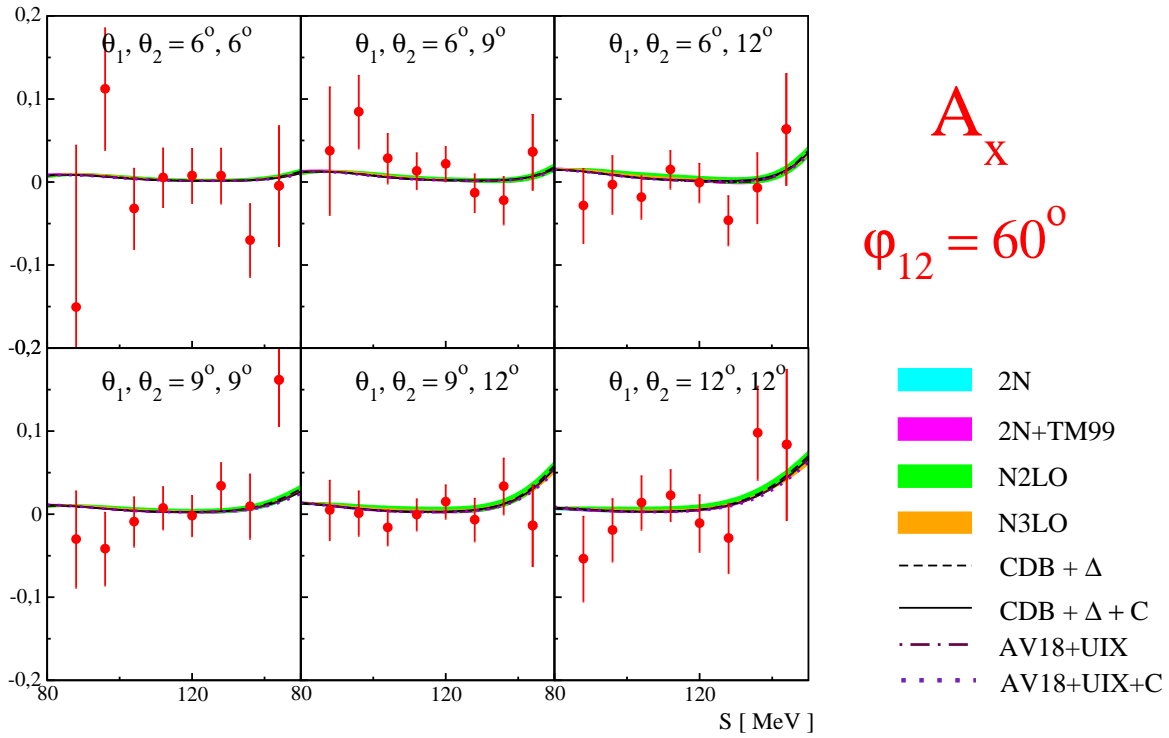


Figure 7.10: The vector analyzing powers A_x for the same relative azimuthal angle $\varphi_{12} = 60^\circ$. Cyan and magenta bands represent calculations based on realistic potentials (with and without 3NF included, respectively), green and orange - chiral theories (at N2LO and N3LO, respectively), black lines - calculations of the coupled channel approach (solid with and dashed without Coulomb interaction included), dashed maroon line - calculations based on the realistic AV18 potential combined with the Urbana IX 3NF and dotted violet line - the same predictions, but with the Coulomb force implemented.

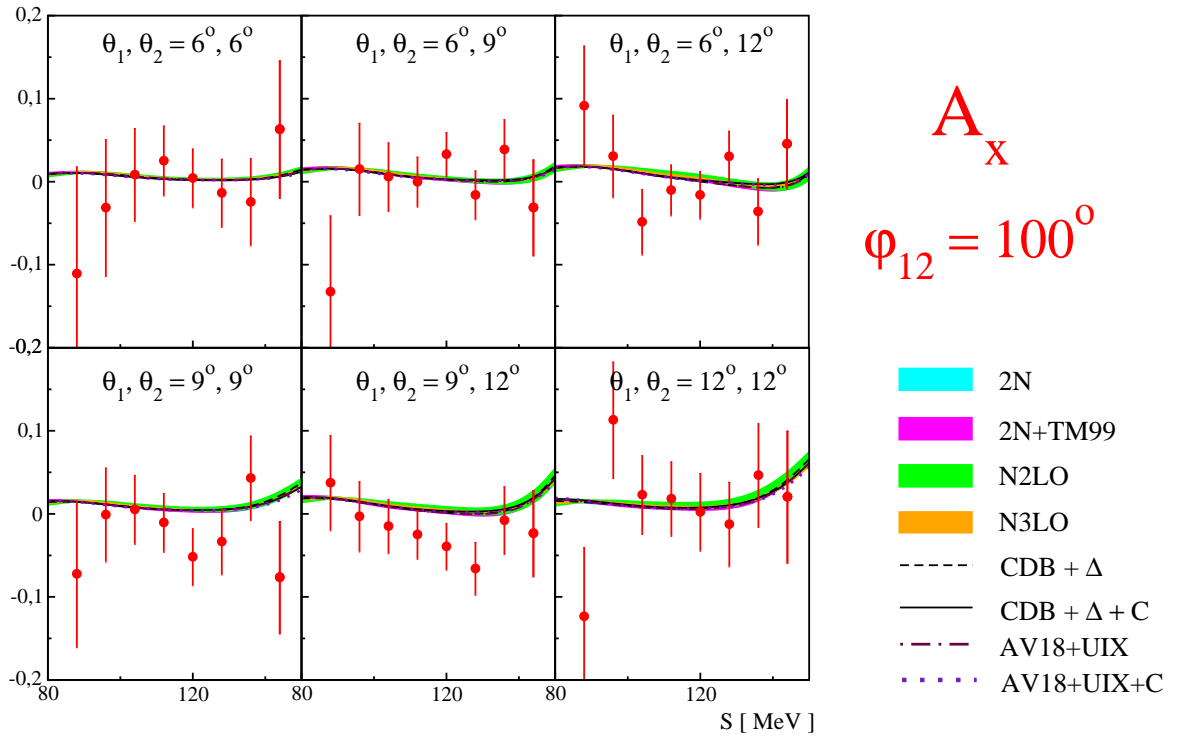


Figure 7.11: Results for A_x as in Fig. 7.10, but for $\varphi_{12} = 100^\circ$.

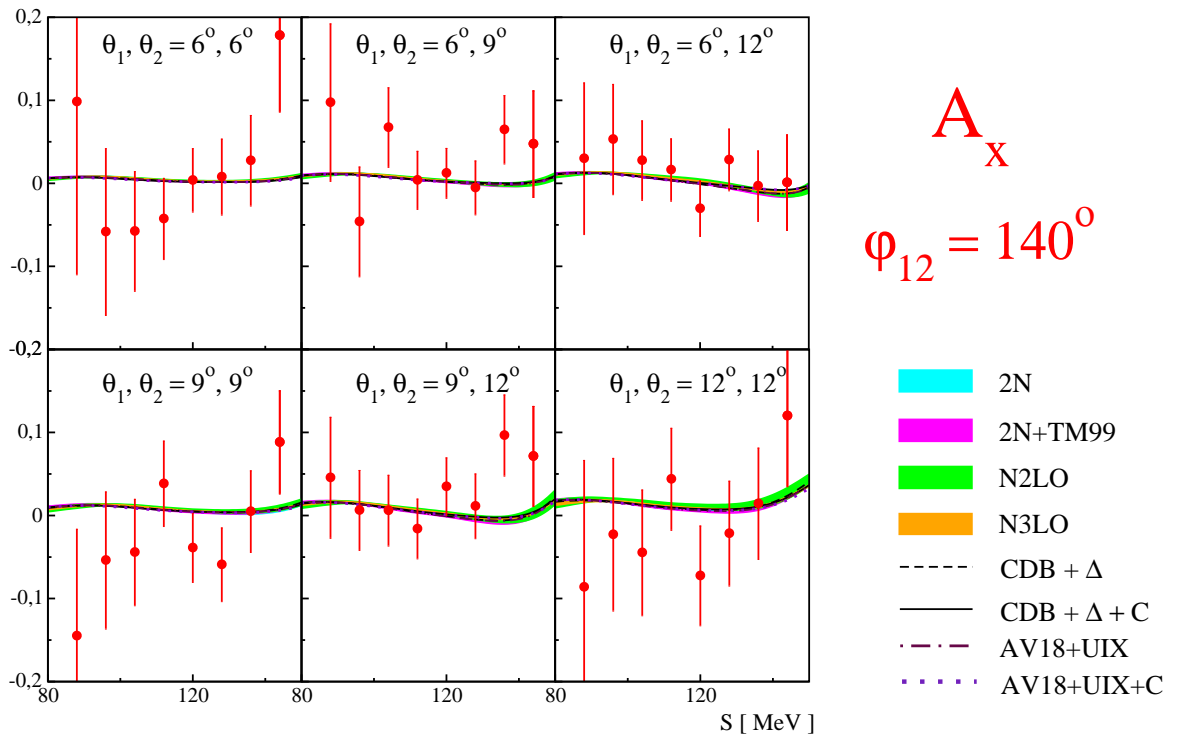
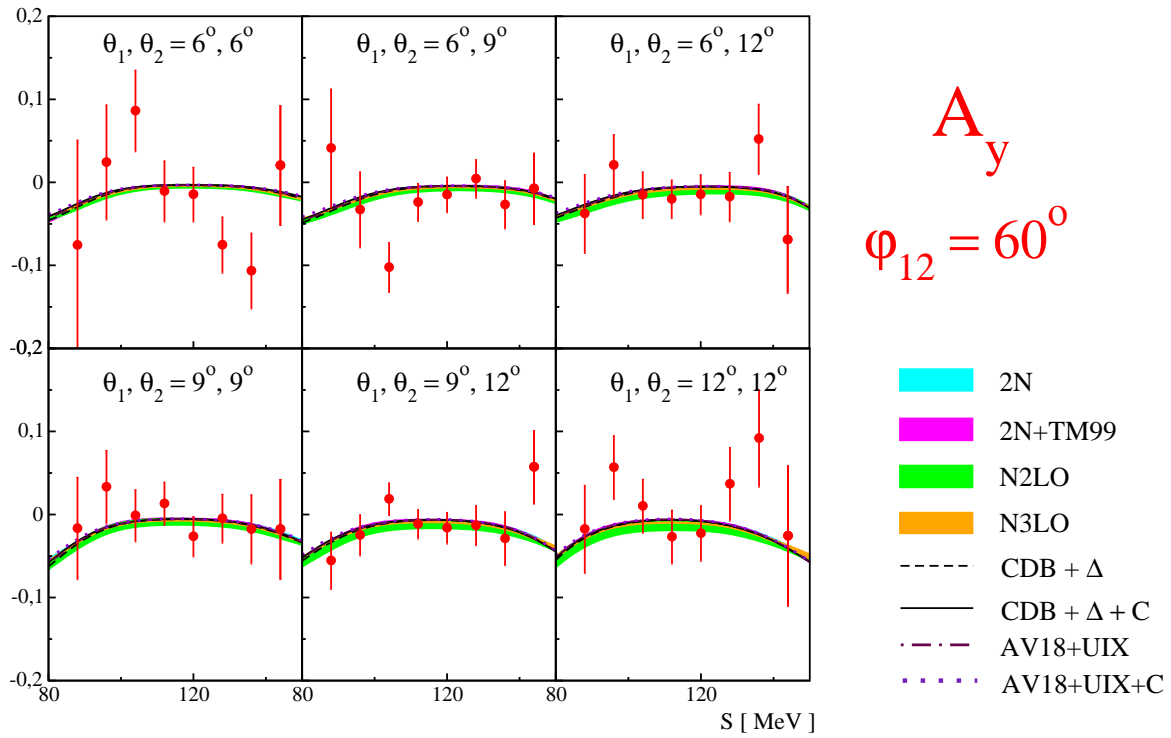
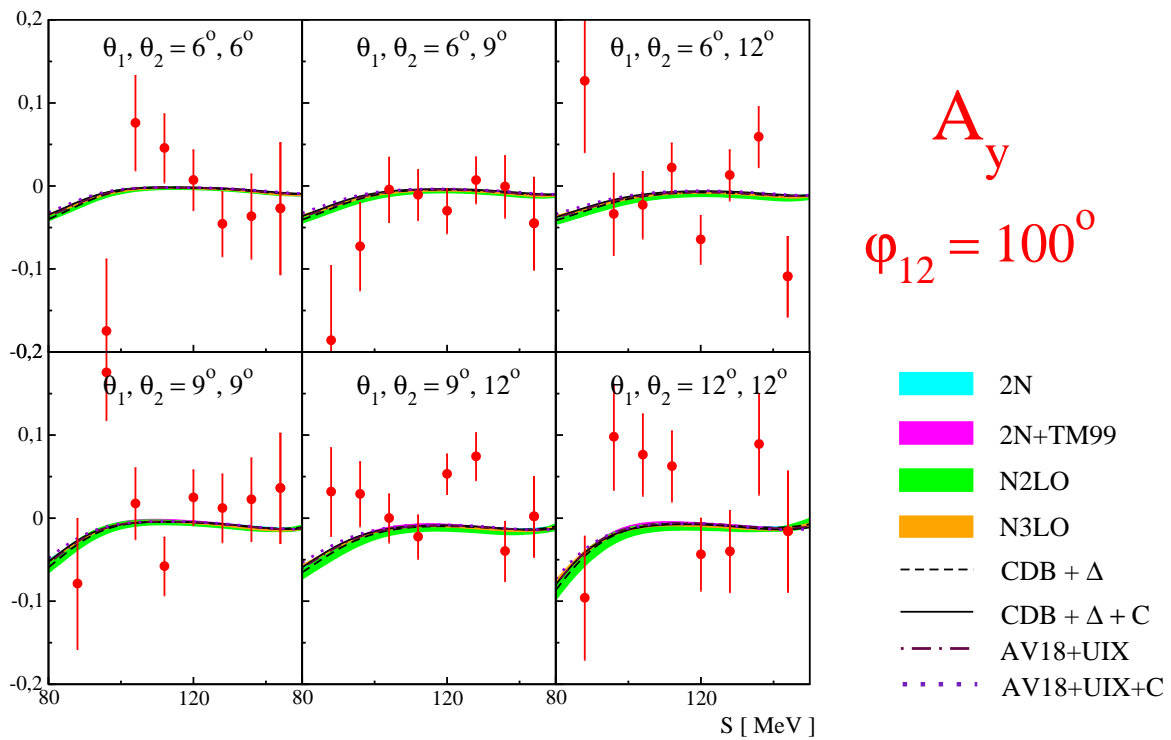
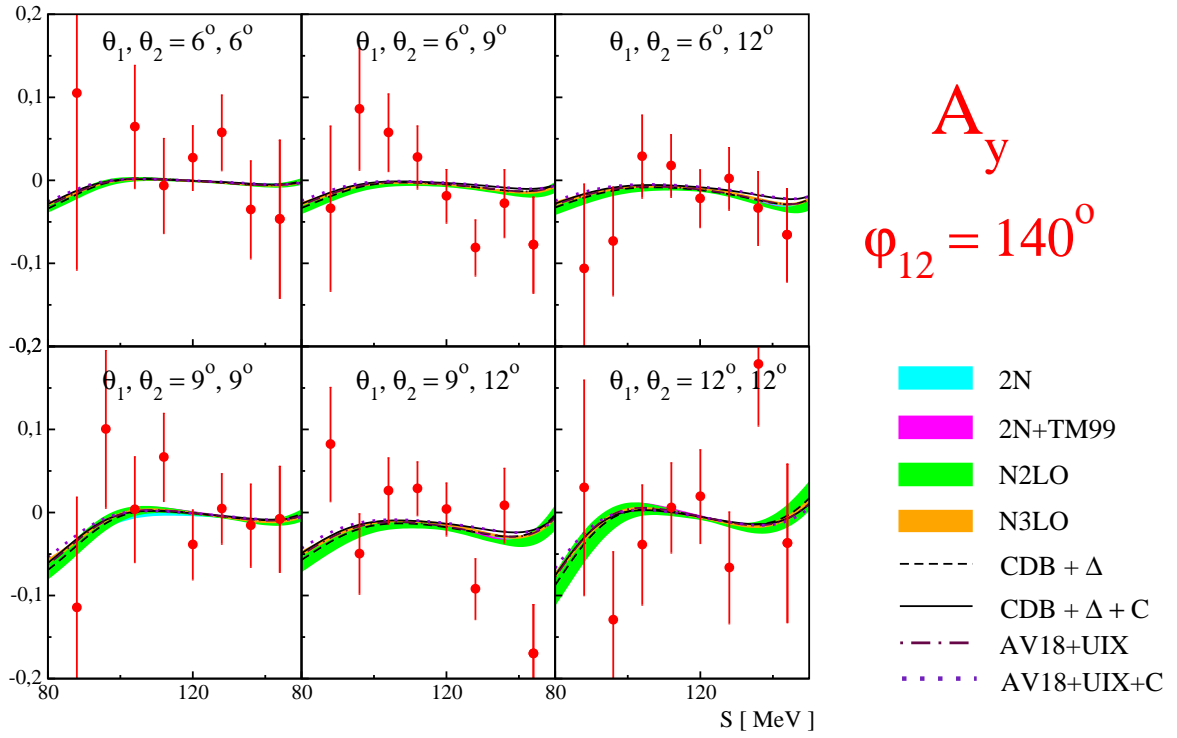
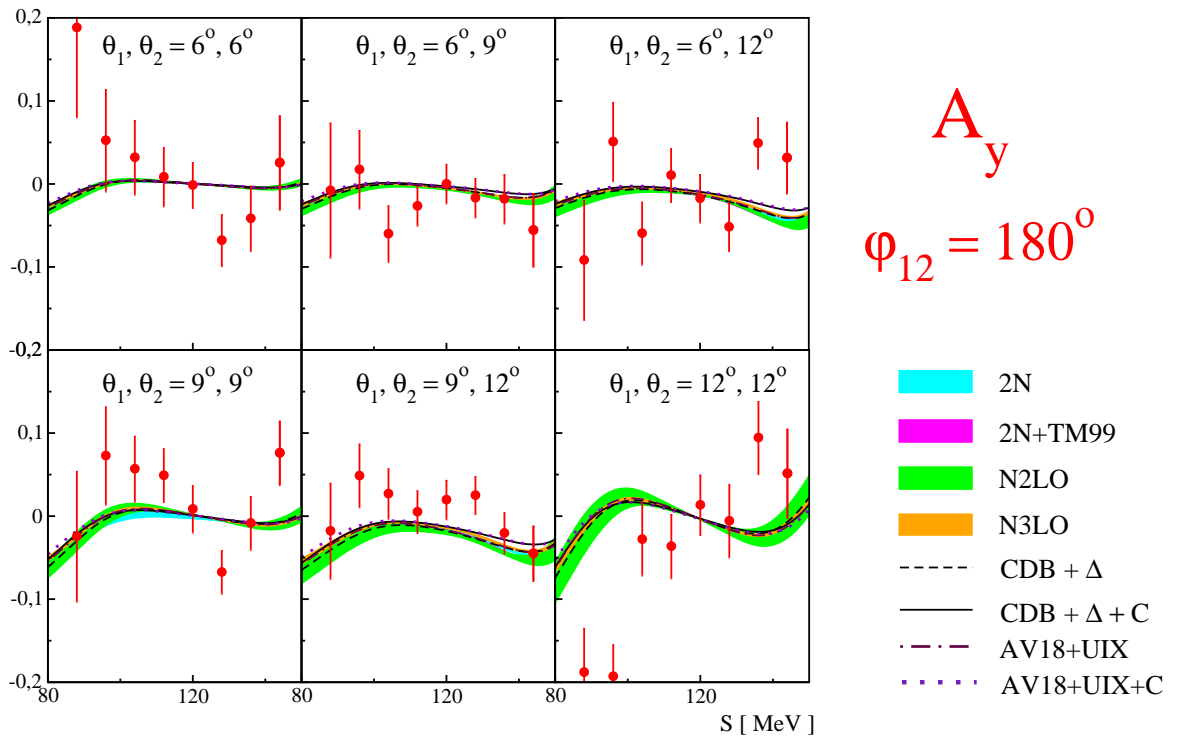


Figure 7.12: Results for A_x as in Fig. 7.10, but for $\varphi_{12} = 140^\circ$.

Figure 7.13: Results for A_y as in Fig. 7.10, but for $\varphi_{12} = 60^\circ$.Figure 7.14: Results for A_y as in Fig. 7.10, but for $\varphi_{12} = 100^\circ$.

Figure 7.15: Results for A_y as in Fig. 7.10, but for $\varphi_{12} = 140^\circ$.Figure 7.16: Results for A_y as in Fig. 7.10, but for $\varphi_{12} = 180^\circ$.

Acknowledgements

At the end, I do wish to thank all the people which helped me to create this work.

First of all I would like to express my deep gratitude to my supervisor **Prof. Dr. Stanisław Kistryn** for teaching and guiding me through all the years during my PhD study and finally for helping me in completion of this work. I am extremely grateful to **Dr. Elżbieta Stephan** for all fruitful discussions and many valuable hints and ideas. Moreover, I would like to thank them both for their great patience and sharing with me their knowledge of nuclear physics.

I would like to express my appreciation to Prof. Dr. Bogusław Kamys for giving me the possibility to prepare this dissertation in the Nuclear Physics Division of the Jagiellonian University.

I wish to thank my Colleagues from the Department for pleasant working atmosphere, as well as for all valuable remarks and discussions concerning the data analysis and computer programming:

Dr. Rafał Sworst,
M.Sc. Małgorzata Fidelus,
M.Sc. Cezary Piskor-Ignatowicz,
M.Sc. Michał Śmiechowicz,
M.Sc. Mariusz Wojciechowski,

I would like to express my sincere thanks to all the Collaborators:

Prof. Dr. Andrzej Magiera,
Prof. Dr. Kazimierz Bodek,
Prof. Dr. Hartmut Machner,
Dr. Regina Siudak,
Dr. Stanisław Kliczewski,
Dr. Mariola Lesiak-Bzdak,
Dr. Piotr Hawranek,
Prof. Dr. Nasser Kalantar-Nayestanaki and the KVI group,
Dr. Barbara Kłos,
Dr. Adam Kozela,
Dr. Jacek Zejma

I do wish to thank my dear Friend Magdalena Kaczmarska, for her kindness, help and support.

Finally I would like to express my deepest gratitude to my whole Family.

Bibliography

- [1] H. Yukawa. *Proc. Phys. Math. Soc.*, Jpn 17:48, 1935.
- [2] P. U. Sauer A. Deltuva, R. Machleidt. *Phys. Rev.*, C68:024005, 2003.
- [3] P. U. Sauer A. Deltuva, K. Chmielewski. *Phys. Rev.*, C67:034001, 2003.
- [4] U.-G. Meissner H.Witała E. Epelbaum A. Nogga W. Glöckle, H. Kamada. *Phys. Rev.*, C66:064001, 2002.
- [5] W. Glöckle U.-G. Meissner, E. Epelbaum. *The European Physical Journal*, A19:125, 2004.
- [6] H. Kamada W. Glöckle L. E. Marcucci S. Rosati M. Viviani A. Nogga, A. Kievsky. *Phys. Rev.*, C67:034004, 2003.
- [7] W. Glöckle H. Witała, Th. Cornelius. *Phys. Rev. Lett.*, 81:1183, 1998.
- [8] S. Oryu P. U. Sauer S. Nemoto, K. Chmielewski. *Phys. Rev.*, C58:2599, 1998.
- [9] H. Sakai et al. *Phys. Rev. Lett.*, 84:5288, 2000.
- [10] K. Ermisch et al. *Phys. Rev. Lett.*, 86:5862, 2001.
- [11] R. V. Cadman et al. *Phys. Rev. Lett.*, 86:967, 2001.
- [12] K. Hatanaka et al. *Phys. Rev.*, C66:044002, 2002.
- [13] K. Ermisch et al. *Phys. Rev.*, C68:051001(R), 2003.
- [14] K. Sekiguchi et al. *Phys. Rev.*, C70:014001, 2004.
- [15] P. Mermod et al. *Phys. Lett.*, B597:243, 2004.
- [16] W. Glöckle et al. *Phys. Rep.*, 274:107, 1996.
- [17] S. A. Coon et al. *Nucl. Phys.*, A317:242, 1979.
- [18] W. Glöckle S. A. Coon. *Phys. Rev.*, C23:1790, 1981.
- [19] B. S. Pudliner et al. *Phys. Rev.*, C56:1720, 1997.
- [20] H. K. Han S. A. Coon. *Few-Body Syst.*, 30:131, 2001.
- [21] H. Rühl et al. *Nucl. Phys.*, A524:377, 1991.

- [22] K. Sagara et al. *Phys. Rev.*, C50:576, 1994.
- [23] N. Sakamoto et al. *Phys. Lett.*, B367:60, 1996.
- [24] A. Micherdzińska. *Experimental Investigation of the Breakup Reaction at 130 MeV*. PhD thesis, University of Silesia, Katowice, 2003.
- [25] J. Kuroś-Żołnierczuk. *Three-Body Effects in Nucleon-Deuteron Scattering*. PhD thesis, Jagiellonian University, Cracow, 2001.
- [26] St. Kistryn et al. *Phys. Rev.*, C68:054004, 2003.
- [27] St. Kistryn et al. *Phys. Rev.*, C72:044006, 2005.
- [28] St. Kistryn. *Three-Nucleon Force Effects in the Deuteron-Proton Breakup Reaction*. Habilitation thesis, Jagiellonian University, Cracow, 2005.
- [29] P. U. Sauer A. Deltuva, A. C. Fonseca. *Phys. Rev.*, C71:054005, 2005.
- [30] P. U. Sauer A. Deltuva, A. C. Fonseca. *Phys. Rev.*, C73:057001, 2006.
- [31] A. Deltuva. *Phys. Rev.*, C80:064002, 2009.
- [32] R. Schiavilla R. B. Wiringa, V. G. J. Stoks. *Phys. Rev.*, C51:38, 1995.
- [33] E. Stephan et al. *Phys. Rev.*, C 82:014003, 2010.
- [34] G. G. Ohlsen et al. *Nuclear Instruments and Methods*, 179:283–294, 1981.
- [35] *Proceedings of The 3rd International Symposium on Polarization Phenomena in Nuclear Reaction*, 1971.
- [36] J. B. England. *Metody doświadczalne fizyki jądrowej*. PWN, 1980.
- [37] Y. Song R. Machleidt, F. Sammarruca. *Phys. Rev.*, C53:R1483, 1996.
- [38] V. G. J. Stoks et al. *Phys. Rev.*, C49:2950, 1994.
- [39] W. Glöckle A. Nogga, H. Kamada. *Phys. Rev. Lett.*, 85:944, 2000.
- [40] G. Rauprich et al. *Few-Body Syst.*, 5:67, 1988.
- [41] W. Grüebler et al. *Nucl. Phys.*, A63:193c, 1987.
- [42] S. Shimizu et al. *Nucl. Phys.*, A382:242, 1982.
- [43] H. Miyazawa J. Fujita. *Prog. Theor. Phys.*, 17:360, 1957.
- [44] L. D. Faddeev. *Sov. Phys. JETP*, 12:1014, 1961.
- [45] K. Sekiguchi. *Search for Three Nucleon Force Effect via $d - p$ Elastic Scattering*. PhD thesis, University of Tokyo, 2001.
- [46] H. Witała W. Glöckle D. Hüber, H. Kamada. *Acta Phys. Pol.*, B28:1677, 1997.

- [47] E. Epelbaum. *The Nucleon-Nucleon Interaction in a Chiral Effective Field Theory*. PhD thesis, Berichte des Forschungszentrums Juelich, Juel-3803, 2000.
- [48] U. G. Meissner E. Epelbaum, W. Glöckle. *Eur. Phys. J.*, A19:125, 2004.
- [49] E. Epelbaum et al. *Nucl. Phys.*, A737:43, 2004.
- [50] U. G. Meissner E. Epelbaum, W. Glöckle. *Nucl. Phys.*, A747:362, 2005.
- [51] A. Biegun. *Analyzing Powers of the $^1H(\vec{d}, pp)n$ Breakup Reaction at 130 MeV in a Large Phase Space Region*. PhD thesis, University of Silesia, Katowice, 2005.
- [52] A. Deltuva et al. *nucl-th/0503015*, to appear in *Phys. Rev. C*.
- [53] A. Deltuva et al. *Phys. Rev.*, C72:054004, 2005.
- [54] St. Kistryn et al. *Phys. Lett.*, B641:23–27, 2006.
- [55] E. Stephan et al. *The European Physical Journal*, A42:13, 2009.
- [56] W. Glöckle H. Kamada U.-G. Meissner H. Witała E. Epelbaum, A. Nogga. *Phys. Rev.*, C66:064001, 2002.
- [57] R. Maier. *Nucl. Instr. Meth. in Phys. Res.*, A390:1, 1997.
- [58] R. Weidmann et al. *Rev. Sci. Instrum* 67, 3:1357, 1996.
- [59] Cosy News. *Forschungszentrum Jülich*, No 8, 2000.
- [60] D. Chiladze et al. *Phys. Rev.*, 9:050101, 2006.
- [61] A. Hamacher et al. *Nuclear Instruments and Methods*, A295:128, 1990.
- [62] M. Betigeri et al. *Nuclear Instruments and Methods*, A421:447, 1999.
- [63] P. Hawranek. $\pi^0 - \eta$ Meson Mixing in Isospin Symmetry Breaking Reactions. PhD thesis, Jagiellonian University, Cracow, 2003.
- [64] Y. Y. Ilieva. *Simultaneous Measurement of the Reaction $pd \rightarrow ^3He\pi^0$ and $pd \rightarrow ^3H\pi^+$ in the Threshold-Resonance Transition Region*. PhD thesis, Bulgarian Academy of Sciences, Sofia, 2000.
- [65] W. Klimala. *Isospin Symmetry Breaking in the $pd \rightarrow ^3H\pi^+$ and $pd \rightarrow ^3He\pi^0$ Reactions*. PhD thesis, Jagiellonian University, Cracow, 2000.
- [66] V. Jaeckle et al. *Nucl. Phys.*, A349:15, 1994.
- [67] A. Hassan et al. *Nucl. Phys.*, A626:435c, 1997.
- [68] M. Gasthuber. Xd manual (ver. 1.1). *Hamburg University*, 1993.
- [69] P. A. Żolnierczuk W. Garske. Data analysis software for gem experiments at cosy. *GEM Internal Report*, 1998.

- [70] W.Garske. *Untersuchung der π^0 und π^+ Produktion in Proton-Proton und Proton-Deuterium Wechselwirkung bei 850 MeV/c*. PhD thesis, Münster University, 1999.
- [71] E. Stephan et al. *Phys. Rev.*, C76:057001, 2007.
- [72] R. Sworst. *Influence of Three-Nucleon Force on Polarization Observables of the $^1H(\vec{d}, pp)n$ Breakup Reaction at 130 MeV*. PhD thesis, Jagiellonian University, Cracow, 2009.
- [73] H. Mardanpour et al. *The European Physical Journal*, A42:383, 2007.
- [74] W. Glöckle H. Witała, Th. Cornelius. *Few-Body Syst.*, 15:67, 1993.